Electronic and Optoelectronic Devices Using Chemical Vapour Deposited 2D Materials



Ye Fan
The Queen's College
Department of Materials
University of Oxford

A Thesis submitted for the Degree of
Doctor of Philosophy

Trinity 2016

Declaration

The material contained within this thesis had not previously been submitted for a degree at the University of Oxford or any other university. The research reported within this thesis has been conducted by the author unless indicated otherwise.

Copyright Notice

The copyright of this thesis rests with the author. No quotation from it should be published without the prior written consent of the author, and any information derived from it should be acknowledged.

Abstract

Two dimensional (2D) materials bear a lot of expectations on playing important role in next generation electronics and optoelectronics. Driven by the thrust of this, this project studies the electronic and optoelectronic properties of 2D materials through device fabrication with 2D materials. Graphene and WS_2 are the representative 2D materials studied in this thesis.

In the study of graphene, a simple method to grow uniform continuous layer of graphene via chemical vapour deposition (CVD) is developed. Factors cause micro-defects like cracks and holes in the graphene sheet are revealed. Our study helps to develop the growth and transfer method of producing chip-sized continuous single layer graphene. This growth and transfer method is currently used as the routine for high quality graphene production in our lab.

The study on graphene device fabrication soon extends to device fabrication with other 2D materials like WS_2. WS_2 photo conductor is fabricated with the CVD WS_2. Large gain factor up to several hundred is achieved in WS_2 photo conductor. A close link between the large gain and trapped states between WS_2 and metal contact is revealed. A photo induced Schottky barrier lowering is measured in this study.

Subsequent studies aim to deepen the understanding on the relation between WS_2 microstructure and its electronic properties results the fabrication of *in-situ*

electronic devices. A novel *in-situ* electronic measurement TEM chip is designed and fabricated. Our measurement reveals the detailed atomic structure of WS_2 after electronic break-down. Furthermore we developed a one-step method to synthesis WS_2 nanoparticles decorated graphene film by electric shock. Our in-situ electronic measurement concludes with a discovery of negative electronic responsivity in the conductance of suspended WS_2 single crystal domain. This result cast light on the fabrication of novel 2D direct electron detector.

Acknowledgements

I would first express my deep thankfulness to my supervisor Porf. Dr. Jamie H Warner. Without his generosity sharing of knowledge and critic comment on my works, this thesis would be impossible. I would also like to extend the acknowledgement to my senior supervisor Prof. Dr. Andrew Briggs. The nervousness during my termly report to him is still fresh in my mind but has mostly turned into a treasure memory of experiences on extending my sight and research interest.

I also own a deep acknowledgement to my colleagues in Oxford. I would express particular thanks to Dr. Alex Robertson and Mr. Haijie Tan. Alex is my major collaborator in the exploring of in-situ electronic device in this DPhil project. His support and broad knowledge on TEM characterizations is one of the determinative factors that lead to our successful in this project. Haijie is my major collaborator in electronic device fabrication, to whom I own enormous cups of coffee during our discussion on experiments and results. I am also in debt to Youmin Rong and Yingqiu Zhou. Their high quality transition metal dichalcogenide 2D crystals are the base stone for many studies carried out my DPhil study.

I should gratefully acknowledge the Clarendon Scholarship offered by the University of Oxford. This generous supports allow me the luxury to focus on academic study, but not suffering from the financial concerns.

To my Parents and Grandparents

First Author Publications

(1) **Fan, Y**.; He, K.; Tan, H.; Speller, S.; Warner, J. H. Crack-Free Growth and Transfer of Continuous Monolayer Graphene Grown on Melted Copper. *Chem. Mater.* **2014**, *26*, 4984–4991.

(2) **Fan, Y**.; Zhou, Y.; Wang, X.; Tan, H.; Rong, Y.; Warner, J. H. Photoinduced Schottky Barrier Lowering in 2D Monolayer WS 2 Photodetectors. *Adv. Opt. Mater.* **2016**.

(3) **Fan, Y**.; Robertson, A. W.; Zhang, X.; Tweedie, M.; Zhou, Y.; Rummeli, M. H.; Zheng, H.; Warner, J. H. Negative Electro-Conductance in Suspended 2D WS 2 Nanoscale Devices. *ACS Appl. Mater. Interfaces* **2016**, *8*, 32963–32970.

Contents

Abstract ii

Acknowledgements iv

Publications vi

Chapter 1
Introduction to the Thesis

1.1 Aim of Project 1

1.2 Scope of the Thesis 1

Chapter 2
Literature Review

2.1 Introduction 3

2.2 Production of 2D materials 5

2.3 Electronic Properties of 2D Materials 21

2.4 2D Electronics and Optoelectronics 43

Reference 62

Chapter 3
Methodology

3.1 Introduction 94

3.2 Materials Production 96

3.3 Device Fabrication 102

3.4 Characterization 109

Reference 120

Chapter 4
Growth and Electronic Application of CVD Graphene

4.1 Introduction 123

4.2 CVD Growth and Transfer of Graphene 124

4.3 Influence of Substrate to Graphene FET 139

Reference 146

Chapter 5
Electronics and Optoelectronics with CVD WS_2

5.1 Introduction 152
5.2 WS_2 Monolayer Photoconductor 153
Reference 172

Chapter 6
2D *In-situ* Electronics in TEM

6.1 Introduction 182
6.2 Electric Breakdown of WS_2/Amorphous-Carbon Film 183
6.3 Negative Electro-Conductance of WS_2 Nano-device 200
Reference 213

Chapter 7
Conclusion and Future Works

7.1 Summary and Conclusions 222
7.2 Outlook into Future Works 224

1

Introduction to the Thesis

Contents

1.1 Aim of the Project 1
1.2 Scope of the Thesis 1

1.1 Aim of the Project

The doctoral project covered by this thesis aims to explore the device application of 2D materials with nano-electronic device fabrication. An emphasis on the influence of micro- and nano- structure to electronic and optoelectronic properties of 2D materials are put throughout this doctoral project. Chemical vapour deposited (CVD) 2D materials (i.e. WS_2 and graphene) are synthesized and studied as functional material. This project leads to the electronic and optoelectronic applications of WS_2 and graphene and finally develops into the successful establishment of an in-situ electronic measurement system. Studies in this thesis deepen our understanding on the origin of unique electronic and optoelectronic properties of CVD 2D materials and broaden the horizon of possible 2D device applications.

1.2 Scope of the Thesis

The thesis incorporates my researches over the span of the four year DPhil study in the Department of Materials, University of Oxford. These four years witness a

booming development in the field of 2D materials, which is also reflected in this thesis. I will mainly focus on the electronic and optoelectronic device applications of 2D materials and highlight the influence of trapped states on these applications.

This thesis starts from a review on recent progress on studies of 2D materials in chapter 2. Materials production and device applications are the two major themes of this chapter, while special attentions are put on linking the physics picture with experimental results. Following the review, major equipment and facilities used during the doctoral project will be introduced as chapter 3. This chapter also covers methodology used to process the experimental data. Chapter 4 reports my study on the CVD growth of graphene. 2D FET array fabricated from wafer-sized monolayer graphene film is realized in this chapter with a discussion on the influence of measurement environment to their field effect. Further study on the device fabrication leads to the fabrication of photodetectors with monolayer WS2 domains in chapter 5. This thesis finish with a realization of in-situ electronic measurement system that enables the in-situ electronic measurement in TEM as reported in chapter 6. Throughout the thesis, an emphasis on the device fabrication and experimental study on 2D materials are placed, though efforts are made to provide a clear picture on the physics mechanisms under the observations.

2

Literature Review

Contents

2.1 Introduction 3
2.2 Production of 2D Materials 5
2.2.1 Mechanical and Liquid Exfoliation 5
2.2.2 Chemical Vapour Deposition 9
2.2.3 Other Production Methods 18
2.3 Electronic Properties of 2D Materials 21
2.3.1 Band Structure 22
2.3.2 Doping the 2D Materials 26
2.3.3 Trap States and Charge Carrier Scatter Centres 33
2.3.4 Junctions and Contacts to 2D materials 38
2.4 2D Electronics and Optoelectronics 43
2.4.1 Influence of Measurement Environment 44
2.4.2 Field Effect Transistors and Logic Circuits 47
2.4.3 Photodetectors with 2D materials 52
Reference 62

2.1 Introduction

The recent years have witnessed an ever more prosperous study into 2D materials after the discovery of graphene, which push the study in material science entering a new dimension. Tremendous experimental and theoretical efforts have been made to understand and make use of the unique properties of 2D materials. Nevertheless, it is worth noticing that experimental results on the studies of 2D materials are chaotic and

sometimes contradictory with each other. This reflects the fact that we are still at the very beginning of exploring the world of 2D materials.

This chapter of the thesis aims to provide a review on the electronic and optoelectronic properties of 2D materials. Particular attention will be paid to chemical vapour deposited (CVD) graphene and materials belonging to the TMDC family. This is not only because they are the two materials that are used in the later chapters of this thesis, but, more importantly, because they are the representatives of 2D semi-metal and 2D semiconductors. This chapter starts with a review on the production method of 2D materials, which lays foundation to experimental studies of 2D materials. The exfoliation and chemical vapour deposition methods are the most popular methods used in today's experiments and thus will be carefully reviewed. Other production methods like epitaxial growth of graphene on SiC will also be covered. In the next section of this chapter (section 2.3) electronic properties of 2D materials are discussed. This section starts with an enlightening tight binding approach to understand the electronic properties of 2D materials. After this, the influence of dopant and trap states on 2D materials will be reviewed. Junctions and metal contacts to 2D materials are also reviewed in this section. Section 2.4 finishes this chapter by looking into applications of 2D materials. This section focuses on applications of 2D materials in information processing (field effect transistors and logic gates with 2D materials) and collection (2D optoelectronics). Several properties reviewed in previous section will be reiterated in this section as mechanisms to explain the experimental results.

2.2 Production of 2D Materials

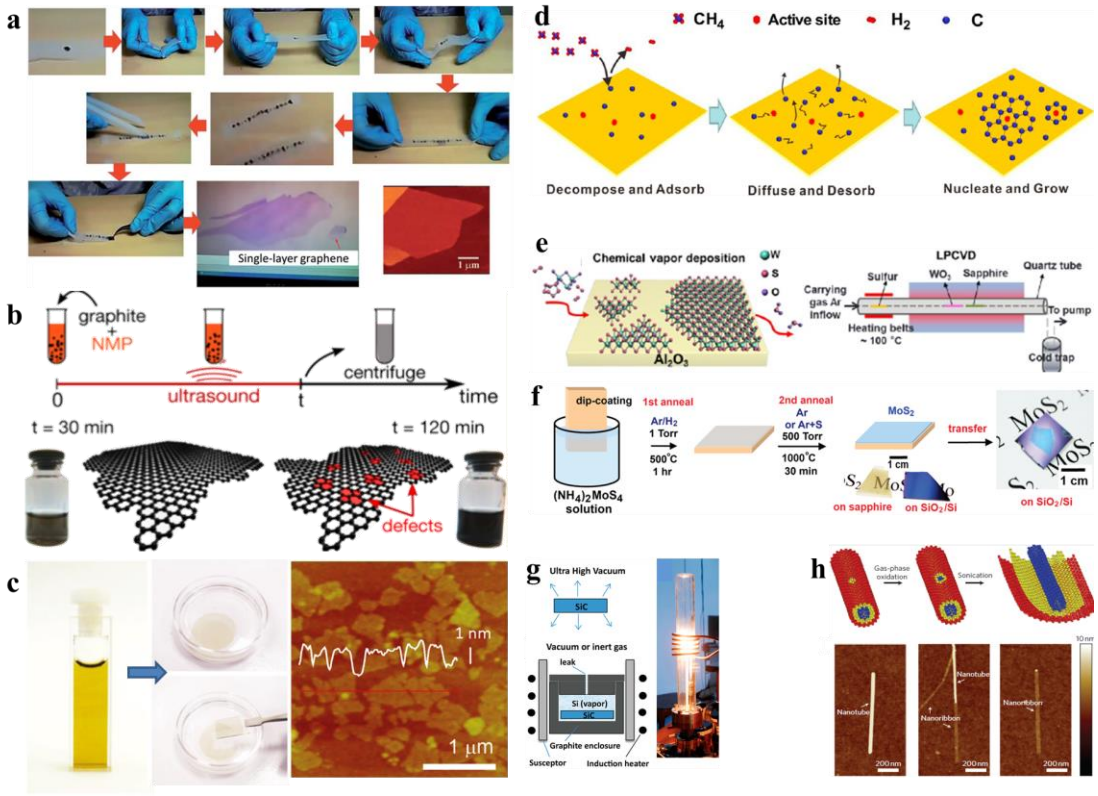


Figure 2-1 Schematics illustrating some conventional production methods of 2D materials. (a) Mechanical exfoliation of graphene. The image is reprinted from reference[1]. (b) Liquid exfoliation of graphene. The image is reprinted from reference[2]. (c) Liquid exfoliation of MoS_2. The image is reprinted from reference[3]. (d) CVD growth of graphene. The image is reprinted from reference[4]. (e) CVD growth of WS2 domains. The image is reprinted from reference[5]. (f) CVD growth of MoS_2 film. The image is reprinted from reference[6]. (g) Epitaxial growth of graphene from SiC. The image is reprinted from reference[7]. (h) Unzipping carbon nanotube. The image is reprinted from reference[8].

2.2.1 Mechanical and Liquid Exfoliation

Mechanical exfoliation

The successful production of graphene from bulk graphite triggered the booming study on 2D materials. The very first production method of graphene is the so called "mechanical exfoliation" method, in which an adhesive tape is firmly attached to, and then peeled off from, bulk layered material. Small pieces of multi-layered material

attached on the tape are stamped onto the target substrate. By repeatedly peeling and stamping the few layer materials on new substrates, pieces of monolayer materials are produced eventually. The mechanical exfoliation method is thus widely known as the "Scotch Tape" method, because Scotch tape is the most popular adhesive medium. Nevertheless, other adhesive mediums such as PDMS[9] or thermal released tape[10] also works. Mechanical exfoliation was first applied to produce graphene from HOPG[11], but soon promoted into a general method for obtaining 2D materials[12]. Monolayer materials from semiconductor like black phosphorus[13] [14] to insulator like BN[15] and from semimetal graphene[16] to superconductor like $Bi_2Sr_2CaCu_2O_x$[12] have all been successfully produced by the mechanical exfoliation method.

Despite its versatility, the laboursome and sophistication of mechanical exfoliation of 2D materials stimulate many attempts to automate such process. For example, Buddhika et al reported to lathe HOPG with superfine sharp tip and produce a large number of pieces of thin graphite flakes.[17] Most pieces produced in this way, however, are still in the form of multi-layer, but neither single nor bi-layer graphene. Jindeng et al tried to exfoliate the graphene by making use of the shear stress during roll milling.[18] HOPG is mixed with polymer before milling the HOPG-polymer plastic into thin film. Thin graphite flakes are generated during this process. Although these attempts achieve certain success in obtaining few layer graphene, automatic mechanical exfoliation is still in its infancy due to the lack of control on the thickness of the final product.[1] The mechanical exfoliation method is a physical approach to

obtain 2D materials and thus does not suffer from extrinsic dopants and defects. On the other hand, the yield rate of this method is very low and requires skilful operations.

Liquid Exfoliation

Liquid exfoliation is another option to separate monolayer material from its bulk form. In this method, small molecules (or ion) in solvent (or solution) intercalate into the layered materials, weaken the van-der-Waals bonding between layers and finally delaminate the layered materials.

Liquid exfoliation of graphene from graphite was first realized by sonication of graphite powder in N-methyl-2-pyrrolidone (NMP).[19] It was proposed that the liquid exfoliation process would be most efficient if minimizing the surface energy between solvent and graphene. Based on this idea, a variety of exfoliation solvent including water/acetone mixture,[20] surfactant/water solution[21], perfluorinated aromatic[22] etc., are studied. Nevertheless, solvent like water that does not wet graphite were also reported to delaminate graphite into graphene.[23] This indicates that the basic mechanism under liquid exfoliation still required further clarification. Similar to mechanical exfoliation, the liquid exfoliation method is a general method to produce 2D materials from its bulk form.[24] The successful obtaining of 2D insulators (e.g. h-BN) and transition metal chalcogenides (TMDC e.g. MoS_2) with similar methods have also been reported.[23]

Different from direct "cleavage" of the layered materials by solvent molecule, a two-step liquid exfoliation method involving ion intercalation followed by hydrolysis are often used in production of TMDC. Changes in chemical bonds, not only van-der-Waals bonds, take place during such exfoliation process. Although the history of seeking monolayer TMDC material using the Li interaction method can date back to 1986,[25] it is only until recently that the old method returns to the spotlight. TMDC materials are sonicated in non-aqueous solution of organic lithium salt (e.g. n-butyl-lithium) to form Li interacted compound.[26] [27] [3] Water is then introduced to hydrolyse such compound which produces suspended few or mono-layer TMDC. It is noted that TMDCs like MoS_2 tend to transforms from 2H phase to 1T phase during the Li intercalation process. In this way, this method is also used to produce 2D materials (like 1T TMDC) that do not exist in bulk form by nature. The detailed mechanism is still under investigation and hereby does not fit in the scope of this thesis. More discussions can be referred to other papers and reviews.[3] [28]

Liquid exfoliation method provide an economically favourable way for industry scale production of few-layer materials compared with mechanical exfoliation method or chemical vapour deposition method as will mentioned in next section. For example, conductive "graphene ink" consisted of liquid exfoliated "graphene" has been produced and sold.[29] Such "graphene ink" can be used to fabricate wires and electrodes in flexible circuit and has attracted lot attentions. On the other hand, the

size and thickness of single piece of “graphene” produced by liquid exfoliation is hardly controllable. “Graphene” produced by liquid exfoliation is generally a collection of sub-micrometre-sized pieces[30] [31] of thin graphite (~ 10 atomic layers)[31] with rarely appeared few-layer graphene. This is indicated by the insignificant field effect of “graphene” produced by this method. In this way, although the liquid exfoliation is favourable for large-scale production, careful selection is still required to find mono- or few-layer 2D material.

2.2.2 Chemical Vapour Deposition

Chemical vapour deposition (CVD) is a chemical method for thin film deposition, with a wide application from lab experiment to industrial production. In CVD process, chemical reaction of precursor gas was triggered by external energy (i.e. high temperature, plasma, tec.), which is followed by nucleation and growth of materials on the surface of substrate. Thermal dynamic factors like chemical component, base pressure of the precursor gas and reaction temperature are major issues controlling the yield of the reaction, whilst kinetic factors like flow turbulence, pre-treatment of substrate and the use of catalyst make differences in the morphology, nucleation density and growth speed of as-grown 2D materials.

This section of the chapter is devoted to review the progress in CVD growth of 2D materials. Graphene and 2D materials belonging to the transition metal dichalcogenide (TMDC) family are the representatives of two types of 2D materials

generally grown on different substrates, which will be carefully reviewed. Metallic catalysts are generally used for the growth of graphene. Catalytic dehydrogenation of the organic gaseous precursor plays an essential role in the CVD growth of graphene. However, direct growth of graphene on dielectric insulators has also been reported and will be discussed in this section. In contrary to graphene, 2D materials belonging to the transition metal dichalcogenide (TMDC) family are generally grown on insulators. A review on CVD growth of TMDC materials will be right after the review of CVD growth of graphene. Mechanisms and techniques reviewed in this section can be well applied to the CVD growth of a broader range of 2D materials, but the details will not be elaborated.

CVD growth of graphene

The realization of chemical vapour deposition (CVD) growth of graphene on metal catalyst is a milestone on the production of 2D materials. Many kinds of metal have demonstrate catalytic ability to graphene, but nickel (Ni), copper (Cu) and platinum (Pt) are the three most popular and well-studied catalysts among them.[32] Studies on graphitization of carbon on Ni substrate have a very long history dating back to the 1970s.[33] Both theoretical and experimental results shows that Ni effectively catalyses the dehydrogenation of hydrocarbons.[34] On the other hand, the relatively high carbon solubility leads to difficulties in controlling the number of layers of graphene grown on Ni. In contrast to Ni, Cu hardly dissolves any carbon, which enables a relative control of the graphene growth. However, the low catalytic ability of Cu results in a

longer reaction time and higher temperature compared with Ni. Pt has an advantage of striking a good balance between catalytic ability and low carbon solubility. However, the high price of Pt casts a shadow on its large-scale usage in the graphene synthesis.

CVD grown thin graphite, or thick multi-layered graphene, on Ni is synthesized soon after the discovery of graphene.[35] After that, few layer graphene with monolayer regions was grown on Ni by carefully controlling the growth temperature, flow rate of precursor gas and growth time.[36] Although few-layer graphene can be easily synthesized on Ni, pushing the layer number down to one or two turns out to be challenging, which is due to the high solubility of carbon in Ni. To suppress the precipitated carbon forming multilayer graphene, various methods are applied for obtaining single layer graphene. By decreasing the base pressure of carbon source and lowering the reaction temperature, the amount of carbon dissolved in Ni should decrease. Following that strategy, single layered graphene grown in ultrahigh vacuum and low growth temperature was realized.[37]

CVD growth of graphene on Cu, on the other hand, enables the growth of single layer graphene in relatively easier growth conditions. Pioneering work by Li et al. reported continuous graphene sheet with 95% coverage of the monolayer graphene grown on copper at low pressure.[38] Their growth pressure (~0.05mbar) is much easier to reach compared with the ultra-high vacuum ($\sim 1 \times 10^{-6}$mbar) commonly used to grow monolayer graphene on Ni. Following their study, Li et al unveiled the fundamental

difference between graphene grown on Ni and copper.[39] They demonstrated that graphene grown on Ni is formed during the cooling process due to precipitation of carbon, which is dissolved into the catalyst earlier during reaction. On the contrary, solubility of carbon atoms in Cu is low, which would enable carbon atoms to migrate on the catalyst surface until collating to form graphene. However, it is soon found that graphene grown on copper are not always of monolayer, especially when grown in ambient pressure. The diffusion of carbon atoms through the copper catalyst is reported as a possible mechanism in the growth of two or even more layers of graphene.[40] Scratches and grain boundaries of copper are also reported as the nucleation spot of graphene and easy to form multilayer domains.[41]

Besides Ni and Cu, Pt is another catalyst commonly used in the growth of graphene. Pt balances a good catalytic ability and low carbon solubility and is potentially one of the optimum catalyst in terms of catalytic ability.[42] [43] The good catalytic ability of Pt is experimentally demonstrated by the lower reaction temperature and faster growth rate of graphene on Pt. Continuous monolayer graphene sheet with multilayer patches was grown on Pt by ambient pressure CVD.[44] It was found that the step edges on Pt surface serve as the preferable nucleation point for graphene.[45] By diluting the concentration of carbon precursor, single layer graphene domains were grown on Pt catalyst.[46] Graphene domains cover several crystal grains of Pt while keeps their hexagonal shape. This result suggests graphene grown on Pt follows a similar absorption-diffusion mechanism as on copper. To recycle the noble metal catalyst,

graphene domains are peeled off from the catalyst with a PMMA scaffold layer by hydrogen bubbles generated in the electrolysis of NaOH solution.[46]

To combine the advantage of different metal catalysts, alloy catalyst was synthesized to reach favourable catalyst performance for graphene growth. The major effort is put in to ally Ni's good catalytic ability on dehydrogenation of hydrocarbon [43] with Cu's low carbon solubility. Continuous multi-crystalline monolayer graphene is successfully grown at relative low temperature (600 ℃) on Cu-Ni alloy.[47] By carefully controlling the gas flow, single graphene domains with a diameter around 3cm are realized on the Ni-Cu alloy recently.[48]

The nucleation and growth of 2D materials in CVD process is sensitive to the chemical conditions of the catalyst surface. Oxidizing the copper catalyst before graphene growth is found to effectively inhibit graphene nucleation. [49] [50] Hexagonal domains of graphene can reach up to the scale of half centimetre. 4 hours annealing of copper under ambient pressure before graphene growth is also found to have a similar effect in terms of lowering the nucleation density, but square shaped graphene domains are grown.[51] Even longer annealing (7h) and lower reaction pressures further decreases the nucleation density and eventually lead to millimetre-sized graphene domains.[4] Gentle oxidation of the copper by wet etching is also found to be helpful.[52] It should be noted, however, surface coating on copper foil would apparently influence the yield of graphene growth. Most researchers use the copper foil from the

Alfa Assar Company following Li's works on graphene growth. However, a coating layer is added onto the copper by the company, at least after 2014, to prevent oxidation. It is unclear how this coating layer on copper would influence the reported pre-treatment results. After 2015, however, the company recovered the production of uncoated copper and noted as "for graphene growth" on their website. Our experimental results do suggest a different result in graphene growth when using the coated and uncoated copper, but detailed discussion is out of the scope of this thesis.

In addition to solid state catalyst, graphene can also be grown on melted catalyst. The catalyst ability of copper remains when it is melted as demonstrated by our group as well as others.[53] [54] Besides copper, melted Ga is found to act as catalyst for the graphitization of amorphous carbon and thus forming graphene.[55] Uniform monolayer graphene is found to grown on different liquid metal (Cu, Ga and In) with high coverage and uniformity.[56]

Considering the bright vista of graphene in application to electronic devices, it is desirable to directly grow graphene on dielectric materials. However, the inefficiency of catalyst ability of common dielectric insulators leaves a question mark on such a growth strategy.[57] [58] Till now, most attempts on direct growth of graphene on dielectric insulators resulted in small graphene flakes not exceeding the level of ten micro-metres. Many strategies have been tried to overcome the lack of catalyst ability of dielectric insulators. Activating the SiO2 surface by pre-annealing in air before

CVD growth is found to assist the nucleation of graphene, which is due to increasing the adsorption of hydrocarbons.[59] Graphene nano-sheets have been synthesized on the surface of MgO at relatively low temperature (325℃).[60] Graphene up to micrometre size has been deposited on mica.[61] Graphene with similar size was also realized on Si_3N_4 coated silicon chip.[62] After 3 hours growth, almost continuous monolayer graphene is grown on high κ materials like $SrTiO_3$, while the grain size is still likely to be small.[63]

CVD growth of TMDC materials

In contrast to graphene, 2D transition metal dichalcogenide (TMDC) materials are generally directly grown on dielectric insulators.[64] CVD growth of TMDC monolayers generally involves the sulfurization of a transition metal compound. Two strategies are generally used to reach this goal. The first method involves sublimation of a transitional metal compound, reaction with the sulphur atmosphere and deposition on the target substrate. In this method, transition metal compound powder is placed in a vial separated from the substrate. The reaction vial is heated to evaporate the transitional metal compound. The gas of the transition metal compound then mixes and reacts with a sulphur gas and results in a deposition of TMDC on substrate. TMDC domains with controllable layer number can be synthesized by this method. However, due to the low partial pressure of most transition metal compound at the growth temperature (~1000℃), this process is sensitive to external influence factors like turbulence and temperature variations. The second method is to directly

sulphurize the transition metal component coated on substrate surface. A layer of transition metal compound is coated on to the substrate prior to loading into the reaction furnace. The coating layer is sulphurized under sulphur atmosphere at high temperature, which transforms the coating layer into a TMDC layer. This method can produce continuous uniform few layered TMDC on a substrate, but there are difficulties in controlling the layer number down to mono- or bi- layers.

Precursor for the CVD growth of 2D materials belonging to the TMDC family are generally solid state. Powder of Metal oxide (MO_3, M=Mo or W) and sulphur (S) are the most commonly used transitional metal compound and sulphur source. The position and temperature of metal oxide, sulphur and substrate should be carefully controlled respectively so as to reach the best yield. By varying these parameters, MoS_2 nanotubes and flakes are reported to be produced instead of monolayer 2D materials.[65] The distance between WO3 and substrate is found to be critical in the formation of WS_2.[66] Similar technique is use to grown $MoSe_2$[67] and p-type WSe_2 [68]. The shape of domain is found to change form triangle to hexagonal when increasing the reaction temperature of the substrate during the synthesis of WSe_2.[69]

In addition to the silicon chip, other chemically inert substrates are studied in the growth of 2D TMDC materials. Sapphire is one the most popular alternative substrates for the growth of TMDC. Effects of a hydrogen atmosphere during growth was studied for WS2 grown on sapphire.[5] To reuse the previous sapphire substrate,

transfer process is improved to enable a self-pealing of the WS_2 with a poly-carbon scaffold layer.[70] Considering the possible epitaxial relation between TMDC and other layered materials, BN and graphite have also been used in the CVD growth of WS_2. WS_2 grown on graphite was found to exhibit a sharp Lorentz-shaped exciton peak in its photo luminescence without trion peak. This indicates good quality and lower doping level in this system.[71] Different from TMDCs grown on graphite, an epitaxial relation between MoS_2 and BN substrates has been disovered.[72] The lattice rotation between MoS_2 and BN is found less than 5°. Considering the improvement of BN substrate on the electronic performance of TMDC materials,[73] this growth method is promising to facilitate the realization of high performance TMDC electronics.

The inert substrates (e.g. SiO_2 or Al_2O_3) are believed to lack catalytic ability and merely provide a scaffold for the nucleation and growth process of TMDC domains. This can be improved by a pre-treatment to the substrate, which would make a difference to the growth result. Spin-coated graphene oxide on SiO_2/Si substrate was found to speed up the growth of MoS_2.[74] Inspired by the effective promotion of MoS_2 growth on graphene oxide coated chip, other seeding promoters containing benzene rings like PTAS are found to efficiently improve the crystallinity of MoS_2 on treated chips.[75]

Another way to grow continuous TMDC films is to directly sulfurize the substrate with pre-coated transition metal compound. A 1.9nm thick MoS_2 layer is grown by

direct sulfurization of a 3.6nm thick MoO_3 layer coated on the sapphire.[76] Hydrogen gas is introduced ahead of sulphur vapour to gently reduce the MoO_3 film and thus increase the chemical activity. In addition, direct sulfurization of thin Mo film on substrate was also proved to produce thin MoS_2 layers.[77] A MoS_2 thin layer with a thickness of 2nm was grown by thermal decomposition of $(NH_4)_2MoS_4$ on a SiO_2/Si chip.[6] Similar to the growth of MoS_2, the growth of WS_2 was realized by this direct sulfurization method. A WO_3 coating layer is used in this approach and sulphur gas is used as the precursor gas. By carefully controlling the thickness of coated WO_3 monolayer WS_2 can be grown occasionally.[78] Although progress has been made in the direct growth of continuous wafer scale TMDC layers by direct sulfurization of coating layer on a chip, multilayer TMDC materials with small grain size are mostly obtained.

The versatility of the CVD method is proven by its ability to synthesize most kind of 2D materials that have been discovered. 2D insulators like h-BN have been synthesized on Ni catalyst by the CVD method under ambient pressure.[79] Similar to graphene, monolayer h-BN was grown on a copper surface.[80] The 2D form of superconductors like Mo_2C were also grown by CVD under ambient pressure.[81]

2.2.3 Other Production Methods

In addition to the exfoliation and chemical vapour deposition reviewed in previous sections, there are several other methods that are specially designed for certain materials.

Epitaxial growth of graphene from thermal decomposition of silicon carbide (SiC) is used to produce graphene on its surface. Silicon atoms on the surface of SiC sublimate leaving a carbon rich surface. This surface will subsequently reconstruct to form graphene. Large area graphene epitaxially grown on SiC have been realized.[82 7] Ultrahigh vacuum ($\sim 10^{-10}$Torr) is required for the thermal decomposition process of silicon carbide. The growth process is further improved to enable wafer size growth of graphene on SiC.[83] To date, there is still no good transfer method for epitaxial graphene on SiC, which seriously limits the application of graphene produced in this method.

Unzipping of carbon nanotubes is a promising method to directly produce graphene nanoribbon. Aqueous solution of $KMnO_4$ is found to selectively oxidize the carbon nanotube and unzip it along the longitudinal direction.[84] AFM and TEM images demonstrate that the unzipped carbon nanotube can result in graphene nanoribbons with width and length ranging from 200nm to a few micrometres. Gas phase etching of double-wall carbon nanotube is also found to unzip the carbon nanotube into bilayer graphene nano-ribbon width 10nm to 30nm.[8] Band gap due to quantum confinement effect emerges in these graphene nanoribbons. Similar etching method is

also used in producing graphene from its bulk form. Multilayer graphene is exfoliated onto the substrate, which is later plasma etched. By controlling the etching time and power, the graphite is etched layer by until monolayer regions are obtained.[85]

Producing graphene by the reduction of "graphene oxide" (GO) is another popular method to produce graphene. Although electronic properties (e.g. charge carrier mobility) of such "reduce graphene oxide" (RGO) pieces are not ideal, they can be produced in large quantity. In this method, graphite is oxidized by wet chemical method. The oxidized product is then diluted and reduced to recover graphene. Many functional groups, however, still remain on the reduced product.[86] Hydrazine hydrate is a common reducing agent used in the reduction, but other agent are also used.[87] It was later found that vacuum annealing of GO at 600℃ also effectively reduce it into graphene.[88] In addition, electric current was found to reduce the GO and form RGO.[89] [90] [91] A thermal effect induced by Joule annealing is assumed to help the reduction of GO similarly to the simple annealing method.[89] However, it is revealed that the actual temperature increase during the current treatment is too small to induce any significant thermal effect. Electrochemical reaction with the help of absorbed water molecules are proposed to be the mode for the reduction process.[90] Hot electrons are also suggested to weaken the carbon-oxygen bond, which would help to evaporate the heteroatoms. [91]

Conventional thin film deposition methods are also used to synthesis coating layers of 2D materials on substrate. Thin MoS_2 film with average film thickness of 2 layers were successfully coated on sapphire substrates with pulsed laser deposition.[92] Atomic layer deposition (ALD) has also been used to grown MoS_2 film on sapphire substrates.[93]

2.3 Electronic Properties of 2D Materials

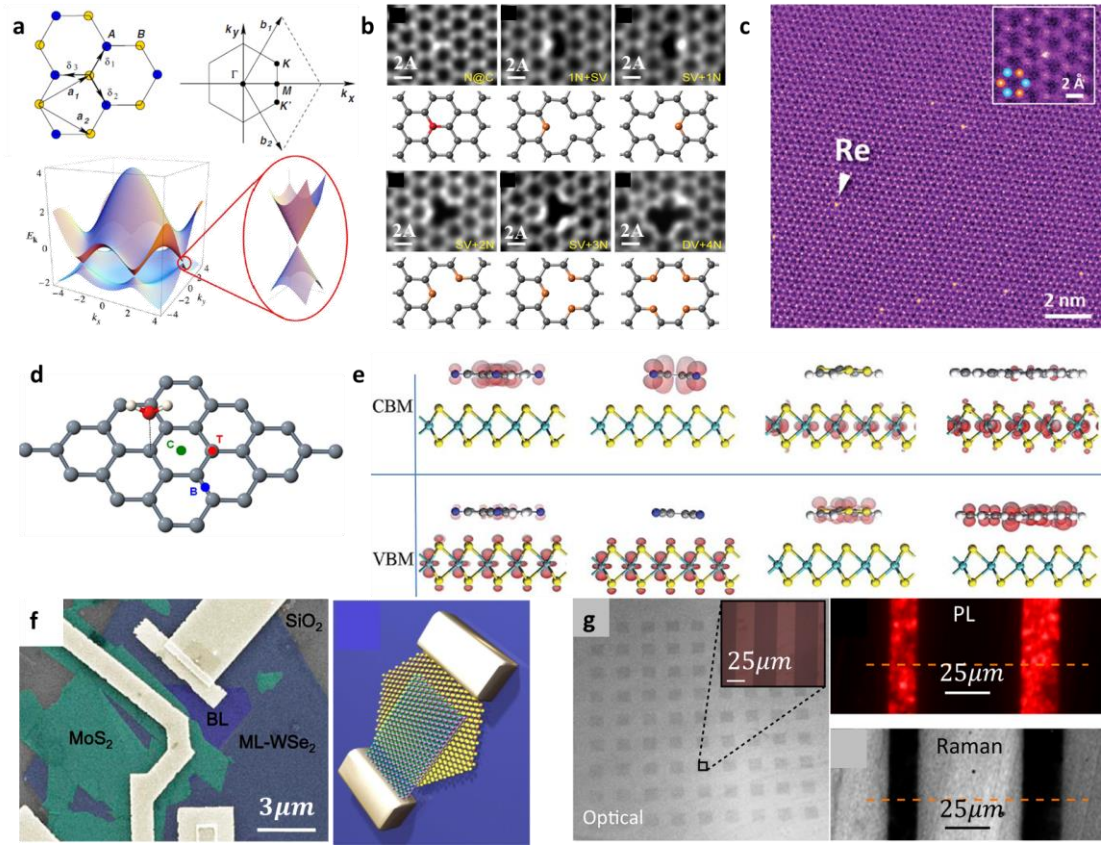


Figure 2-2 (a) Electronic structure of graphene. Two atoms are included in one unit cell and labelled as 'a' and 'b' respectively. The image is reprinted from reference[94]. (b) Atomic structure of nitrogen doped graphene. The image is reprinted from reference[95]. (c) Atomic structure of Re doped MoS_2. The image is reprinted from reference[96]. (d) Schematic of surface doping to graphene. NO_2 molecule is adsorbed on the surface. The image is reprinted from reference[97]. (e) Schematic image of Van-der-Waals doping of adsorbed molecules to TMDC materials. The molecules are TCNQ, TCNE, TTF and BV respectively. The image is reprinted from reference[98]. (f) Fake-coloured SEM and Schematic image of lateral junction between MoS_2 and WSe_2 formed by overlapping. The image is reprinted from reference[99]. (g) Images of the 1D

junction between MoS_2 and graphene. The junction is formed by CVD growth of MoS_2 from graphene edge. The image is reprinted form reference[100].

2.3.1 Band Structure

The intriguing properties of 2D materials are deeply rooted in their unique band structures. This part of section 2.3 begins with the derivation of the band structure of graphene-like 2D materials based on a tight bonding model. Rudimentary as the model appears, it provides a concise roadmap to exploring the electronic properties of 2D materials. Following the tight binding model, several general properties of 2D materials can be found. It should be noted, however, the tight binding model is used only as an enlightening tool, but results from experiment and theoretical calculations based on more precise models are also reviewed.

The tight binding model has a long history in the theoretical study of electronic structures of graphite.[101] In this approach, the crystal orbit is assumed to be a linear composition of the molecular orbit of each unit cell.[102] It is further assumed that only the interactions between neighbour atoms (or atom clusters as in the case of TMDC family) are taken into consideration, which is sometimes referred as the Ising model. By assuming similar lattice symmetry as to graphene (e.g. graphene, silicene and BN), we can write down the Hamiltonian of the crystal. To keep it concise, the Hamiltonian operator is expressed in the form of a generation and annihilation operator.[103] Without special claim, the “Einstein summation convention” (namely, whenever certain footnote appears twice in multiplication, the summation goes over all possible values

of this footnote) is applied hereafter. Another further assumption is that each unit cell consists two atoms (or atom clusters), which are labelled as ‘a’ atom and ‘b’ atom respectively. The two assumptions above can be understood from a chemistry point of view. Atoms in the same unit cell are combined to form a “molecule” before periodically arranged into the crystal. The highest occupied molecular orbit (HOMO) and lowest unoccupied molecular orbit (LUMO) of the “molecule” in one unit cell is further linearly combined to form the electronic band of the crystal.

$$2H = \left(a_{\vec{r}}^{\dagger}, b_{\vec{r}}^{\dagger}\right) A \begin{pmatrix} a_{\vec{r}} \\ b_{\vec{r}} \end{pmatrix} \qquad \text{eq. 2-1}$$

and

$$A = [\begin{pmatrix} 2E_a & \epsilon \\ \epsilon & 2E_b \end{pmatrix} + \begin{pmatrix} 0 & 0 \\ \epsilon & 0 \end{pmatrix} \left(\hat{U}_{\overrightarrow{c_1}} + \hat{U}_{\overrightarrow{c_2}}\right) + \begin{pmatrix} 0 & \epsilon \\ 0 & 0 \end{pmatrix} \left(\hat{U}_{-\overrightarrow{c_1}} + \hat{U}_{-\overrightarrow{c_2}}\right)] \qquad \text{eq. 2-2}$$

In eq. 2-1 and eq. 2-2, H is the Hamiltonian operator, $a_{\vec{r}}^{\dagger}$ (or $a_{\vec{r}}$) is the generation (annihilation) operator of atom ‘a’, and $b_{\vec{r}}^{\dagger}$ (or $b_{\vec{r}}$) is the generation (annihilation) operator of atom ‘b’. The footnote $\vec{r}$ refers to the position of unit cell. E_a, E_b, and ϵ are the energy of ‘a’ atom, ‘b’ atom, and interaction energy between ‘a’ and ‘b’ atom respectively. $\hat{U}$ is the displacement operator, which shifts the coordinate of the generation operator (for example $\hat{U}_{\overrightarrow{c_1}} a_{\vec{r}} = a_{\vec{r}+\overrightarrow{c_1}}$). The foot note $\overrightarrow{c_1}$ and $\overrightarrow{c_2}$ are the unit cell vectors. We have $2H$ in eq. 2-1 because the interaction between atoms is counted twice. Martials with different lattice symmetry would be described by a different expression of A

To solve the band structure of materials, where Hamiltonian operator is described as eq. 2-1 and eq. 2-2, we carry out a Fourier transformation.

Since:

$$a_{\vec{r}} = e^{i\vec{k}\cdot\vec{r}} a_{\vec{k}} \qquad \text{eq. 2-3}$$

Here, $a_{\vec{k}}$ is the generation operator in reciprocal space. It should be noted that $\vec{k}$ is within the first Brillouin zone (FBZ). In this way, we have:

$$2H = \left(e^{-i\overrightarrow{k'}\cdot\vec{r}} a^{\dagger}_{\overrightarrow{k'}}, e^{-i\overrightarrow{k'}\cdot\vec{r}} b^{\dagger}_{\overrightarrow{k'}}\right) A^{*} \begin{pmatrix} e^{i\vec{k}\cdot\vec{r}} a_{\vec{k}} \\ e^{i\vec{k}\cdot\vec{r}} b_{\vec{k}} \end{pmatrix} \qquad \text{eq. 2-4}$$

and $$A^{*} = [\begin{pmatrix} 2E_a & \epsilon \\ \epsilon & 2E_b \end{pmatrix} + \begin{pmatrix} 0 & 0 \\ \epsilon & 0 \end{pmatrix} (e^{i\vec{k}\cdot\overrightarrow{c_1}} + e^{i\vec{k}\cdot\overrightarrow{c_2}}) + \begin{pmatrix} 0 & \epsilon \\ 0 & 0 \end{pmatrix} (e^{-i\vec{k}\cdot\overrightarrow{c_1}} + e^{-i\vec{k}\cdot\overrightarrow{c_2}})] \qquad \text{eq. 2-5}$$

Since:

$$e^{-i\overrightarrow{k'}\cdot\vec{r}} \cdot e^{i\vec{k}\cdot\vec{r}} = \delta(k - k') \qquad \text{eq. 2-6}$$

In eq. 2-6, $\delta(x)$ is the Dirac Delta function. In this way, we have:

$$H = \left(a^{\dagger}_{\vec{k}}, b^{\dagger}_{\vec{k}}\right) A^{*} \begin{pmatrix} a_{\vec{k}} \\ b_{\vec{k}} \end{pmatrix} \qquad \text{eq. 2-7}$$

and $$A^{*} = \frac{1}{2} \begin{pmatrix} 2E_a & \epsilon(1 + e^{-i\vec{k}\cdot\overrightarrow{c_1}} + e^{-i\vec{k}\cdot\overrightarrow{c_2}}) \\ \epsilon(1 + e^{i\vec{k}\cdot\overrightarrow{c_1}} + e^{i\vec{k}\cdot\overrightarrow{c_2}}) & 2E_b \end{pmatrix} \qquad \text{eq. 2-8}$$

The conduction band and valance band of 2D materials is calculated by solving the eigenvalue of A^{*}.

$$E = \frac{1}{2}[(E_a + E_b) \pm \sqrt{(E_a - E_b)^2 + \epsilon^2 \left|1 + e^{-i\vec{k}\cdot\overrightarrow{c_1}} + e^{-i\vec{k}\cdot\overrightarrow{c_2}}\right|^2}] \qquad \text{eq. 2-9}$$

The band structure of graphene is a special case of the results derived in eq. 2-9. Graphene is a planer 2D crystal and the atoms in ‘a’ and ‘b’ position are the same. This results in a reflection symmetry in graphene, and thus $E_a = E_b$. In this way, the band structure of graphene is described as:

$$E_{Gr} = \frac{1}{2}(E_a + E_b) \pm \frac{\epsilon}{2}\left|1 + e^{-i\vec{k}\cdot\vec{c_1}} + e^{-i\vec{k}\cdot\vec{c_2}}\right| \quad \text{eq. 2-10}$$

When $\vec{k}$ is at the K (or K') spot in the reciprocal space, $\frac{\epsilon}{2}\left|1 + e^{-i\vec{k}\cdot\vec{c_1}} + e^{-i\vec{k}\cdot\vec{c_2}}\right| = 0$. In this way, graphene is predicted as a gapless semi-metal with zero density of states at Fermi level according to the tight binding model. Moreover, a linear dispersion relation between energy E and lattice vector $\vec{k}$ near K points of the FBZ is predicted, which is also experimentally confirmed.[104] This result should not be confused with the existence of a band gap in black phosphorus, which is not planer but exhibits a buckled structure. This structure breaks the reflection symmetry between the 'a' atom and 'b' atom, which results in a band gap (about 1.7eV)[105] in monolayer black phosphorus. Another 2D material, silicene, on the other hand, has a crystal structure similar to graphene, but with a slightly different height between 'a' atom and 'b' atom. This height variation, however, keeps the reflection symmetry and thus silicene is also a semimetal with Dirac point at K point in reciprocal space like graphene.[106] As a matter of fact, the symmetry of lattice plays an essential role in determining the crystal structure of 2D material.

Several common features of 2D materials can be understood with the help of the tight binding model. Till now, many two-dimensional semimetals (e.g. graphene[16]), semiconductors (2H-TMDC materials[107 108]) and insulators (e.g. BN[109]) have been studied theoretically and experimentally. All of these monolayer materials are with a direct band gap or zero band gap, which fits with the prediction by tight binding

model. Moreover, the tight binding model predicts the conduction band minimum (CBM) and valence band maximum (VBM) appears at the K point in FBZ if the lattice has a 3-fold (or higher symmetry, which is also satisfied for monolayer materials till now. A further prediction of the tight binding model is that the effective mass of electron and hole near the band edge of 2D materials should be the same. This does not fully agree with the case revealed by experimental and theoretical studies. For example, the effective masses of electron and hole at band edge of MoS_2 are $m_e^* = 0.54m_0$ and $m_h^* = 0.44m_0$ respectively, where m_0 is the mass of electron.[110] Nevertheless, the difference in effective mass between electron and hole is not very large. The tight binding model can be adapted to cope with more complicated cases like multilayer materials.[111] However, the simplicity is lost in exchange of a more detailed and accurate description.

2.3.2 Doping the 2D Materials

The prosperity of modern semiconductor electronics comes only after the realization of controllable doping techniques. In this way it is of vital importance to study the doping to 2D materials. Two main reasons are given for paying particular attention to the doping of 2D materials. First, many electronic applications of 2D materials are determined by doped rather than intrinsic materials. For example, $FeCl_3$ doped graphene can have a conductivity comparable with ITO while maintaining a good transparency.[112] In addition, Diodes of materials with different doping level play important role in rectifying electronics and photovoltaic applications. The second

reason lays in the fact that most 2D materials are intrinsically doped. The reason for this doping is generally complicated, which make it hard to make use of. A thorough understanding on the doping effect to 2D materials would thus favour both scientific studies and technology applications.

This part of section 2.3 will review the methods and effects of doping to 2D materials. The review unfolds into a discussion on three types of doping method. Substitutional doping of 2D materials starts the review in this section. In this doping strategy, a small portion of atoms in the intrinsic material (e.g. C atoms in graphene) are substituted by extrinsic atoms (e.g. N atoms). This kind of doping has been thoroughly studied and overwhelmingly used in conventional 3D materials, but studies on 2D material are still in their beginning stage. Substitutional doping of graphene and materials in the TMDC family are reviewed as two examples. Following substitutional doping, the surface adsorption doping of 2D materials will be discussed. Most cases of unintentional doping, especially in CVD grown materials, happen in this form. The large surface aspect ratio of 2D materials makes them much more sensitive to surface absorbed molecules compared to 3D materials. The doping effect of surface absorbed molecules on 2D materials is also made use of to artificially dope 2D materials. Similarly to the review on substitutional doping, this part of review will focus on graphene and TMDC materials. Our review finishes with a discussion on doping 2D materials with adding a layer of another 2D material. From a physics point of view a new band structure should be used to describe the vertical

stacking of several 2D materials. In this aspect, it is questionable whether this hybrid should be treated as a doping process, which generally tunes the Fermi level without changing the band structure. However, a simplified picture of such hybrid material that only considers the "charge transfer" between the neighbour layers of 2D materials prevails in the literature. It turns out to be a simplified yet useful model to understand many electronic and photonic properties of such hybrid materials. In this way, "doping" a 2D material with another 2D material will also be reviewed in this section.

Substitutional doping

Substitutional doping is commonly used in semiconductor doping for 3D materials, but it turns out to be challenging for 2D materials. Bilayer graphene doped by B atoms was realized in graphene synthesized by the arc discharge method.[113] B_2H_6 gas is introduced during the synthesis to dope graphene. The arc discharge method, however, only produces small pieces of graphene and thus has limited device applications. Continuous B doped graphene was realized by a CVD method later.[114] Phenylboronic acid ($PhB(OH)_2$) was heated and evaporated during the growth process to provide a mixture of carbon and boron precursor gas. The p doped nature of B-doped graphene is further proved by the field effect measurement of graphene grown by this method.

Considering most CVD grown graphene is intrinsically p-doped, compensation n doping of graphene has attracted a lot of attention. Substitutional negative doping of

graphene by nitrogen atoms was realized by introducing NH_3 during the CVD growth process.[115] 1% to 3% of the carbon atoms were replaced by N atoms according to XPS results. The N doped graphene exhibits a Dirac point appearing at negative gate voltage in field effect measurements. Plasma treatment in a gas of the dopant was also found to induce substitutional doping to graphene. Nitrogen plasma treatment was used to dope reduced graphene, which is originally heavily p-doped.[116] The effective substitution of C atom by N atom was proven by XPS. It is interesting to notice the significant D peak appears in the Raman spectrum of substitutional doped graphene, no matter the doping type or method of doping. It is yet unclear whether the substitutional atoms or other factors cause defects in graphene.

Substitutional doping to materials in the TMDC family attracts even wider attention compared with graphene. Chalcogen atoms in TMDC materials can be replaced to alter their electronic properties. Halogen atoms like Cl, Br or I have been known to n-dope the bulk TMDC materials.[117] The Fermi level of WS_2 and MoS_2 is reported to be levelled up by chloride molecules.[118] The chloride molecule dopant is introduced by soaking multilayer WS_2 or MoS_2 flakes in 1,2-dichloroethane for a long time. Field effect measurements clearly show the n doping effect of such a treatment. Chlorine atoms are assumed to occupy the sulphur vacancy and thus work as a substitutional n dopant to TMDC. A low energy phosphorus (P) implantation is found to effectively p-dope few-layer MoS_2.[119] Although the implantation energy is low, defects are still

introduced to the few-layer MoS2, and result a large subthreshold swing measured in the transfer curve of the doped material.

On the other hand, metal atoms in the TMDC family (i.e. Mo or W) are also replaceable during the doping process. Positive doping of MoS_2 is realized by substituting the Mo atom with Nb atom.[120] The threshold voltage of a FET on 300nm SiO_2 dielectric layer positively shifts more than 60V after the doping. A highly conductive p-type Nb doped MoS_2 was achieved. The Nb doping technique has been used for the synthesis of doped bulk TMDC for a long time.[117] Mo atoms in MoS_2 can also be replaced by W atoms.[121] A CVD method was used for the materials growth. The band gap of $MoxW_{1-x}S_2$ was found to depend on the ratio between W and S atoms.

Surface absorption doping

Comparing with substitutional doping of 2D materials, Van-der-Waals surface molecule doping of 2D materials is easier to achieve and draw a lot interest in experimental studies. Structure defect is less likely to be caused by the adsorption molecules, but they still efficiently control the Fermi level of the 2D substrate.

An intuitive way to n dope graphene is to absorb alkali metal atoms that have a high work function like K on the graphene surface.[122] The dopant is found to effectively n dope graphene but also induce a strong charge carrier scattering and thus decrease

charge carrier mobility. The first principle study on the doping effect of different gas molecules suggest that H_2O and NO_2 are strong electron acceptors and thus should p dope graphene. On the other hand NH_3 and CO should be electron donors and thus n dope graphene. All these predictions have been confirmed experimentally.[123] However it is later revealed that the sensitivity of graphene to gas molecules is determined by the defect density or functional groups on graphene but not an intrinsic property of graphene.[124] Joule annealing graphene in NH_3 atmosphere turns out to be more effective in doping the graphene compared with graphene simply exposed the NH_3 atomsphere.[125] In this way, the doping process is proposed to be assisted by the defects induced during the annealing process. Besides small molecules, like what has been mentioned above, specially designed strong electron acceptors like F4-TCNQ are used to surface dope the graphene. Positive doping of epitaxial graphene on SiC is realized by covering the graphene with evaporated of F4-TCNQ.[126] The p dope effect is characterized by the shift of peaks in XPS measurement.

Surface absorption doping on 2D TMDC materials is also under intensive study. Liquid based doping techniques are carried out on exfoliated WS_2. LiF or KI are used to n-dope WS_2.[127] [128] The sensitivity of 2D materials to external dopants is useful for application in gas sensing.[129] The conductance of MoS_2 is found to decrease to about 20% of its original value after exposed to 400ppb NO_2 gas. On the other hand, the conductance of MoS_2 increases to more than 10 times of its original value after being exposed to 500 ppm NH_3. The conductance of MoS_2 returns to its origin value after

the NH_3 gas is pumped away. This indicated that NH_3 was adsorbed on, but not reacted with, the MoS_2. Deep ultraviolet (UV) light is used to accelerate the rate of doping.[130] Mono- or bi- layer WS_2 is exposed to N_2 or O_2 gas when illuminated by deep UV. N_2 gas is found to n dope the WS_2, which results in a negative shift of threshold voltage of WS_2 FET on 300nm SiO_2 by 60V after 30min of deep UV illumination. On the other hand, O_2 gas p dopes the WS2 and results in a 50V positive shift of the threshold voltage after 10min UV illumination. Time resolved photo current measurement reveals a slow response and recovery process (characteristic time is around tens of seconds), which is attributed to the introducing of trap states during the UV treatment. F4-TCNQ is also used to p dope TMDC materials.[131] The p dope effect of F4-TCNQ to TMDC was confirmed by a significant change in the ratio between the intensities of trion and exciton peaks before and after the doping.

Charge transfer doping between 2D materials

When 2D materials stack together, the electrons redistribute to minimize the total energy. The electron redistribution process is generally understood as a charge transfer without changing the band structure of materials. Stacking WS_2 on graphene is reported to n-dope graphene, which is marked by the shift of Dirac point of the graphene.[132] It is interesting to note that the n-dope effect of WS_2 on graphene becomes stronger when it is illuminated by incident light. This means a stronger polarization between graphene and WS_2 when illuminated. In this way, the apparent photo assisted “charge transfer” is likely due to a photo gating effect, but not simply a

photovoltaic effect in between the 2D materials. A similar charge transfer and photo gating effect is also found in the stacking of 2D CdSe on graphene.[133]

2.3.3 Trap States and Charge Carrier Scatter Centres

The prosperous study on 2D materials also reveals certain variations and disagreements between theoretical prediction and experiments and between experiments themselves as well. For example, although some exfoliated graphene exhibits high mobility around the theoretical limit caused by phonon scattering, graphene gown by CVD generally exhibits much lower charge carrier mobility. In addition, the photo response times of devices are generally longer than their theoretical expectations. Trap states are accordingly believed to make difference on the electronic and optoelectronic performance of devices. The term “trap states” generally refers to localized states that “trap” charge carriers, while the charge scatter centre is generally used to describe a perturbation to the charge carriers that are delocalized. However, the boundary between these two concepts is not a clear-cut. For example, shallow trap states with a trapping energy lower than the energy of environmental thermal excitation will not localize charge carriers but transfer into a scattering centre. In this section, these two terms are used somewhat interchangeably, but follow the convention of the literature. Similar to previous sections, this section aims to provide experimental evidence on relative topics. Awareness of the important role of these trap states in determining the electronic properties of 2D materials is hoped to be raised.

The study of trap states and charge scattering centres in 2D system is still at the very early stage. In this section the charge scatter centres, or electron-hole puddles, in graphene will be discussed first. Because of the linear dispersion relation in graphene, charge carriers can tunnel through the energy barrier around the trap states and thus cannot get "trapped". However, these trap states, which can be caused by extrinsic factors like oxygen defect in dielectric oxide or intrinsic factors like defect in graphene, still scatter the charge carriers and thus act as charge scattering centres. After the review on graphene, trap states in 2D TMDC will be discussed.

Electronic measurement of trap states

A determinative measurement of the trap states by electronic method is challenging not only in 2D but even in conventional 3D materials. This is partly due to the fact that similar electronic measurement results could be the result of different mechanisms and single experiment is generally hard to interpret. However, there are still several electronic methods to cast light on the characterization of trap states. In this part, one of the most commonly used electronic measurements is reviewed.

The measurement of sub-threshold swing is one of the major methods to characterize trap states in semiconductor. In an ideal 2D semiconductor, when the Fermi level is tunnelled near but not yet reach the conduction band minimum (CBM) or valence band maximum (VBM), a small leakage current starts to flow through the device.

This is the so called "sub-threshold region" in the transfer curve. By assuming the electron (or hole) obeys a Boltzmann distribution when the Fermi level is near the CBM (or VBM), we can get the following relation between subthreshold conductivity versus temperature.[134]

$$\mathrm{S} \coloneqq \frac{1}{I} \cdot \frac{dI}{dV_g} = \frac{q}{kT}(1 - c_c/c_g) \qquad \text{eq. 2-11}$$

In eq. 2-11, I is the sour-drain current, V_g is the gate voltage, $\mathrm{k} \approx 1.38 \times 10^{-13}\mathrm{J/K}$ is the Boltzmann factor, T is the temperature, q is the absolute value of electrical charge of the charge carriers, c_c is the capacity between channel and contacts and c_g is the capacitance between channel and gate. The so called subthreshold swing is more commonly used in practice which is defined as:

$$S_{sw} \coloneqq \frac{\ln(10)}{\mathrm{S}} = \ln(10)\frac{kT}{q}(1 + c_c/c_{ox}) \qquad \text{eq. 2-12}$$

In eq. 2-11 and eq. 2-12, it is generally the case that $c_c \ll c_{ox}$. The subthreshold swing is used to characterize how "quick" a transistor turns on and off by means of changing the gate voltage. The smaller subthreshold swing marks a "quicker" turning on of the transistor. However, a theoretical limit for a transistor working at room temperature can be derived from eq. 2-12 as 60mV/dec, and a commercial conventional field-effect transistor generally reaches a subthreshold swing at 70mV/dec.

The existence of trap states will slow down the "turning on" process of a transistor, especially when they are within the band gap of material. In this way, the density of trap states can be measured by the increase of subthreshold swing.[135]

$$S_{sw} = S_{sw0} \times (1 + \frac{q^2}{c_g} N_{tr}) \qquad \text{eq. 2-13}$$

In eq. 2-13, S_{sw} is the measured subthreshold swing, S_{sw0} is the subthreshold swing for idea semiconductor, which is about 60mV/dec in room temperature, q is the charge of charge carrier, c_g is the gate capacitance and N_{tr} is the trap states density. A similar method has been proposed to apply to 2D materials without major changes.[136]

Charge scatter centres in graphene

The experimental value of electron mobility of CVD graphene at room temperature is reported to vary from $\sim 10^2 \mathrm{cm^2 V^{-1} s^{-1}}$ to $\sim 10^5 \mathrm{cm^2 V^{-1} s^{-1}}$.[59] [137] [52] [49] [138] The record of room temperature mobility as high as $10^5 \mathrm{cm^2 V^{-1} s^{-1}}$ is set by suspended[139] or BN encapsulated graphene[138] [140], however, the average reported mobility of graphene is around $10^3 \mathrm{cm^2 V^{-1} s^{-1}}$. It is believed that the electron-hole puddle, which acts as the charge carrier scatter centres, is responsible for such a variation in mobility. The origin of such electron-hole puddle could be from either extrinsic adsorbed molecules or intrinsic defects.

Adsorbed molecules are one of the major reasons for the decrease of mobility. Electrical interaction between the charged impurity with graphene is one of the reasons for the decreased mobility in doped graphene.[122] Mobility decreases in potassium (K) doped graphene are found to be proportional to the reciprocal of dopant concentration, which supports the theory prediction on the charge carrier scattering caused by electrical interaction between impurities and graphene. Electron mobility

decreases quicker than hole mobility when increasing the dopant concentration. The mobility decreases to less than $10^3 \mathrm{cm}^2\mathrm{V}^{-1}\mathrm{s}^{-1}$ when the K concentration increase to about 1.5×10^{-3} K atom per C atom. This result is similar to what can be seen from graphene doped with other atom or molecules.[141] The mobility of both electrons and holes reaches the highest value when the Dirac point appears around zero gate voltage, but keeps on decreasing when n doped by adsorbed molecules. As for the p dope of graphene, similar phenomenon repeats. For instance, NO_2 is found to p-dope graphene together with a degradation in mobility of both electrons and holes.[123] In this way, surface adsorbed molecules are experimentally demonstrated to scatter charge carriers in graphene.

Defects are also found to influence the mobility of graphene. Defect density in CVD graphene films are found to directly change the mobility of graphene.[142] The ratio between D and G peak in Raman spectra of graphene are used to mark the defect concentration in the graphene film. The mobility decreases from $1300 \mathrm{cm}^2\mathrm{V}^{-1}\mathrm{s}^{-1}$ to about $400 \mathrm{cm}^2\mathrm{V}^{-1}\mathrm{s}^{-1}$ when defect concentration increases from $10^8 \mathrm{cm}^{-2}$ to $10^{11} \mathrm{cm}^{-2}$. Defects in this study are induced by changing the H_2 concentration during growth, but the measurement was always on a monolayer region of the graphene. Defects can also be artificially created by Ne^+ ion irradiation of exfoliated graphene.[143] The mobility found to inversely depend on the dose of Ne^+. The mobility decreases from $10^4 \mathrm{cm}^2\mathrm{V}^{-1}\mathrm{s}^{-1}$ to $10^3 \mathrm{cm}^2\mathrm{V}^{-1}\mathrm{s}^{-1}$ when Ne^+ dose increase from zero to $10^{12} \mathrm{cm}^{-2}$.

Trap states in TMDC

Different from graphene, the influence of trap states on 2D semiconductors like TMDC materials is more significant. Trap states are revealed by AC measurement of the capacitance of MoS_2.[144] The density of mid-gap trap states is measured as $10^{12}\mathrm{eV}^{-1}\mathrm{cm}^{-2}$ and the density of band edge trap states is $10^{14}\mathrm{eV}^{-1}\mathrm{cm}^{-2}$.

The sulphur vacancy is one of the most common defects in TMDC. It is theoretically shown that the sulphur vacancy will introduce a mid-gap localized trap states.[145] This partly explains the experimental discovery of an insulating state of TMDC when measured in air.[146] The mid-band tapped states cause a hopping transport under low temperature.[147] The measured defects from TEM observation fits well with what calculated values according to the hopping model, which confirms that sulphur vacancy is likely to be the source of trap states.

2.3.4 Junctions and Contacts to 2D materials

Junctions and contacts to 2D materials play a central role in 2D electronics. This is not only because a number of junctions and contacts appears by nature in any devices fabricated, but also because they directly determine the measurement results. This part of section 2.3 reviews three major types of junctions and contacts. First, lateral junctions between 2D materials are reviewed. Internal electric fields form in this type

of junction. The lateral junction is further divided into the junction between partly overlapped 2D materials and the 1D junction within one 2D film. Following that lateral junction between 2D materials, a review on the vertical junction between the 2D materials will be presented. As mentioned before, an accurate description of vertical stacked 2D materials requires treating the hybrid material as a new material. The charge transfer between the sheets results in some interesting phenomenon. Our review on junctions and contacts to 2D materials will finish with a review on metal contact to 2D materials. Both 1D and 2D contact between the metal and 2D materials will be discussed. However, the boundary between the junction and contact to 2D materials in different categories are not clear cut. For example, the lateral junction between partly overlapped 2D materials also involved the vertical junction at the overlapping region.

Lateral junction between 2D materials

The most commonly seen lateral junction is realized by partly overlapping two 2D materials. Graphene electrodes are reported to form good contact to multilayer MoS2 with a negligible Schottky barrier.[148] On the other hand, a significant Schottky barrier between graphene and multi-layer MoS_2 is also reported.[149] These contradictory results suggest complicated mechanisms behind the contact between overlapped graphene on MoS_2. This disagreement between different reports could be due to different density of trap states within the overlapping region, which is sensitive to the production and fabrication method.

The 1D junction between 2D materials would to a large extent solve the problems introduced from overlapping two different materials. A 1D homo-junction was realized by selectively doping part of the 2D material. A MoS2 diode was fabricated by chemically p dope the n-type MoS_2 with $AuCl_3$.[150] Half of the MoS_2 is covered by BN to shelter off from the dopant. A rectifying IV curve and close circuit photo current is measured after the doping that indicates the successful formation of p-n junction. A 1D Schottky junction between 1T and 2H phase of MoS_2 was fabricated by electron beam induced phase transformation.[151] Part of MoS_2 changes from semiconductor 2H phase to metallic 1T phase after the electron beam radiation. The current temperature measurement reveals that the current is proportional to $T^{\frac{3}{2}}$, which deviates from the current-temperature relation of conventional 2D Schottky junction but fits well with theoretical prediction for 1D junction. Another method to form 1D p-n junction between 2D materials is to grow a 2D hetero-structure directly by CVD. WSe_2 was epitaxially grown from the edge of MoS_2 directly to form an atomically sharp junction.[152] The rectifying IV curve and close circuit photo current confirms the existence of internal electrical field between MoS_2 and WSe_2. Similar epitaxial growth was also used to fabricate the 1D junction between MoS_2 and WS_2.[153]

Vertical junctions between 2D materials

Graphene-WS2-graphene vertical junction is first realized by stacking the exfoliated 2D materials together.[154] In this study, multilayer WS_2 was proposed as a tunnelling

layer for electrons between the two graphene electrodes. Band bending at the WS_2-graphene interface acts as the tunnelling barrier. Since the Fermi level of 2D materials is controlled by an external gate voltage, the effective junction can be tuned in the graphene-WS_2-graphene hybrid material by applying a gate voltage.[155] Photocurrent is measured in this system, which indicated an internal electric field induced by external gate voltage. By inserting a BN insulation layer between the graphene and WS_2, a light emission diode (LED) was fabricated.[156] The Fermi level of WS_2 was altered by the voltage applied to the graphene electrode and thus forming a junction between the top layer and bottom layer of the WS_2 flake. Electroluminescence was measured in this LED.

In addition to the vertical hetero-structures with graphene, vertical hetero-junctions between 2D TMDC materials are also widely studied. Hetero junction between WSe_2 and MoS_2 was observed by stacking these two materials together.[99] A rectifying behaviour in the IV curve was measured in this system. The existence of a p-n junction was further confirmed by the electroluminescence generated in this structure. It should be noted that the stronger electroluminescence emits from the edge of MoS_2 layer, but not uniform within the stacking region. This indicates that the recombination mainly happens around the edge. The photovoltaic effect of a similar structure was also studied.[157] The non-zero open circuit voltage confirms the existence of an internal electric field inside this heterojunction. Black phosphorus and monolayer MoS_2 are also reported to form heterojunctions.[158] The non-zero close

circuit current clearly indicate the existence of internal electric field in this system. It is noted that photo current at zero bias (i.e. close circuit current) was only generated within the region where black phosphorus stacks on MoS_2 but not the region with only MoS_2, which is evidence the inter electric field is formed vertically between black phosphorus and MoS_2. An ultrafast charge transfer in the WS_2/MoS_2 stacking hybrid was reported.[159] Time resolved photo luminescence study shows that the excited electron in MoS_2 can quickly transfer into the WS_2 layer in attach with the MoS2 layer and results in a quenching of the MoS_2's photo luminescence. Vertical p-n junction within one material formed in thin MoS_2 flakes is realized by p-doping one side of the MoS_2 with $AuCl_3$.[160] By tuning the back gate voltage, the device can work in electron, hole, or ambipolar transport region.

Metal contacts to 2D materials

Due to the 2D nature of monolayer materials they are sensitive to defects. Intrinsic defects in TMDC materials (MoS_2) are found to pin the Schottky barrier between the MoS_2 and metal contact.[161] This pinning effect results in a Schottky barrier irrelevant to the metal contact known as the "Bardeen model".[162] This is helpful to understand the complicated and sometimes even contradictory results reported by different groups. One way to reduce the influence of the Schottky barrier, no matter caused by trap states or band bending, is to add a thin insulation layer between metal contact and materials. Electrons would tunnel through the insulating layer. A thin MgO layer (2nm) is found to effectively inhibit the Schottky barrier between Co electrode and MoS_2

form 70meV to less than 10meV.[163] Due to the decreasing of the Schottky barrier, the MgO effectively decrease the contact resistance between Co electrode and monolayer MoS_2. Two phases, the semi-conductive 2H phase and metallic 1T phase, have been discovered in MoS_2 with Li doping. Phase engineering is used to lower the contact resistance between 2D materials and the metal contact.[164] Part of the MoS_2 crystal is doped and transformed into 1T phase so as to form better contact with metal electrode.

As mentioned, it would be ideal to form 1D contact to 2D material, which inhibit the effect of trap states existing on the materials surface. Edge contacts to graphene were found to decrease the contact resistance by about a quarter.[138] Epitaxial growth TMDC materials from graphene have also been explored.[100] Graphene was used as the metal contact in this study and an ohmic contact was found between TMDC materials and graphene.

2.4 2D Electronics and Optoelectronics

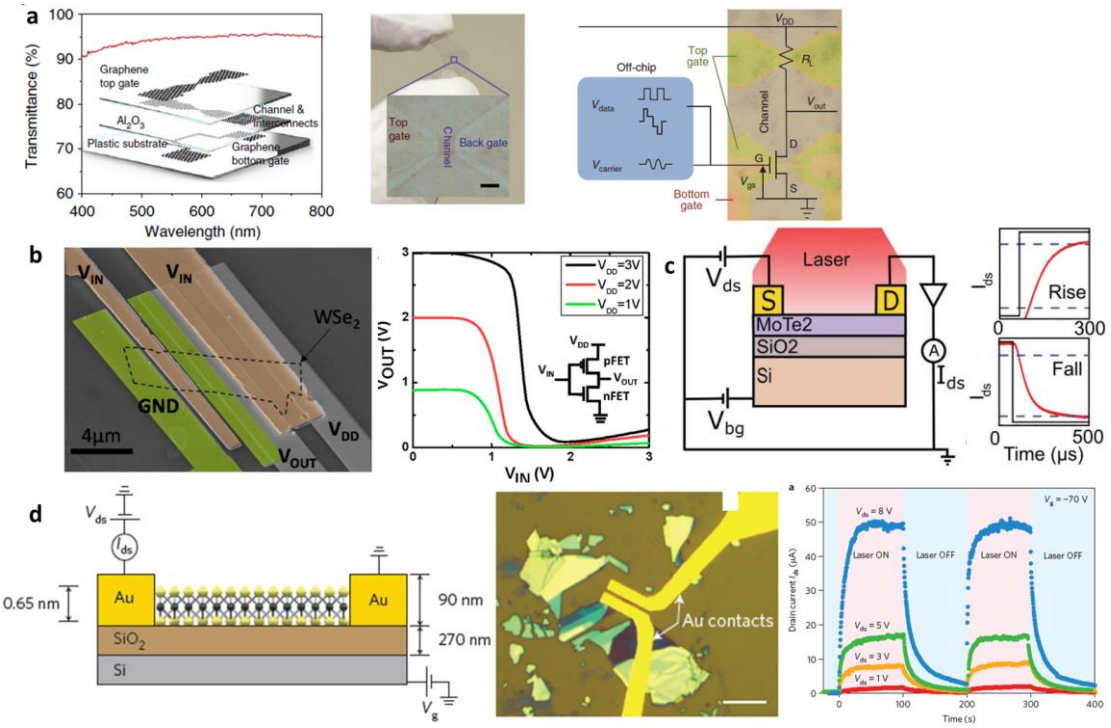


Figure 2-3 (a) All graphene flexible graphene circuit. The image is reprinted from reference[165]. (b) WSe_2 'NOT' gate. The left image in (b) is the output character of the device. The image is reprinted from reference[166]. (c)$MoTe_2$ photo detector. Good photo responsivity and fast response is realized in this device. The image is reprinted from reference[167]. (d) MoS_2 photo transistor. Photo responsivity is as high as 880A/W in this photo transistor. The image is reprinted from reference[168].

2.4.1 Influence of Measurement Environment

Electronic properties of 2D materials are much more sensitive to measurement environment compared with their 3D counterparts, which is due to the abundancy of trapped states as mentioned in section 2.3.3 of this thesis. In practice point of view, although such sensitivity to environment brings light to 2D gas sensor[123 169], shadow is cast on any device application due to the uncertainty and inconsistency between measurements. In this way, several major influential factors to the electronic and optoelectronic properties of 2D materials are discussed in this section before the review on real fabricated devices. Further discussion on our studies can be found in

section 4.3 in chapter 4 of this thesis.

Substrates and coating layer

Hexagonal Born-nitride (h-BN) is one of the best substrate for 2D electronic devices by providing a low-noise and hysteresis-free dielectric environment. It was found to boost the mobility of charge carriers in graphene more than 5 times compared with conventional SiO_2 substrate when measured in vacuum.[170] This is attributed to the Van-der-Waals self-cleaning effect between graphene and BN, which results in lower concentration of charge scatter centres on BN compared with SiO_2 substrate.

Similar as graphene, the humidity of the measurement environment was found to influence the measurement result of MoS_2 monolayer.[171] When moving from vacuum to an environment of 22% humidity, the conductivity of MoS2 diminished to almost zero within 29s. An encapsulation layer of Si_3N_4 was found to effectively lower the influence of environment humidity. Monolayer WS_2 was found to be almost insulating regardless the back gate voltage in ambient conditions.[146] However, a significant n-type transfer curve was measured under vacuum. The electronic performance was further improved after vacuum annealing. Encapsulating the single layer MoS_2 in HfO_2 was proven to be helpful in terms of approaching the theoretical mobility limit.[172] This could be a result of the dielectric screening effect to charge scatter centres. In addition to high κ materials, BN is another di-electric material that improves electronic behaviours of TMDC material. An additional BN layer under 4

layer WS_2 efficiently lowered the hysteresis in the field effect measurement of WS_2.[173] Charge stability map measured in 4.2K indicates a hopping transport mechanism of WS_2, which serve as direct evidence of the existence of trap states in the WS_2. By encapsulating the 2D TMDC in BN flakes, the charge carrier mobility is further improved. Few layer WSe_2 is encapsulated by two thick BN layers.[174] Very high motilities up to $750 cm^2 V^{-1} s^{-1}$ measured in this hybrid structure.

Ionic liquids provide an extremely large gate capacitance and thus alter the charge carrier concentration of 2D materials very effectively. Moreover, the measured 2D material is isolated from the environment and thus suffers less from extrinsic factors like water moisture. Monolayer MoS_2 exhibited ambipolar transfer behaviour, which is rarely observed without the help of ionic liquid gate.[175] The injection of electrons and holes form counter electrodes of this device, when working in ambipolar mode, was proven by the electroluminescence in this device.

Pre-treatments

Effects of annealing on transport properties on CVD grown MoS_2 has also been examined.[176] Similar to the exfoliated TMDC materials, it is found that a vacuum annealing is helpful to improve the electronic behaviour. The mobility was found to decrease with increasing temperature, with a highest mobility up to 200 measured around 10K.

In addition to annealing, surface treatment of the silicon chip also works to improve the performance of graphene. Functionalizing the silicon oxide layer with HMDS results in a much neutralized graphene and improves the mobility.[177] The surface of silicon chip becomes very hydrophobic after the HMDS processing and thus decreases the amount of adsorbed water. In this way, the graphene is less doped and the Dirac point appears near zero gate voltage.

2.4.2 Field Effect Transistors and Logic Circuits

This part of section 2.4 aims to review some progress in the study of 2D electronics. Similar to previous sections, graphene and materials in the TMDC family will be mainly discussed. The high charge carrier mobility of graphene is one major advantage of it over conventional materials in pursuing fast information processing. However, this advantage is undermined by an undesired large 'off' current due to the semimetal nature of graphene. Till now, most applications of graphene work to pick up high-frequency small-amplitude signal. On the other hand, although the charge carrier mobility with 2D TMDC is not outstanding, the on/off ratio of such materials can easily reach 10^6 or higher with an "off" current lower than nano-Ampere level. In this way, it is believed that 2D TMDC could find a position in logic circuits. In addition to these, 2D materials are blessed with many other properties like flexibility and space economy. All those properties provide 2D materials a good possibility to play an important role in the next generation of electronics. In this part, a general picture of nano-devices will be depicted first. The so called "short channel effect"

commonly found in the nano-devices will be discussed. After that, the applications of 2D materials in flexible electronics will be reviewed. This part of the review ends with a review on the high frequency and logic gate applications of 2D materials.

Nano-devices and short channel effect

With the ever more compact processing units in modern computers, the channel length of each field effect transistor is cut shorter and shorter. These "short channel effect" thus emerge: a set of parasitic effects that appear in FETs when shrinking the channel length shorter than several hundred nano-meters. The short channel effect can roughly be attributed to two major effects: drain induced barrier lower (DIBL) and punch through. The former is measured as a change of threshold voltage versus source drain bias, and the latter is measured as an increasing of "off" current when decreasing the channel length. To estimate the effect of DIBL, a "scaling channel length" is often used.[178]

$$\lambda = \sqrt{t_g t_{ch} \left(\frac{\epsilon_{ch}}{\epsilon_g}\right)} \qquad \text{eq. 2-14}$$

In eq. 2-14, λ is the scaling channel length, t_g is the thickness of the gate dielectric layer, t_{ch} is the thickness of semiconductor in the channel, ϵ_{ch} is the electric permittivity of the semiconductor and ϵ_g is the electric permittivity of the gate dielectric layer. eq. 2-14 provides a lower limit of channel length by considering the influence of the source-drain electrode to the Fermi level of channel material. Roughly speaking, eq. 2-14 describes when the field effect of source and drain

electrode would be as strong as the gate and thus gate losing its control over the channel material. Conventionally, high κ dielectric layers are used to increase ϵ_g in eq. 2-14 and thus decrease the channel length threshold. In the case of 2D materials, however, the t_{ch} is generally around 1nm, which enables another possibility to decrease the characteristic channel length. In this way, 2D materials are very attractive for device applications. Another commonly found short channel effect, punch through, is mostly determined by the depletion zone between materials. Since the physics of depletion zone in 2D materials are by nature very different from 3D material,[179] the review will focus on the experimental but not theoretical aspect of such features in FET.

FETs with 5nm thin MoS2 flake were fabricated with channel lengths down to 50nm.[180] Effective gate control of the conductance was maintained in the device even with a 300nm SiO_2 dielectric layer, which is generally inefficient for conventional short channel devices. The drain induce barrier lowering (DIBL) at 50nm channel length was measured at around $11V/V$ for 5nm thick MoS_2 in comparison with $24V/V$ for 12nm thick MoS_2. Despite a slight increase in the "off" current, no obvious punch through is discovered and the on/off ratio remains higher than 10^7. 15nm MoS_2 transistor has been developed with 4 layer MoS_2 contacted by graphene recently.[181] The on/off ratio maintains 10^7 in this device and the DIBL is measured as 0.7V/V with the 10nm HfO_2 dielectric layer. The DIBL in graphene based 2D FET

is represented by a shift of Dirac point at different source-drain bias.[182] A stronger shift of the Dirac point is found with smaller channel lengths.

Flexible electronics

The first proposed application of 2D materials in flexible electronics is to use as a flexible and transparent electrode. Graphene is one of most suitable materials for that task. Graphene touch screens have been fabricated and demonstrated to have better light transparency compared with ITO.[183] Moreover, it is also shown that such a transparent electrode is bendable and thus compatible with next generation soft electronics. The flexible graphene electrodes also find its role in the LED.[184] No significant degrade in performance of the LED is found after thousands of bending, which confirm the resilient of graphene electrodes.

Flexible field effect transistors have been fabricated using exfoliated 2D materials. A thin BN flake was used as the dielectric insulator between a graphene gate and MoS_2 semiconductor channel.[185] The whole device was fabricated on a flexible substrate. Bending experiments show that the device can bear 15% strain. Transistors made with graphene gate and channel have also been fabricated for signal modulation.[186]

High frequency electronics and logic circuits

One major thrust for graphene field effect transistor (FET) is making use of its high charge carrier mobility at room temperature. IBM researchers fabricated the graphene

transistors working at high frequency.[187] The graphene was epitaxially grown on SiC by thermal annealing. High κ material (HfO2) was used as the dielectric layer of top gate. Although the Hall mobility of the transistors vary from $900\text{cm}^2\text{V}^{-1}\text{s}^{-1}$ to $1520\text{cm}^2\text{V}^{-1}\text{s}^{-1}$, which is still far from the recorded highest mobility of graphene, the cut-off frequency exceeded 100GHz. CVD grown graphene is also found to show good high frequency electronic behaviours comparable with the epitaxial graphene.[188] In addition to monolayer graphene, there is theoretical and experimental evidence that an electric field tuneable band gap exist in bilayer graphene.[189] However, the dark current of bilayer graphene is still too large at room temperature even when a gate voltage is applied. Application of the small band gap in bilayer graphene is challenging. Recently radio frequency transistors with a small dark current were realized by black phosphorus.[190] The transistor proved to be able to process around a 20GHz signal.

Several types of logic circuits have been fabricated. An inverter (i.e. the NOT logic gate) is one of the simplest logic circuits, which inverts the input digit signal. High voltage input (i.e. signal '1') is transformed into low level voltage output (i.e. signal '0') and vice versa. Inverters based on WSe2 complementary FET have been fabricated.[166] Mechanically exfoliated p-type WSe2 was doped with potassium (K) atom at selected regions to form an n-p-n junction. The top gate was fabricated on the K doped region to form an n-type FET that makes the complementary logic circuit together with the p-type FET as its neighbour. The current-voltage gain of the circuit,

which indicate how quick the inverter is switched, is up to 12. A similar inverter but with slightly different geometry was fabricated with a MoS_2 monolayer with a high κ material as dielectric insulator.[191] The gain factor was 4 in this device. Based on the single layer MoS2 transistor, a NOR-gate logic circuit was fabricated. The NOR logic circuit have two inputs and will only export a high voltage level (signal '1'), when both inputs are of low voltage level (signal '0'). More complicated NAND logic gates and random access memory (SRAM) have also been fabricated on exfoliated bilayer MoS_2.[191] The output current of 2D logic circuits are still in their infancy, but they do provide new hopes to the semiconductor industry.

In addition to graphene and TMDC materials, other 2D materials have also attracted a lot of attention. Exfoliated thin black phosphorus flakes with mobility around $1000\text{cm}^2\text{V}^{-1}\text{s}^{-1}$ at room temperature were fabricated into FETs and exhibits on-off ratios around 10^5.[14] Hysteresis in the field effect measurement was also commonly found in the black phosphorus FET. Annealing and encapsulating the device in Al_2O_3 was found to be helpful in terms of decreasing the hysteresis.[192] Anisotropic electrical conductivity was discovered in multilayer black phosphorus. The conductivity of black phosphorus depends on the relative orientation between crystal and current. The hole mobility is large than the electron mobility[192] but smaller than the value reported for relatively thick black phosphrous[14].

2.4.3 Photodetectors with 2D materials

Many 2D materials are of direct band gap when in the monolayer form, which qualify them as competitive candidates for applications in photo sensing and energy conversion. In addition, 2D materials are generally of good transparency. 2D materials are thus believed to lead to the next-generation of high-space resolution and multifunctional photo detection facilities. Three major types of photodetectors are reviewed in this section according to their working mechanism. 2D photovoltaic devices that make use of an internal electric field are discussed first. Detectors based on this mechanism can also work as solar cells that convert light energy into electrical energy. 2D photoconductors are reviewed following the photovoltaic devices. The conductance of this kind of device changes when illuminated yet no open circuit voltage would generate, which is different to the photovoltaic devices. Mechanisms governing the photoconduction of 2D materials are complicated, but generally involve the appearance of trap states. Other photodetectors like avalanche photo detector or photodetectors based on photo-thermal-electrical effects will be reviewed in the final.

Photovoltaic photodetector and solar cells

Studies of graphene photo detectors emerged soon after its discovery. Although the zero-band gap of graphene results in a large dark current, it also enables a wide absorption spectrum. The graphene “photo detector” is thus generally used to pick-up radio frequency electromagnetic signals for communication applications. However it is still regarded as a photo detector due to a similar working mechanism. Graphene detectors based on the internal electric field within a graphene-metal junction were

fabricated for high speed optical communication.[193] Bilayer graphene was exfoliated onto silicon oxide with Pd and Ti contact as source and drain respectively. Pd (or Ti) is of higher (or lower) work function than graphene, and thus forms a Schottky junction with graphene. Different metals were used for the electrode on source or drain side and thus lead to opposite direction of band bending. This is confirmed by the reverse sign on the photo current when illuminating the graphene/Pd and graphene/Ti junction with a photo scanning microscope. The existence of an internal electric field is further proved by the close-circuit current when illuminated with light but without external bias. A linear increasing of photo current at low incident light intensity resulted in a photo responsivity of 1.5mA/W. Although the responsivity is not high, a high cut-off frequency of 16GHz was found. An ultrafast graphene photo detector was also realized with graphene contacted with two identical metal electrodes in a symmetric metal-semiconductor-metal (MSM) structure.[194] The close-circuit photo current thus depends on the illumination position. The photo responsivity remains around $10^2 \mu A/W$ with an on/off frequency as high as 40GHz. The decrease of responsivity under higher on/off frequency is actually due to the circuit geometry but not an intrinsic limitation of graphene. In this way, the operation frequency of graphene is expected to be even higher with a better designed circuit.

Different from graphene, TMDC materials are commonly used for conventional photo voltaic applications like photo detectors and solar cells due to the relative chemical stability, flexibility as well as direct band gap of monolayers.[195] Electron-hole pairs

generated by the incident photon are separated by the internal electric field so that they produce a photo-induced voltage drop in the device. This is called the photovoltaic effect. Photocurrent at zero-bias condition marks the separation of a photo-generated electron-hole pair separated by an internal electric field. An MoS_2 photo transistor making use of the photovoltaic effect was first fabricated in 2012 with exfoliated MoS_2.[196] The responsivity was extracted by linear fit of photo current against the incident light power, which was measured in the level of mA/W, with a response and recovery time around 50ms. The lack of internal gain and relative fast reaction and recovery time compared with high gain MoS_2 photo detectors indicate that the photo current generated in this device is likely caused by the separation of electron-hole pair by the internal electric field in the MoS_2-Ti junction. Contact metals with higher work functions (Au) were also used to provide a strong internal electric field.[197] Scanning photocurrent microscopy measurements show 2-order of magnitude increase of the photo current when illuminating on the Au-MoS_2 junction compared with when illuminating the bulk MoS_2. In addition to the metal-semiconductor junction, heterojunctions between 2D materials are another well studied structure for photo detection. Photo diodes with a heterojunction between p-type WSe_2 and n-type MoS_2 were fabricated by stacking multilayer MoS_2 onto WSe_2.[99] The asymmetric IV curve confirms the formation of a p-n junction in this system. The closed-circuit photo current is measured as $0.2\mu A$ when illuminated by $5\mu W$ light, which confirms the existence of an internal electric field within the heterojunction. Since the Fermi level of TMDC materials can be tuned by the external gate voltage, the internal electric

field can be generated with the help of local gating. Solar energy harvesting with this strategy was realized.[198]

The photovoltaic effect is generally accompanied by an internal gain, which means the apparent conversion rate of photon to electron is higher than unity. The internal gain is generally a result of the existence of trap states. This internal gain is measured in the photodetector with gold contacting to multilayer MoS_2. [199] A saturation of photo current was measured, which evidences the photocurrent was controlled by the number of photo induced electron-hole pairs. Internal gain was found to decrease when increasing the on/off frequency during measurement. This is attributed to the relative slow process to charge and discharge the trap states. A similar effect was also observed in multilayer MoS_2 in contact with Ti/Au electrode.[200] It should be noted that although the photo responsivity when a device is biased is magnified by the internal gain in 2D photo detectors induced by trap states, it has a negative influence on the photo energy conversion rate. In this way, it is not favourable for 2D solar cell applications.

In addition to TMDCs, other 2D photovoltaic detectors have been developed recently. Multilayer black phosphorus metal-semiconductor-meatal (MSM) photodetectors have been fabricated.[201] A small photo responsivity (4.8mA/W) but quick response (1ms) and recovery (4ms) time were discovered in the metal-black-phosphorus-metal photo detector. Because the same metal is used for the source and drain electrode no

close circuit current is measured. Photo conductors based on GaSe nano-sheet have also been studied.[202] The responsivity reached 2.8A/W, but the response time was slowed down to about 20ms and recovery time (300ms), which indicate the existence of trap states in such a system.

Photoconductors

2D photoconductors are another type of photo detector that make use of the photo-induced changes of conductance in 2D materials. The device is generally fabricated in the form of a transistor to utilize the gate-tuneable conductivity of 2D materials.[203] It should be noted that "photo transistor" is only used to describe the structure of the device, but not to hint the working mechanism.[203] As a matter of fact, many 2D photo transistors with a high gain factor work as a gate-controlled photo conductor but not photovoltaic detectors.

Graphene hybrid strictures are commonly used as photo-conductors with high internal gain. Photo responsivity, as high as $5 \times 10^8 \mathrm{A/W}$, was measured in hybrid staking of graphene on multilayer MoS_2.[104] A unipolar field effect was extracted from graphene on MoS_2, which is in contrast to the ambipolar transfer curve of graphene on insulation layer. A similar transfer curve was confirmed by other reports, which is due to the strong interaction between graphene and TMDC substrate.[204] [205] The existence of TMDC substrates in this case should apparently not be considered as merely a doping source, but the band structure of the hybrid material should be considered as a

whole. The high photo responsivity is in expense of a slow response and recovery process of the photo conductor with graphene-MoS_2 hybrid material. MoS_2 is proposed to trap holes of the photo excited electron hole pair and the release time is up to several minutes. Besides using MoS_2 as the layer to trap the hole, quantum dots can also play a similar role. Hybrid structures of PbS quantum dots decorated graphene were found to exhibit photo responsivity up to $10^7 A/W$.[206] Holes stimulated by incident phonons are injected into graphene leaving electrons trapped inside the quantum dots. Those quantum dots are thus negatively charged, and thus negatively gate the graphene underneath. This gating effect is measured as a positive shift of Dirac point in field effect transfer measurement. Different from the MoS_2 substrate, PbS quantum dots does not alter the shape of transfer curve of graphene very much.

High gain photo conductor with monolayer MoS_2 is fabricated by two groups almost at the same time in 2013.[207] [168] Li's group fabricated the MoS_2 photo detector with CVD grown continuous monolayer MoS2.[207] The MoS_2 is in Ohmic contact with the Ti layer of Ti/Au contact, which was measured as linear IV behaviour. Photo responsivity up to 2200A/W was achieved, which equals to a high gain factor of at least 5000. The high internal gain is explained by the intrinsic trap states in MoS_2, which induces persistent photo conductance. A similar result was achieved by Kis' group.[168] Different from Li's experiment, exfoliated monolayer MoS_2 is used with gold contacts. Photo responsivity up to 880A/W was measured. In both studies, a

negative dependence of the responsivity versus incident light intensity is revealed following a power law, however the power factor is measured as different values. Photo conductors with multilayer WS_2 as the photo sensing materials have also been fabricated.[208] Ti/Au contact were used and an Ohmic contact between Ti and multilayer WS_2 was found. The photo responsivity was measured as $92\mu A/W$. Similar to MoS_2, the dependence of photo current on incident light intensity of WS_2 follows a power law. For all experiments mentioned above, the power factor is measured smaller than one, which indicates decreasing photo responsivity with increasing illumination intensity. Very recently, a photo conductor with monolayer WS_2 with internal gain up to 200A/W was fabricated with CVD WS_2.[209] Different from experiments mentioned above, the Schottky barrier is found to govern the measured the two-terminal resistance. A light-induced Schottky barrier lowering is proposed to explain the large internal gain.

Surface adsorbates were found to influence the performance of the 2D photodetector by lowering the photo responsivity as well as slowing down the reaction time.[210] By encapsulating the MoS_2 inside a HfO_2 coating layer, the reaction and recovery time decreased to about one tenth of the original value while the responsivity increased more than two orders of magnitude and reached 50000A/W. The effect of the optoelectronic measurement environment was further tested by comparing the measurement of MoS_2 photo detectors in vacuum and ambient conditions. CVD grown MoS_2 monolayer was found to exhibit higher photo responsivity, but a slower

reaction and recovery when measured in vacuum compared to when measured in air.[207] [211] The photo response of thin WS_2 flake in different gas environment was also measured.[212] The photo responsivity was found to increase when the WS_2 flake was exposed to n dopant gas like NH_3.

Besides lateral structured photo detectors, vertical structured photo detectors are fabricated by stacking of 2D materials. The vertically stacked structure extends the photo sensing region from 1D junction to 2D area, which could help improvement of photo detection efficiency. Graphene-MoS_2-Graphene lateral photo detectors were realized by mechanical exfoliation and stacking method.[213] Thick MoS_2 flakes were sandwiched between the graphene layers, which enabled a large absorption rate of photons. The external quantum efficiency was found to be controlled by both external gate and light intensity. A Graphene-WS_2-Graphene vertical photo detector was also realized on a flexible substrate.[155] The high external quantum efficiency is attributed to the Van Hove singularity in the band structure of TMDC.

Photodetectors working by other mechanisms

Further to the two major mechanisms that have been reviewed, photo detection taking advantages of other mechanisms are also reported in the literature. Avalanche photo detectors based on InSe have been reported.[214] A high bias was applied to InSe to induce avalanche conduction when illuminated. Working mechanisms of such photodetectors are still unclear due to the very limited study on the impact ionization

of 2D materials. A photo-thermal-electric effect is reported to happen near the gate induced p-n junction in graphene.[215] An incident laser induces a temperature gradient near the junction, which further induces a Seebeck effect. A very interesting negative photo conductance is found in WS2-reduce-graphene-oxide hybrid materials.[216] When illuminated by infrared light, the conductivity of the hybrid material decreases. This effect can be understood as a result of charge carrier trapping by the reduced graphene oxide when the hybrid material is illuminated. Similar effects have been reported previously in nanoparticle decorated thin films.[217]

To address the problem of relative low intrinsic photo responsivity, while keeping a relatively quick response time of 2D material, one strategy is to increase the surface electromagnetic field strength of the light. This requires “concentrating” and “holding” the incident photon on the materials surface. Surface plasmonic enhancement on 2D materials is thus introduced for this purpose. Periodically placed gold dots were fabricated on the surface of graphene to enhance the surface electro-magnetic field of light.[218] Five-fold enhancement in photo responsivity was achieved when the incident light wavelength coupled with the plasmonic mode. By modifying the distance between gold particles the absorption peak in wavelength was changed, which realized the photo detection of multiple colours.[219] Another way to increase the light field strength is to make use of a micro-cavity to focus light on the materials. The photocurrent of graphene is significantly enhanced when the incident light is of the wavelength that couples with the Fabry−Pérot micro-cavity mode of the micro

cavity.[220] On chip graphene photo detectors covering a waveguide were also fabricated.[221] Photo detectors mentioned above generally have photo responsivity around 10mA/W, but a response rate quicker than GHz level.

Reference

(1) Yi, M.; Shen, Z. A Review on Mechanical Exfoliation for the Scalable Production of Graphene. *J. Mater. Chem. A* **2015**, *3*, 11700–11715.

(2) Bracamonte, M. V.; Lacconi, G. I.; Urreta, S. E.; Foa Torres, L. E. F. On the Nature of Defects in Liquid-Phase Exfoliated Graphene. *J. Phys. Chem. C* **2014**, *118*, 15455–15459.

(3) Eda, G.; Yamaguchi, H.; Voiry, D.; Fujita, T.; Chen, M.; Chhowalla, M. Photoluminescence from Chemically Exfoliated MoS 2. *Nano Lett.* **2011**, *11*, 5111–5116.

(4) Yan, Z.; Lin, J.; Peng, Z.; Sun, Z.; Zhu, Y.; Li, L.; Xiang, C.; Samuel, E. L.; Kittrell, C.; Tour, J. M. Toward the Synthesis of Wafer-Scale Single-Crystal Graphene on Copper Foils. *ACS Nano* **2012**, *6*, 9110–9117.

(5) Zhang, Y.; Zhang, Y.; Ji, Q.; Ju, J.; Yuan, H.; Shi, J.; Gao, T.; Ma, D.; Liu, M.; Chen, Y.; Song, X.; Hwang, H. Y.; Cui, Y.; Liu, Z. Controlled Growth of High-Quality Monolayer WS 2 Layers on Sapphire and Imaging Its Grain Boundary. *ACS Nano* **2013**, *7*, 8963–8971.

(6) Liu, K. K.; Zhang, W.; Lee, Y. H.; Lin, Y. C.; Chang, M. T.; Su, C. Y.; Chang, C. S.; Li, H.; Shi, Y.; Zhang, H.; Lai, C. S.; Li, L. J. Growth of Large-Area and

Highly Crystalline MoS 2 Thin Layers on Insulating Substrates. *Nano Lett.* **2012**, *12*, 1538–1544.

(7) de Heer, W. a.; Berger, C.; Ruan, M.; Sprinkle, M.; Li, X.; Hu, Y.; Zhang, B.; Hankinson, J.; Conrad, E. Large Area and Structured Epitaxial Graphene Produced by Confinement Controlled Sublimation of Silicon Carbide. *Proc. Natl. Acad. Sci.* **2011**, *108*, 16900–16905.

(8) Jiao, L.; Wang, X.; Diankov, G.; Wang, H.; Dai, H. Facile Synthesis of High-Quality Graphene Nanoribbons. *Nat. Nanotechnol.* **2010**, *5*, 321–325.

(9) Goler, S.; Piazza, V.; Roddaro, S.; Pellegrini, V.; Beltram, F.; Pingue, P. Self-Assembly and Electron-Beam-Induced Direct Etching of Suspended Graphene Nanostructures. *J. Appl. Phys.* **2011**, *110*.

(10) Magda, G. Z.; Pető, J.; Dobrik, G.; Hwang, C.; Biró, L. P.; Tapasztó, L. Exfoliation of Large-Area Transition Metal Chalcogenide Single Layers. *Sci. Rep.* **2015**, *5*, 14714.

(11) Novoselov, K. S. S.; Geim, A. K. K.; Morozov, S. V. V; Jiang, D.; Zhang, Y.; Dubonos, S. V. V; Grigorieva, I. V. V; Firsov, A. A. a. Electric Field Effect in Atomically Thin Carbon Films. *Science.* **2004**, *306*, 666.

(12) Novoselov, K. S.; Jiang, D.; Schedin, F.; Booth, T. J.; Khotkevich, V. V; Morozov, S. V; Geim, a K. Two-Dimensional Atomic Crystals. *Proc. Natl. Acad. Sci. U. S. A.* **2005**, *102*, 10451–10453.

(13) Liu, H.; Neal, A. T.; Zhu, Z.; Luo, Z.; Xu, X.; Tománek, D.; Ye, P. D. Phosphorene: An Unexplored 2D Semiconductor with a High Hole Mobility.

ACS Nano **2014**, *8*, 4033–4041.

(14) Li, L.; Yu, Y.; Ye, G. J.; Ge, Q.; Ou, X.; Wu, H.; Feng, D.; Chen, X. H.; Zhang, Y. Black Phosphorus Field-Effect Transistors. *Nat. Nanotechnol.* **2014**, *9*, 372–377.

(15) Gorbachev, R. V.; Riaz, I.; Nair, R. R.; Jalil, R.; Britnell, L.; Belle, B. D.; Hill, E. W.; Novoselov, K. S.; Watanabe, K.; Taniguchi, T.; Geim, A. K.; Blake, P. Hunting for Monolayer Boron Nitride: Optical and Raman Signatures. *Small* **2011**, *7*, 465–468.

(16) Geim, A. K. K.; Novoselov, K. S. S. The Rise of Graphene. *Nat. Mater.* **2007**, *6*, 183–191.

(17) Jayasena, B.; Subbiah, S. A Novel Mechanical Cleavage Method for Synthesizing Few-Layer Graphenes. *Nanoscale Res. Lett.* **2011**, *6*, 95.

(18) Chen, J.; Duan, M.; Chen, G. Continuous Mechanical Exfoliation of Graphene Sheets via Three-Roll Mill. *J. Mater. Chem.* **2012**, *22*, 19625.

(19) Hernandez, Y. *et al.* High-Yield Production of Graphene by Liquid-Phase Exfoliation of Graphite. *Nat. Nanotechnol.* **2008**, *3*, 563–568.

(20) Yi, M.; Shen, Z.; Zhang, X.; Ma, S. Achieving Concentrated Graphene Dispersions in Water/acetone Mixtures by the Strategy of Tailoring Hansen Solubility Parameters. *J. Phys. D. Appl. Phys.* **2013**, *46*, 25301.

(21) Lotya, M.; Hernandez, Y.; King, P. J.; Smith, R. J.; Nicolosi, V.; Karlsson, L. S.; Blighe, F. M.; De, S.; Zhiming, W.; McGovern, I. T.; Duesberg, G. S.; Coleman, J. N. Liquid Phase Production of Graphene by Exfoliation of Graphite in

Surfactant/water Solutions. *J. Am. Chem. Soc.* **2009**, *131*, 3611–3620.

(22) Bourlinos, A. B.; Georgakilas, V.; Zboril, R.; Sterioti, T. A.; Stubos, A. K. Liquid-Phase Exfoliation of Graphite Towards Solubilized Graphenes. *Small* **2009**, *5*, 1841–1845.

(23) Kim, J. *et al.* Direct Exfoliation and Dispersion of Two-Dimensional Materials in Pure Water via Temperature Control. *Nat. Commun.* **2015**, *6*, 8294.

(24) Coleman, J. N. *et al.* Two-Dimensional Nanosheets Produced by Liquid Exfoliation of Layered Materials. *Science.* **2011**, *331*, 568–571.

(25) Joensen, P.; Frindt, R. F.; Morrison, S. R. Single-Layer MoS2. *Mater. Res. Bull.* **1986**, *21*, 457–461.

(26) Fan, X.; Xu, P.; Zhou, D.; Sun, Y.; Li, Y. C.; Nguyen, M. A. T.; Terrones, M.; Mallouk, T. E. Fast and Efficient Preparation of Exfoliated 2H MoS 2 Nanosheets by Sonication-Assisted Lithium Intercalation and Infrared Laser-Induced 1T to 2H Phase Reversion. *Nano Lett.* **2015**, *15*, 5956–5960.

(27) Voiry, D.; Yamaguchi, H.; Li, J.; Silva, R.; Alves, D. C. B.; Fujita, T.; Chen, M.; Asefa, T.; Shenoy, V. B.; Eda, G.; Chhowalla, M. Enhanced Catalytic Activity in Strained Chemically Exfoliated WS2 Nanosheets for Hydrogen Evolution. *Nat. Mater.* **2013**, *12*, 850–855.

(28) Li, X.; Zhu, H. Two-Dimensional MoS2: Properties, Preparation, and Applications. *J. Mater.* **2015**, *1*, 33–44.

(29) Torrisi, F.; Hasan, T.; Wu, W.; Sun, Z.; Lombardo, A.; Kulmala, T. S.; Hsieh, G. W.; Jung, S.; Bonaccorso, F.; Paul, P. J.; Chu, D.; Ferrari, A. C. Inkjet-Printed

Graphene Electronics. *ACS Nano* **2012**, *6*, 2992–3006.

(30) Lotya, M.; Rakovich, A.; Donegan, J. F.; Coleman, J. N. Measuring the Lateral Size of Liquid-Exfoliated Nanosheets with Dynamic Light Scattering. *Nanotechnology* **2013**, *24*, 265703.

(31) Backes, C.; Paton, K. R.; Hanlon, D.; Yuan, S.; Katsnelson, M. I.; Houston, J.; Smith, R. J.; McCloskey, D.; Donegan, J. F.; Coleman, J. N. Spectroscopic Metrics Allow in Situ Measurement of Mean Size and Thickness of Liquid-Exfoliated Few-Layer Graphene Nanosheets. *Nanoscale* **2016**, *8*, 4311–4323.

(32) Zhang, Y.; Zhang, L.; Zhou, C. Review of Chemical Vapor Deposition of Graphene and Related Applications. *Acc. Chem. Res.* **2013**, *46*, 2329–2339.

(33) Marsh, H.; Warburton, a. P. Catalysis of Graphitisation. *J. Appl. Chem.* **2007**, *20*, 133–142.

(34) Adkins, H.; Cramer, H. The Use of Nickel as a Catalyst for Hydrogenation. *J. Am. Chem. Soc.* **1930**, *52*, 4349–4358.

(35) Yu, Q.; Lian, J.; Siriponglert, S.; Li, H.; Chen, Y. P.; Pei, S. S. Graphene Segregated on Ni Surfaces and Transferred to Insulators. *Appl. Phys. Lett.* **2008**, *93*, 6–9.

(36) Chae, S. J.; Güneş, F.; Kim, K. K.; Kim, E. S.; Han, G. H.; Kim, S. M.; Shin, H.; Yoon, S. M.; Choi, J. Y.; Park, M. H.; Yang, C. W.; Pribat, D.; Lee, Y. H. Synthesis of Large-Area Graphene Layers on Poly-Nickel Substrate by Chemical Vapor Deposition: Wrinkle Formation. *Adv. Mater.* **2009**, *21*, 2328–

2333.

(37) Addou, R.; Dahal, A.; Sutter, P.; Batzill, M. Monolayer Graphene Growth on Ni(111) by Low Temperature Chemical Vapor Deposition. *Appl. Phys. Lett.* **2012**, *100*, 8–11.

(38) Li, X.; Cai, W.; An, J.; Kim, S.; Nah, J.; Yang, D.; Piner, R.; Velamakanni, A.; Jung, I.; Tutuc, E.; Banerjee, S. K.; Colombo, L.; Ruoff, R. S. Large-Area Synthesis of High-Quality and Uniform Graphene Films on Copper Foils. *Science* **2009**, *324*, 1312–1314.

(39) Li, X. S.; Cai, W. W.; Colombo, L.; Ruoff, R. S. Evolution of Graphene Growth on Ni and Cu by Carbon Isotope Labeling. *Nano Lett.* **2009**, *9*, 4268–4272.

(40) Fang, W.; Hsu, A. L.; Song, Y.; Birdwell, A. G.; Amani, M.; Dubey, M.; Dresselhaus, M. S.; Palacios, T.; Kong, J. Asymmetric Growth of Bilayer Graphene on Copper Enclosures Using Low-Pressure Chemical Vapor Deposition. *ACS Nano* **2014**, *8*, 6491–6499.

(41) Han, G. H.; Güneş, F.; Bae, J. J.; Kim, E. S.; Chae, S. J.; Shin, H.-J. J.; Choi, J.-Y. Y.; Pribat, D.; Lee, Y. H. Influence of Copper Morphology in Forming Nucleation Seeds for Graphene Growth. *Nano Lett.* **2011**, *11*, 4144–4148.

(42) Au, C.-T.; Ng, C.-F.; Liao, M.-S. Methane Dissociation and Syngas Formation on Ru, Os, Rh, Ir, Pd, Pt, Cu, Ag, and Au: A Theoretical Study. *J. Catal.* **1999**, *185*, 12–22.

(43) Robertson, J. Heterogeneous Catalysis Model of Growth Mechanisms of Carbon Nanotubes, Graphene and Silicon Nanowires. *J. Mater. Chem.* **2012**, *22*,

19858.

(44) Gao, T.; Xie, S.; Gao, Y.; Liu, M.; Chen, Y.; Zhang, Y.; Liu, Z. Growth and Atomic-Scale Characterizations of Graphene on Multifaceted Textured Pt Foils Prepared by Chemical Vapor Deposition. *ACS Nano* **2011**, *5*, 9194–9201.

(45) Cushing, G. W.; Johánek, V.; Navin, J. K.; Harrison, I. Graphene Growth on Pt(111) by Ethylene Chemical Vapor Deposition at Surface Temperatures near 1000 K. *J. Phys. Chem. C* **2015**, *119*, 4759–4768.

(46) Gao, L.; Ren, W.; Xu, H.; Jin, L.; Wang, Z.; Ma, T.; Ma, L.-P.; Zhang, Z.; Fu, Q.; Peng, L.-M.; Bao, X.; Cheng, H.-M. Repeated Growth and Bubbling Transfer of Graphene with Millimetre-Size Single-Crystal Grains Using Platinum. *Nat. Commun.* **2012**, *3*, 699.

(47) Woo, Y. S.; Seo, D. H.; Yeon, D. H.; Heo, J.; Chung, H. J.; Benayad, A.; Chung, J. G.; Han, H.; Lee, H. S.; Seo, S.; Choi, J. Y. Low Temperature Growth of Complete Monolayer Graphene Films on Ni-Doped Copper and Gold Catalysts by a Self-Limiting Surface Reaction. *Carbon.* **2013**, *64*, 315–323.

(48) Wu, T.; Zhang, X.; Yuan, Q.; Xue, J.; Lu, G.; Liu, Z.; Wang, H. H.; Wang, H. H.; Ding, F.; Yu, Q.; Xie, X.; Jiang, M. Fast Growth of Inch-Sized Single-Crystalline Graphene from a Controlled Single Nucleus on Cu-Ni Alloys. *Nat. Mater.* **2015**, *15*, 43–47.

(49) Zhou, H.; Yu, W. J.; Liu, L.; Cheng, R.; Chen, Y.; Huang, X.; Liu, Y.; Wang, Y.; Huang, Y.; Duan, X. Chemical Vapour Deposition Growth of Large Single Crystals of Monolayer and Bilayer Graphene. *Nat. Commun.* **2013**, *4*, 2096.

(50) Hao, Y. *et al.* The Role of Surface Oxygen in the Growth of Large Single-Crystal Graphene on Copper. *Science* **2013**, *342*, 720–723.

(51) Wang, H.; Wang, G.; Bao, P.; Yang, S.; Zhu, W.; Xie, X.; Zhang, W.-J. Controllable Synthesis of Submillimeter Single-Crystal Monolayer Graphene Domains on Copper Foils by Suppressing Nucleation. *J. Am. Chem. Soc.* **2012**, *134*, 3627–3630.

(52) Kim, S. M.; Hsu, A.; Lee, Y.-H.; Dresselhaus, M.; Palacios, T.; Kim, K. K.; Kong, J. The Effect of Copper Pre-Cleaning on Graphene Synthesis. *Nanotechnology* **2013**, *24*, 365602.

(53) Wu, Y. A.; Fan, Y.; Speller, S.; Creeth, G. L.; Sadowski, J. T.; He, K.; Robertson, A. W.; Allen, C. S.; Warner, J. H. Large Single Crystals of Graphene on Melted Copper Using Chemical Vapor Deposition. *ACS Nano* **2012**, *6*, 5010–5017.

(54) Wu, B.; Geng, D.; Xu, Z.; Guo, Y.; Huang, L.; Xue, Y.; Chen, J.; Yu, G.; Liu, Y. Self-Organized Graphene Crystal Patterns. *NPG Asia Mater.* **2013**, *5*, e36.

(55) Fujita, J.; Ueki, R.; Miyazawa, Y.; Ichihashi, T. Graphitization at Interface between Amorphous Carbon and Liquid Gallium for Fabricating Large Area Graphene Sheets. *J. Vac. Sci. Technol. B Microelectron. Nanom. Struct.* **2009**, *27*, 3063.

(56) Zeng, M.; Tan, L.; Wang, J.; Chen, L.; R??mmeli, M. H.; Fu, L. Liquid Metal: An Innovative Solution to Uniform Graphene Films. *Chem. Mater.* **2014**, *26*, 3637–3643.

(57) Sun, J.; Zhang, Y.; Liu, Z. Direct Chemical Vapor Deposition Growth of Graphene on Insulating Substrates. *ChemNanoMat* **2016**, *2*, 9–18.

(58) Chen, X.; Wu, B.; Liu, Y. Direct Preparation of High Quality Graphene on Dielectric Substrates. *Chem. Soc. Rev.* **2016**, *45*, 2057–2074.

(59) Chen, J.; Wen, Y.; Guo, Y.; Wu, B.; Huang, L.; Xue, Y.; Geng, D.; Wang, D.; Yu, G.; Liu, Y. Oxygen-Aided Synthesis of Polycrystalline Graphene on Silicon Dioxide Substrates. *J. Am. Chem. Soc.* **2011**, *133*, 17548–17551.

(60) Rümmeli, M. H.; Bachmatiuk, A.; Scott, A.; Börrnert, F.; Warner, J. H.; Hoffman, V.; Lin, J. H.; Cuniberti, G.; Büchner, B. Direct Low-Temperature Nanographene Cvd Synthesis over a Dielectric Insulator. *ACS Nano* **2010**, *4*, 4206–4210.

(61) Lippert, G.; Dabrowski, J.; Yamamoto, Y.; Herziger, F.; Maultzsch, J.; Lemme, M. C.; Mehr, W.; Lupina, G. Molecular Beam Growth of Micrometer-Size Graphene on Mica. *Carbon.* **2013**, *52*, 40–48.

(62) Chen, J.; Guo, Y.; Jiang, L.; Xu, Z.; Huang, L.; Xue, Y.; Geng, D.; Wu, B.; Hu, W.; Yu, G.; Liu, Y. Near-Equilibrium Chemical Vapor Deposition of High-Quality Single-Crystal Graphene Directly on Various Dielectric Substrates. *Adv. Mater.* **2014**, *26*, 1348–1353.

(63) Sun, J.; Gao, T.; Song, X.; Zhao, Y.; Lin, Y.; Wang, H.; Ma, D.; Chen, Y.; Xiang, W.; Wang, J.; Zhang, Y.; Liu, Z. Direct Growth of High-Quality Graphene on High-κ Dielectric SrTiO3 Substrates. *J. Am. Chem. Soc.* **2014**, *136*, 6574–6577.

(64) Shi, Y.; Li, H.; Li, L. Recent Advances in Controlled Synthesis of

Two-Dimensional Transition Metal Dichalcogenides via Vapour Deposition Techniques. *Chem. Soc. Rev.* **2015**, *44*, 2744–2756.

(65) Feldman, Y.; Wasserman, E.; Srolovitz, D. J.; Tenne, R. High-Rate, Gas-Phase Growth of MoS2 Nested Inorganic Fullerenes and Nanotubes. *Science* **1995**, *267*, 222–225.

(66) Rong, Y.; Fan, Y.; Leen Koh, A.; Robertson, A. W.; He, K.; Wang, S.; Tan, H.; Sinclair, R.; Warner, J. H. Controlling Sulphur Precursor Addition for Large Single Crystal Domains of WS2. *Nanoscale* **2014**, *6*, 12096–12103.

(67) Wang, X.; Gong, Y.; Shi, G.; Chow, W. L.; Keyshar, K.; Ye, G.; Vajtai, R.; Lou, J.; Liu, Z.; Ringe, E.; Tay, B. K.; Ajayan, P. M. Chemical Vapor Deposition Growth of Crystalline Monolayer MoSe2. *ACS Nano* **2014**, *8*, 5125–5131.

(68) Zhou, H.; Wang, C.; Shaw, J. C.; Cheng, R.; Chen, Y.; Huang, X.; Liu, Y.; Weiss, N. O.; Lin, Z.; Huang, Y.; Duan, X. Large Area Growth and Electrical Properties of P-Type WSe 2 Atomic Layers. *Nano Lett.* **2015**, *15*, 709–713.

(69) Liu, B.; Fathi, M.; Chen, L.; Abbas, A.; Zhou, C. Chemical Vapor Deposition Growth of Monolayer WSe2 with Tunable Device Characteristics and Growth. *ACS Nano* **2015**, *9*, 6119–6127.

(70) Xu, Z.; Zhang, Y.; Lin, S.; Zheng, C.; Zhong, Y. L.; Xia, X.; Li, Z.; Sophia, P. J.; Fuhrer, M. S.; Cheng, Y.; Bao, Q. Synthesis and Transfer of Large-Area Monolayer WS2 Crystals : Moving Toward the Recyclable Use of Sapphire Substrates Synthesis and Transfer of Large-Area Monolayer WS 2 Crystals : Moving Toward the Recyclable Use of Sapphire Substrates. **2015**, 6178–6187.

(71) Kobayashi, Y.; Sasaki, S.; Mori, S.; Hibino, H.; Liu, Z.; Watanabe, K.; Taniguchi, T.; Suenaga, K.; Maniwa, Y.; Miyata, Y. Growth and Optical Properties of High-Quality Monolayer WS2 on Graphite. *ACS Nano* **2015**, *9*, 4056–4063.

(72) Yan, A.; Velasco, J.; Kahn, S.; Watanabe, K.; Taniguchi, T.; Wang, F.; Crommie, M. F.; Zettl, A. Direct Growth of Single- and Few-Layer MoS 2 on H-BN with Preferred Relative Rotation Angles. *Nano Lett.* **2015**, *15*, 6324–6331.

(73) Kim, S. M.; Hsu, A.; Park, M. H.; Chae, S. H.; Yun, S. J.; Lee, J. S.; Cho, D.-H.; Fang, W.; Lee, C.; Palacios, T.; Dresselhaus, M.; Kim, K. K.; Lee, Y. H.; Kong, J. Synthesis of Large-Area Multilayer Hexagonal Boron Nitride for High Material Performance. *Nat. Commun.* **2015**, *6*, 8662.

(74) Lee, Y. H.; Zhang, X. Q.; Zhang, W.; Chang, M. T.; Lin, C. Te; Chang, K. Di; Yu, Y. C.; Wang, J. T. W.; Chang, C. S.; Li, L. J.; Lin, T. W. Synthesis of Large-Area MoS 2 Atomic Layers with Chemical Vapor Deposition. *Adv. Mater.* **2012**, *24*, 2320–2325.

(75) Ling, X.; Lee, Y.; Lin, Y.; Fang, W.; Yu, L.; Dresselhaus, M. S.; Kong, J. Role of the Seeding Promoter in MoS 2 Growth by Chemical Vapor Deposition. *Nano Lett.* **2014**, *14*, 140129131422004.

(76) Lin, Y.-C.; Zhang, W.; Huang, J.-K.; Liu, K.-K.; Lee, Y.-H.; Liang, C.-T.; Chu, C.-W.; Li, L.-J. Wafer-Scale MoS2 Thin Layers Prepared by MoO3 Sulfurization. *Nanoscale* **2012**, *4*, 6637.

(77) Zhan, Y.; Liu, Z.; Najmaei, S.; Ajayan, P. M.; Lou, J. Large-Area Vapor-Phase

Growth and Characterization of MoS 2 Atomic Layers on a SiO 2 Substrate. *Small* **2012**, *8*, 966–971.

(78) Elı, A. L.; Terrones, H.; Pradhan, N. R.; Balicas, L.; Mallouk, T. E.; Lo, F.; Terrones, M. Controlled Synthesis and Transfer of Large-Area WS 2 Sheets : From Single Layer to Few Layers. **2013**, 5235–5242.

(79) Shi, Y.; Hamsen, C.; Jia, X.; Kim, K. K.; Reina, A.; Hofmann, M.; Hsu, A. L.; Zhang, K.; Li, H.; Juang, Z. Y.; Dresselhaus, M. S.; Li, L. J.; Kong, J. Synthesis of Few-Layer Hexagonal Boron Nitride Thin Film by Chemical Vapor Deposition. *Nano Lett.* **2010**, *10*, 4134–4139.

(80) Kim, K. K.; Hsu, A.; Jia, X.; Kim, S. M.; Shi, Y.; Hofmann, M.; Nezich, D.; Rodriguez-Nieva, J. F.; Dresselhaus, M.; Palacios, T.; Kong, J. Synthesis of Monolayer Hexagonal Boron Nitride on Cu Foil Using Chemical Vapor Deposition. *Nano Lett.* **2012**, *12*, 161–166.

(81) Xu, C.; Wang, L.; Liu, Z.; Chen, L.; Guo, J.; Kang, N.; Ma, X.-L.; Cheng, H.-M.; Ren, W. Large-Area High-Quality 2D Ultrathin Mo2C Superconducting Crystals. *Nat. Mater.* **2015**, *14*, 1135–1141.

(82) Berger, C.; Song, Z.; Li, T.; Li, X.; Ogbazghi, A. Y.; Feng, R.; Dai, Z.; Alexei, N.; Conrad, M. E. H.; First, P. N.; De Heer, W. A. Ultrathin Epitaxial Graphite: 2D Electron Gas Properties and a Route toward Graphene-Based Nanoelectronics. *J. Phys. Chem. B* **2004**, *108*, 19912–19916.

(83) Emtsev, K. V; Bostwick, A.; Horn, K.; Jobst, J.; Kellogg, G. L.; Ley, L.; McChesney, J. L.; Ohta, T.; Reshanov, S. a; Röhrl, J.; Rotenberg, E.; Schmid, A.

K.; Waldmann, D.; Weber, H. B.; Seyller, T. Towards Wafer-Size Graphene Layers by Atmospheric Pressure Graphitization of Silicon Carbide. *Nat. Mater.* **2009**, *8*, 203–207.

(84) Kosynkin, D. V; Higginbotham, A. L.; Sinitskii, A.; Lomeda, J. R.; Dimiev, A.; Price, B. K.; Tour, J. M. Longitudinal Unzipping of Carbon Nanotubes to Form Graphene Nanoribbons. *Nature* **2009**, *458*, 872–876.

(85) Yang, X.; Tang, S.; Ding, G.; Xie, X.; Jiang, M.; Huang, F. Layer-by-Layer Thinning of Graphene by Plasma Irradiation and Post-Annealing. *Nanotechnology* **2011**, *23*, 25704.

(86) Stankovich, S.; Dikin, D. A.; Dommett, G. H. B.; Kohlhaas, K. M.; Zimney, E. J.; Stach, E. A.; Piner, R. D.; Nguyen, S. T.; Ruoff, R. S. Graphene-Based Composite Materials. *Nature* **2006**, *442*, 282–286.

(87) Stankovich, S.; Dikin, D. A.; Piner, R. D.; Kohlhaas, K. A.; Kleinhammes, A.; Jia, Y.; Wu, Y.; Nguyen, S. T.; Ruoff, R. S. Synthesis of Graphene-Based Nanosheets via Chemical Reduction of Exfoliated Graphite Oxide. *Carbon.* **2007**, *45*, 1558–1565.

(88) Dave, S. H.; Gong, C.; Robertson, A. W.; Warner, J. H.; Grossman, J. C. Chemistry and Structure of Graphene Oxide via Direct Imaging. *ACS Nano* **2016**, *10*, 7515–7522.

(89) Bazargan, A. M.; Sharif, F.; Mazinani, S.; Naderi, N. Highly Conductive Reduced Graphene Oxide Transparent Ultrathin Film through Joule-Heat Induced Direct Reduction. *J. Mater. Sci. Mater. Electron.* **2016**.

(90) Yao, P.; Chen, P.; Jiang, L.; Zhao, H.; Zhu, H.; Zhou, D.; Hu, W.; Han, B. H.; Liu, M. Electric Current Induced Reduction of Graphene Oxide and Its Application as Gap Electrodes in Organic Photoswitching Devices. *Adv. Mater.* **2010**, *22*, 5008–5012.

(91) Ekiz, O. O.; Ürel, M.; Güner, H.; Mizrak, A. K.; Dâna, A. Reversible Electrical Reduction and Oxidation of Graphene Oxide. *ACS Nano* **2011**, *5*, 2475–2482.

(92) Loh, T. A. J.; Chua, D. H. C.; Wee, A. T. S. One-Step Synthesis of Few-Layer WS2 by Pulsed Laser Deposition. *Sci. Rep.* **2015**, *5*, 18116.

(93) Tan, L. K.; Liu, B.; Teng, J. H.; Guo, S.; Low, H. Y.; Loh, K. P. Atomic Layer Deposition of a MoS_2 Film. *Nanoscale* **2014**, *6*, 10584–10588.

(94) Castro Neto, A. H.; Guinea, F.; Peres, N. M. R.; Novoselov, K. S.; Geim, A. K. The Electronic Properties of Graphene. *Rev. Mod. Phys.* **2009**, *81*, 109–162.

(95) Lin, Y. C.; Teng, P. Y.; Yeh, C. H.; Koshino, M.; Chiu, P. W.; Suenaga, K. Structural and Chemical Dynamics of Pyridinic-Nitrogen Defects in Graphene. *Nano Lett.* **2015**, *15*, 7408–7413.

(96) Lin, Y. C.; Dumcenco, D. O.; Komsa, H. P.; Niimi, Y.; Krasheninnikov, A. V.; Huang, Y. S.; Suenaga, K. Properties of Individual Dopant Atoms in Single-Layer MoS2: Atomic Structure, Migration, and Enhanced Reactivity. *Adv. Mater.* **2014**, *26*, 2857–2861.

(97) Leenaerts, O.; Partoens, B.; Peeters, F. M. Adsorption of H2O, NH3, CO, NO2, and NO on Graphene: A First-Principles Study. *Phys. Rev. B* **2008**, *77*, 125416.

(98) Jing, Y.; Tan, X.; Zhou, Z.; Shen, P. Tuning Electronic and Optical Properties of

MoS 2 Monolayer via Molecular Charge Transfer. *J. Mater. Chem. A* **2014**, *2*, 16892–16897.

(99) Cheng, R.; Li, D.; Zhou, H.; Wang, C.; Yin, A.; Jiang, S.; Liu, Y.; Chen, Y.; Huang, Y.; Duan, X. Electroluminescence and Photocurrent Generation from Atomically Sharp WSe2/MoS2 Heterojunction P-N Diodes. *Nano Lett.* **2014**, *14*, 5590–5597.

(100) Guimarães, M. H. D.; Gao, H.; Han, Y.; Kang, K.; Xie, S.; Kim, C. J.; Muller, D. A.; Ralph, D. C.; Park, J. Atomically Thin Ohmic Edge Contacts between Two-Dimensional Materials. *ACS Nano* **2016**, *10*, 6392–6399.

(101) Wallace, P. R. The Band Theory of Graphite. *Phys. Rev.* **1947**, *71*, 622–634.

(102) Ashcroft, N. W.; Mermin, N. *Solid State Physics*; 1976.

(103) Castro Neto, a. H.; Peres, N. M. R.; Novoselov, K. S.; Geim, a. K. The Electronic Properties of Graphene. *Rev. Mod. Phys.* **2009**, *81*, 109–162.

(104) Geim, A. K.; Novoselov, K. S. The Rise of Graphene. *Nat. Mater.* **2007**, *6*, 183–191.

(105) Castellanos-Gomez, A. Black Phosphorus: Narrow Gap, Wide Applications. *J. Phys. Chem. Lett.* **2015**, *6*, 4280–4291.

(106) Kara, A.; Enriquez, H.; Seitsonen, A. P.; Lew Yan Voon, L. C.; Vizzini, S.; Aufray, B.; Oughaddou, H. A Review on Silicene - New Candidate for Electronics. *Surf. Sci. Rep.* **2012**, *67*, 1–18.

(107) Lebègue, S.; Eriksson, O. Electronic Structure of Two-Dimensional Crystals from Ab Initio Theory. *Phys. Rev. B - Condens. Matter Mater. Phys.* **2009**, *79*,

4–7.

(108) Kuc, A.; Zibouche, N.; Heine, T. Influence of Quantum Confinement on the Electronic Structure of the Transition Metal Sulfide TS2. *Phys. Rev. B* **2011**, *83*, 245213.

(109) Topsakal, M.; Aktürk, E.; Ciraci, S. First-Principles Study of Two- and One-Dimensional Honeycomb Structures of Boron Nitride. *Phys. Rev. B* **2009**, *79*, 115442.

(110) Kadantsev, E. S.; Hawrylak, P. Electronic Structure of a Single MoS 2 Monolayer. *Solid State Commun.* **2012**, *152*, 909–913.

(111) Zahid, F.; Liu, L.; Zhu, Y.; Wang, J.; Guo, H. A Generic Tight-Binding Model for Monolayer, Bilayer and Bulk MoS 2. *AIP Adv.* **2013**, *3*, 1–4.

(112) Bointon, T. H.; Jones, G. F.; De Sanctis, A.; Hill-Pearce, R.; Craciun, M. F.; Russo, S. Large-Area Functionalized CVD Graphene for Work Function Matched Transparent Electrodes. *Sci. Rep.* **2015**, *5*, 16464.

(113) Panchakarla, L. S.; Subrahmanyam, K. S.; Saha, S. K.; Govindaraj, A.; Krishnamurthy, H. R.; Waghmare, U. V.; Rao, C. N. R. Synthesis, Structure, and Properties of Boron- and Nitrogen-Doped Graphene. *Adv. Mater.* **2009**, *21*, 4726–4730.

(114) Wang, H.; Zhou, Y.; Wu, D.; Liao, L.; Zhao, S.; Peng, H.; Liu, Z. Synthesis of Boron-Doped Graphene Monolayers Using the Sole Solid Feedstock by Chemical Vapor Deposition. *Small* **2013**, *9*, 1316–1320.

(115) Wei, D.; Liu, Y.; Wang, Y.; Zhang, H.; Huang, L.; Yu, G. Synthesis of N-Doped

Graphene by Chemical Vapor Deposition and Its Electrical Properties. *Nano Lett.* **2009**, *9*, 1752–1758.

(116) Jeong, H. M.; Lee, J. W.; Shin, W. H.; Choi, Y. J.; Shin, H. J.; Kang, J. K.; Choi, J. W. Nitrogen-Doped Graphene for High-Performance Ultracapacitors and the Importance of Nitrogen-Doped Sites at Basal Planes. *Nano Lett.* **2011**, *11*, 2472–2477.

(117) Baglio, J.; Kamieniecki, E.; DeCola, N.; Struck, C.; Marzik, J.; Dwight, K.; Wold, A. Growth and Characterization of N-WS2 and Niobium-Doped P-WS2 Single Crystals. *J. Solid State Chem.* **1983**, *49*, 166–179.

(118) Yang, L.; Majumdar, K.; Liu, H.; Du, Y.; Wu, H.; Hatzistergos, M.; Hung, P. Y.; Tieckelmann, R.; Tsai, W.; Hobbs, C.; Ye, P. D. Chloride Molecular Doping Technique on 2D Materials: WS 2 and MoS 2. *Nano Lett.* **2014**, *14*, 6275–6280.

(119) Nipane, A.; Karmakar, D.; Kaushik, N.; Karande, S.; Lodha, S. Few-Layer MoS 2 P -Type Devices Enabled by Selective Doping Using Low Energy Phosphorus Implantation. *ACS Nano* **2016**, *10*, 2128–2137.

(120) Suh, J.; Park, T. E.; Lin, D. Y.; Fu, D.; Park, J.; Jung, H. J.; Chen, Y.; Ko, C.; Jang, C.; Sun, Y.; Sinclair, R.; Chang, J.; Tongay, S.; Wu, J. Doping against the Native Propensity of MoS2: Degenerate Hole Doping by Cation Substitution. *Nano Lett.* **2014**, *14*, 6976–6982.

(121) Chen, Y.; Xi, J.; Dumcenco, D. O.; Liu, Z.; Suenaga, K.; Wang, D.; Shuai, Z.; Huang, Y. S.; Xie, L. Tunable Band Gap Photoluminescence from Atomically

Thin Transition-Metal Dichalcogenide Alloys. *ACS Nano* **2013**, *7*, 4610–4616.

(122) Chen, J.-H.; Jang, C.; Adam, S.; Fuhrer, M. S.; Williams, E. D.; Ishigami, M. Charged-Impurity Scattering in Graphene. *Nat. Phys.* **2008**, *4*, 377–381.

(123) Schedin, F.; Geim, A. K.; Morozov, S. V; Hill, E. W.; Blake, P.; Katsnelson, M. I.; Novoselov, K. S. Detection of Individual Gas Molecules Adsorbed on Graphene. *Nat. Mater.* **2007**, *6*, 652–655.

(124) Kumar, B.; Min, K.; Bashirzadeh, M.; Farimani, a B.; Bae, M. H.; Estrada, D.; Kim, Y. D.; Yasaei, P.; Park, Y. D.; Pop, E.; Aluru, N. R.; Salehi-Khojin, a. The Role of External Defects in Chemical Sensing of Graphene Field-Effect Transistors. *Nano Lett.* **2013**, *13*, 1962–1968.

(125) Wang, X.; Li, X.; Zhang, L.; Yoon, Y.; Weber, P. K.; Wang, H.; Guo, J.; Dai, H. N-Doping of Graphene through Electrothermal Reactions with Ammonia. *Science.* **2009**, *324*, 768–771.

(126) Chen, W.; Chen, S.; Dong, C. Q.; Xing, Y. G.; Wee, A. T. S. Surface Transfer P-Type Doping of Epitaxial Graphene. *J. Am. Chem. Soc.* **2007**, *129*, 10418–10422.

(127) Khalil, H. M. W.; Khan, M. F.; Eom, J.; Noh, H. Highly Stable and Tunable Chemical Doping of Multilayer WS2 Field Effect Transistor: Reduction in Contact Resistance. *ACS Appl. Mater. Interfaces* **2015**, *7*, 23589–23596.

(128) Iqbal, M. W.; Iqbal, M. Z.; Khan, M. F.; Kamran, M. A.; Majid, A.; Alharbi, T.; Eom, J. Tailoring the Electrical and Photo-Electrical Properties of a WS2 Field Effect Transistor by Selective N-Type Chemical Doping. *RSC Adv.* **2016**, *6*,

24675–24682.

(129) Liu, B.; Chen, L.; Liu, G.; Abbas, A. N.; Fathi, M.; Zhou, C. High-Performance Chemical Sensing Using Schottky-Contacted Chemical Vapor Deposition Grown Monolayer MoS2 Transistors. *ACS Nano* **2014**, *8*, 5304–5314.

(130) Iqbal, M. W.; Iqbal, M. Z.; Khan, M. F.; Shehzad, M. A.; Seo, Y.; Eom, J. Deep-Ultraviolet-Light-Driven Reversible Doping of WS2 Field-Effect Transistors. *Nanoscale* **2014**, *7*, 747–757.

(131) Mouri, S.; Miyauchi, Y.; Matsuda, K. Tunable Photoluminescence of Monolayer MoS2 via Chemical Doping. *Nano Lett.* **2013**, *13*, 5944–5948.

(132) Tan, H.; Fan, Y.; Rong, Y.; Porter, B.; Lau, C. S.; Zhou, Y.; He, Z.; Wang, S.; Bhaskaran, H.; Warner, J. H. Doping Graphene Transistors Using Vertical Stacked Monolayer WS 2 Heterostructures Grown by Chemical Vapor Deposition. *ACS Appl. Mater. Interfaces* **2016**, *8*, 1644–1652.

(133) Robin, A.; Lhuillier, E.; Xu, X. Z.; Ithurria, S.; Aubin, H.; Ouerghi, A.; Dubertret, B. Engineering the Charge Transfer in All 2D Graphene-Nanoplatelets Heterostructure Photodetectors. *Sci. Rep.* **2016**, *6*, 24909.

(134) Seeger, K. *Semiconductor Physics*; Advanced Texts in Physics; Springer Berlin Heidelberg: Berlin, Heidelberg, 2004.

(135) Kalb, W. L.; Batlogg, B. Calculating the Trap Density of States in Organic Field-Effect Transistors from Experiment: A Comparison of Different Methods. *Phys. Rev. B - Condens. Matter Mater. Phys.* **2010**, *81*, 1–13.

(136) Najam, F.; Tan, M. L. P.; Ismail, R.; Seop Yu, Y. Two-Dimensional (2D) Transition Metal Dichalcogenide Semiconductor Field-Effect Transistors: The Interface Trap Density Extraction and Compact Model. *Semicond. Sci. Technol.* **2015**, *30*, 75010.

(137) Kim, H.; Song, I.; Park, C.; Son, M.; Hong, M.; Kim, Y.; Kim, J. S.; Shin, H. J.; Baik, J.; Choi, H. C. Copper-Vapor-Assisted Chemical Vapor Deposition for High-Quality and Metal-Free Single-Layer Graphene on Amorphous SiO2 Substrate. *ACS Nano* **2013**, *7*, 6575–6582.

(138) Wang, L.; Meric, I.; Huang, P. Y.; Gao, Q.; Gao, Y.; Tran, H.; Taniguchi, T.; Watanabe, K.; Campos, L. M.; Muller, D. A.; Guo, J.; Kim, P.; Hone, J.; Shepard, K. L.; Dean, C. R. One-Dimensional Electrical Contact to a Two-Dimensional Material. *Science.* **2013**, *342*, 614–617.

(139) Bolotin, K. I.; Sikes, K. J.; Jiang, Z.; Klima, M.; Fudenberg, G.; Hone, J.; Kim, P.; Stormer, H. L. Ultrahigh Electron Mobility in Suspended Graphene. *Solid State Commun.* **2008**, *146*, 351–355.

(140) Mayorov, A. S.; Gorbachev, R. V; Morozov, S. V; Britnell, L.; Jalil, R.; Ponomarenko, L. a; Blake, P.; Novoselov, K. S.; Watanabe, K.; Taniguchi, T.; Geim, a. K. Micrometer-Scale Ballistic Transport in Encapsulated Graphene at Room Temperature. *Nano Lett.* **2011**, *11*, 2396–2399.

(141) Paniagua, S. a.; Baltazar, J.; Sojoudi, H.; Mohapatra, S. K.; Zhang, S.; Henderson, C. L.; Graham, S.; Barlow, S.; Marder, S. R. Production of Heavily N- and P-Doped CVD Graphene with Solution-Processed Redox-Active

Metal–organic Species. *Mater. Horiz.* **2014**, *1*, 111–115.

(142) Hwang, J.-Y.; Kuo, C.-C.; Chen, L.-C.; Chen, K.-H. Correlating Defect Density with Carrier Mobility in Large-Scaled Graphene Films: Raman Spectral Signatures for the Estimation of Defect Density. *Nanotechnology* **2010**, *21*, 465705.

(143) Chen, J. H.; Cullen, W. G.; Jang, C.; Fuhrer, M. S.; Williams, E. D. Defect Scattering in Graphene. *Phys. Rev. Lett.* **2009**, *102*, 1–4.

(144) Zhu, W.; Low, T.; Lee, Y. H.; Wang, H.; Farmer, D. B.; Kong, J.; Xia, F.; Avouris, P. Electronic Transport and Device Prospects of Monolayer Molybdenum Disulphide Grown by Chemical Vapour Deposition. *Nat Commun* **2014**, *5*, 3087.

(145) Liu, D.; Guo, Y.; Fang, L.; Robertson, J. Sulfur Vacancies in Monolayer MoS2 and Its Electrical Contacts. *Appl. Phys. Lett.* **2013**, *103*.

(146) Ovchinnikov, D.; Allain, A.; Huang, Y.; Dumcenco, D.; Kis, A. Electrical Transport Properties of Single-Layer WS2. *ACS Nano* **2014**, *8*, 8174–8181.

(147) Qiu, H.; Xu, T.; Wang, Z.; Ren, W.; Nan, H.; Ni, Z.; Chen, Q.; Yuan, S.; Miao, F.; Song, F.; Long, G.; Shi, Y.; Sun, L.; Wang, J.; Wang, X. Hopping Transport through Defect-Induced Localized States in Molybdenum Disulphide. *Nat. Commun.* **2013**, *4*, 2642.

(148) Liu, Y.; Wu, H.; Cheng, H. C.; Yang, S.; Zhu, E.; He, Q.; Ding, M.; Li, D.; Guo, J.; Weiss, N. O.; Huang, Y.; Duan, X. Toward Barrier Free Contact to Molybdenum Disulfide Using Graphene Electrodes. *Nano Lett.* **2015**, *15*,

3030–3034.

(149) Tian, H.; Tan, Z.; Wu, C.; Wang, X.; Mohammad, M. A.; Xie, D.; Yang, Y.; Wang, J.; Li, L.-J.; Xu, J.; Ren, T.-L. Novel Field-Effect Schottky Barrier Transistors Based on Graphene-MoS2 Heterojunctions. *Sci. Rep.* **2014**, *4*, 5951.

(150) Choi, M. S.; Qu, D.; Lee, D.; Liu, X.; Watanabe, K.; Taniguchi, T.; Yoo, W. J. Lateral MoS2 P-N Junction Formed by Chemical Doping for Use in High-Performance Optoelectronics. *ACS Nano* **2014**, *8*, 9332–9340.

(151) Katagiri, Y.; Nakamura, T.; Ishii, A.; Ohata, C.; Hasegawa, M.; Katsumoto, S.; Cusati, T.; Fortunelli, A.; Iannaccone, G.; Fiori, G.; Roche, S.; Haruyama, J. Gate-Tunable Atomically Thin Lateral MoS $_2$ Schottky Junction Patterned by Electron Beam. *Nano Lett.* **2016**, acs.nanolett.6b01186.

(152) Li, M.-Y.; Shi, Y.; Cheng, C.-C.; Lu, L.-S.; Lin, Y.-C.; Tang, H.-L.; Tsai, M.-L.; Chu, C.-W.; Wei, K.-H.; He, J.-H.; Chang, W.-H.; Suenaga, K.; Li, L.-J. Epitaxial Growth of a Monolayer WSe2-MoS2 Lateral P-N Junction with an Atomically Sharp Interface. *Science.* **2015**, *349*, 524–528.

(153) Chen, K.; Wan, X.; Wen, J.; Xie, W.; Kang, Z.; Zeng, X.; Chen, H.; Xu, J. Bin. Electronic Properties of MoS2-WS2 Heterostructures Synthesized with Two-Step Lateral Epitaxial Strategy. *ACS Nano* **2015**, *9*, 9868–9876.

(154) Georgiou, T.; Jalil, R.; Belle, B. D.; Britnell, L.; Gorbachev, R. V; Morozov, S. V; Kim, Y.-J.; Gholinia, A.; Haigh, S. J.; Makarovsky, O.; Eaves, L.; Ponomarenko, L. a; Geim, A. K.; Novoselov, K. S.; Mishchenko, A. Vertical Field-Effect Transistor Based on Graphene-WS2 Heterostructures for Flexible

and Transparent Electronics. *Nat. Nanotechnol.* **2013**, *8*, 100–103.

(155) Britnell, L.; Ribeiro, R. M.; Eckmann, A.; Jalil, R.; Belle, B. D.; Mishchenko, A.; Kim, Y.-J.; Gorbachev, R. V; Georgiou, T.; Morozov, S. V; Grigorenko, a N.; Geim, a K.; Casiraghi, C.; Neto, A. H. C.; Novoselov, K. S. Strong Light-Matter Interactions in Heterostructures of Atomically Thin Films. *Science.* **2013**, *340*, 1311–1314.

(156) Withers, F.; Del Pozo-Zamudio, O.; Mishchenko, A.; Rooney, a. P.; Gholinia, A.; Watanabe, K.; Taniguchi, T.; Haigh, S. J.; Geim, a. K.; Tartakovskii, a. I.; Novoselov, K. S. Light-Emitting Diodes by Band-Structure Engineering in van Der Waals Heterostructures. *Nat. Mater.* **2015**, *14*, 301–306.

(157) Furchi, M. M.; Pospischil, A.; Libisch, F.; Burgdörfer, J.; Mueller, T. Photovoltaic Effect in an Electrically Tunable Van Der Waals Heterojunction. *Nano Lett.* **2014**, *14*, 4785–4791.

(158) Deng, Y.; Luo, Z.; Conrad, N. J.; Liu, H.; Gong, Y.; Najmaei, S.; Ajayan, P. M.; Lou, J.; Xu, X.; Ye, P. D. Black Phosphorus–Monolayer MoS 2 van Der Waals Heterojunction P–n Diode. *ACS Nano* **2014**, *8*, 8292–8299.

(159) Hong, X.; Kim, J.; Shi, S.-F.; Zhang, Y.; Jin, C.; Sun, Y.; Tongay, S.; Wu, J.; Zhang, Y.; Wang, F. Ultrafast Charge Transfer in Atomically Thin MoS2/WS2 Heterostructures. *Nat. Nanotechnol.* **2014**, *9*, 1–5.

(160) Li, H.-M.; Lee, D.; Qu, D.; Liu, X.; Ryu, J.; Seabaugh, A.; Yoo, W. J. Ultimate Thin Vertical P-N Junction Composed of Two-Dimensional Layered Molybdenum Disulfide. *Nat. Commun.* **2015**, *6*, 6564.

(161) Mcdonnell, S.; Addou, R.; Buie, C.; Wallace, R. M.; Hinkle, C. L. Defect-Dominated Doping and Contact Resistance in MoS 2. *ACS Nano* **2014**, *8*, 2880–2888.

(162) Bardeen, J. Surface States and Rectification at a Metal Semi-Conductor Contact. *Phys. Rev.* **1947**, *71*, 717–727.

(163) Chen, J.; Odenthal, P. M.; Swartz, A. G.; Floyd, G. C.; Wen, H.; Luo, K. Y.; Kawakami, R. K. Control of Schottky Barriers in Single Layer MoS2 Transistors with Ferromagnetic Contacts. *Nano Lett.* **2013**, *13*, 3106–3110.

(164) Kappera, R.; Voiry, D.; Yalcin, S. E.; Branch, B.; Gupta, G.; Mohite, A. D.; Chhowalla, M. Phase-Engineered Low-Resistance Contacts for Ultrathin MoS2 Transistors. *Nat. Mater.* **2014**, *13*, 1–15.

(165) Lee, S.; Lee, K.; Liu, C.-H.; Kulkarni, G. S.; Zhong, Z. Flexible and Transparent All-Graphene Circuits for Quaternary Digital Modulations. *Nat. Commun.* **2012**, *3*, 1018.

(166) Tosun, M.; Chuang, S.; Fang, H.; Sachid, A. B.; Hettick, M.; Lin, Y.; Zeng, Y.; Javey, A. High-Gain Inverters Based on WSe2 Complementary Field-Effect Transistors. *ACS Nano* **2014**, *8*, 4948–4953.

(167) Octon, T. J.; Nagareddy, V. K.; Russo, S.; Craciun, M. F.; Wright, C. D. Fast High-Responsivity Few-Layer MoTe 2 Photodetectors. *Adv. Opt. Mater.* **2016**, 1–5.

(168) Lopez-Sanchez, O.; Lembke, D.; Kayci, M.; Radenovic, A.; Kis, A. Ultrasensitive Photodetectors Based on Monolayer MoS2. *Nat. Nanotechnol.*

2013, *8*, 497–501.

(169) Li, H.; Yin, Z.; He, Q.; Li, H.; Huang, X.; Lu, G.; Fam, D. W. H.; Tok, A. I. Y.; Zhang, Q.; Zhang, H. Fabrication of Single- and Multilayer MoS2 Film-Based Field-Effect Transistors for Sensing NO at Room Temperature. *Small* **2012**, *8*, 63–67.

(170) Gannett, W.; Regan, W.; Watanabe, K.; Taniguchi, T.; Crommie, M. F.; Zettl, a. Boron Nitride Substrates for High Mobility Chemical Vapor Deposited Graphene. *Appl. Phys. Lett.* **2011**, *98*, 242105.

(171) Late, D. J.; Liu, B.; Matte, H. S. S. R.; Dravid, V. P.; Rao, C. N. R. Hysteresis in Single-Layer MoS2 Field Effect Transistors. *ACS Nano* **2012**, *6*, 5635–5641.

(172) Radisavljevic, B.; Radenovic, A.; Brivio, J.; Giacometti, V.; Kis, A. Single-Layer MoS2 Transistors. *Nat. Nanotechnol.* **2011**, *6*, 147–150.

(173) Withers, F.; Bointon, T. H.; Hudson, D. C.; Craciun, M. F.; Russo, S. Electron Transport of WS2 Transistors in a Hexagonal Boron Nitride Dielectric Environment. *Sci. Rep.* **2014**, *4*, 4967.

(174) Wang, J. I. J.; Yang, Y.; Chen, Y. A.; Watanabe, K.; Taniguchi, T.; Churchill, H. O. H.; Jarillo-Herrero, P. Electronic Transport of Encapsulated Graphene and WSe2 Devices Fabricated by Pick-up of Prepatterned hBN. *Nano Lett.* **2015**, *15*, 1898–1903.

(175) Jo, S.; Ubrig, N.; Berger, H.; Kuzmenko, A. B.; Morpurgo, A. F. Mono- and Bilayer WS2 Light-Emitting Transistors. *Nano Lett.* **2014**, *14*, 2019–2025.

(176) Schmidt, H.; Wang, S.; Chu, L.; Toh, M.; Kumar, R.; Zhao, W.; Neto, a H. C.;

Martin, J.; Adam, S.; Özyilmaz, B.; Eda, G. Transport Properties of Monolayer MoS2 Grown by Chemical Vapor Deposition. *Nano Lett.* **2014**, *14*, 1909–1913.

(177) Chowdhury, S. F.; Sonde, S.; Rahimi, S.; Tao, L.; Banerjee, S.; Akinwande, D. Improvement of Graphene Field-Effect Transistors by Hexamethyldisilazane Surface Treatment. *Appl. Phys. Lett.* **2014**, *105*, 2012–2017.

(178) Chhowalla, M.; Jena, D.; Zhang, H. Two-Dimensional Semiconductors for Transistors. *Nat. Rev. Mater.* **2016**, *1*, 16052.

(179) Yu, H.; Kutana, A.; Yakobson, B. I. Carrier Delocalization in Two-Dimensional Coplanar P–n Junctions of Graphene and Metal Dichalcogenides. *Nano Lett.* **2016**, acs.nanolett.6b01822.

(180) Liu, H.; Neal, A. T.; Ye, P. D. Channel Length Scaling of MoS_2 MOSFETs. *ACS Nano* **2012**, *6*, 8563–8569.

(181) Nourbakhsh, A.; Zubair, A.; Huang, S.; Ling, X.; Dresselhaus, M. S.; Kong, J.; De Gendt, S.; Palacios, T. 15-Nm Channel Length MoS2 FETs with Single- and Double-Gate Structures. In *2015 Symposium on VLSI Technology (VLSI Technology)*; IEEE, 2015; Vol. 2015–Augus, pp. T28–T29.

(182) Han, S. J.; Chen, Z.; Bol, A. A.; Sun, Y. Channel-Length-Dependent Transport Behaviors of Graphene Field-Effect Transistors. *IEEE Electron Device Lett.* **2011**, *32*, 812–814.

(183) Ryu, J.; Kim, Y.; Won, D.; Kim, N.; Park, J. S.; Lee, E. K.; Cho, D.; Cho, S. P.; Kim, S. J.; Ryu, G. H.; Shin, H. A. S.; Lee, Z.; Hong, B. H.; Cho, S. Fast Synthesis of High-Performance Graphene Films by Hydrogen-Free Rapid

Thermal Chemical Vapor Deposition. *ACS Nano* **2014**, *8*, 950–956.

(184) Torres Alonso, E.; Karkera, G.; Jones, G. F.; Craciun, M. F.; Russo, S. Homogeneously Bright, Flexible, and Foldable Lighting Devices with Functionalized Graphene Electrodes. *ACS Appl. Mater. Interfaces* **2016**, *8*, 16541–16545.

(185) Lee, G.-H.; Yu, Y.-J.; Cui, X.; Petrone, N.; Lee, C.-H. C.; Choi, M. S.; Lee, D.-Y.; Lee, C.-H. C.; Yoo, W. J.; Watanabe, K.; Taniguchi, T.; Nuckolls, C.; Kim, P.; Hone, J. Flexible and Transparent MoS 2 Field-Effect Transistors on Hexagonal Boron Nitride-Graphene Heterostructures. *ACS Nano* **2013**, *7*, 7931–7936.

(186) Bae, S.; Kim, H.; Lee, Y.; Xu, X.; Park, J.-S.; Zheng, Y.; Balakrishnan, J.; Lei, T.; Kim, H. R.; Song, Y. Il; Kim, Y.-J.; Kim, K. S.; Ozyilmaz, B.; Ahn, J.-H.; Hong, B. H.; Iijima, S. Roll-to-Roll Production of 30-Inch Graphene Films for Transparent Electrodes. *Nat. Nanotechnol.* **2010**, *5*, 574–578.

(187) Lin, Y.; Dimitrakopoulos, C.; Jenkins, K. a; Farmer, D. B.; Chiu, H.-Y.; Grill, A.; Avouris, P. 100-GHz Transistors from Wafer-Scale Epitaxial Graphene. *Science.* **2010**, *327*, 662–662.

(188) Wu, Y.; Jenkins, K. A.; Valdes-Garcia, A.; Farmer, D. B.; Zhu, Y.; Bol, A. A.; Dimitrakopoulos, C.; Zhu, W.; Xia, F.; Avouris, P.; Lin, Y. M. State-of-the-Art Graphene High-Frequency Electronics. *Nano Lett.* **2012**, *12*, 3062–3067.

(189) Castro, E.; Novoselov, K.; Morozov, S.; Peres, N.; dos Santos, J.; Nilsson, J.; Guinea, F.; Geim, a.; Neto, a. Biased Bilayer Graphene: Semiconductor

with a Gap Tunable by the Electric Field Effect. *Phys. Rev. Lett.* **2007**, *99*, 216802.

(190) Wang, H.; Wang, X.; Xia, F.; Wang, L.; Jiang, H.; Xia, Q.; Chin, M. L.; Dubey, M.; Han, S. J. Black Phosphorus Radio-Frequency Transistors. *Nano Lett.* **2014**, *14*, 6424–6429.

(191) Radisavljevic, B.; Whitwick, M. B.; Kis, A. Integrated Circuits and Logic Operations Based on Single-Layer MoS2. *ACS Nano* **2011**, *5*, 9934–9938.

(192) Li, L.; Engel, M.; Farmer, D. B.; Han, S.-J.; Wong, H.-S. P. High Performance P-Type Black Phosphorus Transistor with Scandium Contact. *ACS Nano* **2016**, acsnano.6b01008.

(193) Mueller, T.; Xia, F.; Avouris, P. Graphene Photodetectors for High-Speed Optical Communications. *Nat. Photonics* **2010**, *4*, 297–301.

(194) Xia, F.; Mueller, T.; Lin, Y.-M.; Valdes-Garcia, A.; Avouris, P. Ultrafast Graphene Photodetector. *Nat. Nanotechnol.* **2009**, *4*, 839–843.

(195) Bernardi, M.; Palummo, M.; Grossman, J. C. Extraordinary Sunlight Absorption and One Nanometer Thick Photovoltaics Using Two-Dimensional Monolayer Materials. *Nano Lett.* **2013**, *13*, 3664–3670.

(196) Yin, Z.; Li, H.; Li, H.; Jiang, L.; Shi, Y.; Sun, Y.; Lu, G.; Zhang, Q.; Chen, X.; Zhang, H. Single-Layer MoS2 Phototransistors. *ACS Nano* **2012**, *6*, 74–80.

(197) Wu, C. C.; Jariwala, D.; Sangwan, V. K.; Marks, T. J.; Hersam, M. C.; Lauhon, L. J. Elucidating the Photoresponse of Ultrathin MoS2 Field-Effect Transistors by Scanning Photocurrent Microscopy. *J. Phys. Chem. Lett.* **2013**, *4*, 2508–

2513.

(198) Pospischil, A.; Furchi, M. M.; Mueller, T. Solar-Energy Conversion and Light Emission in an Atomic Monolayer P-N Diode. *Nat. Nanotechnol.* **2014**, *9*, 257–261.

(199) Tsai, D. S.; Liu, K. K.; Lien, D. H.; Tsai, M. L.; Kang, C. F.; Lin, C. A.; Li, L. J.; He, J. H. Few-Layer MoS2 with High Broadband Photogain and Fast Optical Switching for Use in Harsh Environments. *ACS Nano* **2013**, *7*, 3905–3911.

(200) Choi, W.; Cho, M. Y.; Konar, A.; Lee, J. H.; Cha, G. B.; Hong, S. C.; Kim, S.; Kim, J.; Jena, D.; Joo, J.; Kim, S. High-Detectivity Multilayer MoS2 Phototransistors with Spectral Response from Ultraviolet to Infrared. *Adv. Mater.* **2012**, *24*, 5832–5836.

(201) Buscema, M.; Groenendijk, D. J.; Blanter, S. I.; Steele, G. A.; Van Der Zant, H. S. J.; Castellanos-Gomez, A. Fast and Broadband Photoresponse of Few-Layer Black Phosphorus Field-Effect Transistors. *Nano Lett.* **2014**, *14*, 3347–3352.

(202) Hu, P.; Wen, Z.; Wang, L.; Tan, P.; Xiao, K. Synthesis of Few-Layer GaSe Nanosheets for High Performance Photodetectors. *ACS Nano* **2012**, *6*, 5988–5994.

(203) Koppens, F. H. L.; Mueller, T.; Avouris, P.; Ferrari, A. C.; Vitiello, M. S.; Polini, M. Photodetectors Based on Graphene, Other Two-Dimensional Materials and Hybrid Systems. *Nat. Nanotechnol.* **2014**, *9*, 780–793.

(204) Tan, J. Y.; Avsar, A.; Balakrishnan, J.; Koon, G. K. W.; Taychatanapat, T.;

O'Farrell, E. C. T.; Watanabe, K.; Taniguchi, T.; Eda, G.; Castro Neto, A. H.; Özyilmaz, B. Electronic Transport in Graphene-Based Heterostructures. *Appl. Phys. Lett.* **2014**, *104*, 1–5.

(205) Wang, Z.; Ki, D.-K.; Chen, H.; Berger, H.; MacDonald, A. H.; Morpurgo, A. F. Strong Interface-Induced Spin-Orbit Interaction in Graphene on WS2. *Nat. Commun.* **2015**, *6*, 8339.

(206) Konstantatos, G.; Badioli, M.; Gaudreau, L.; Osmond, J.; Bernechea, M.; de Arquer, F. P. G.; Gatti, F.; Koppens, F. H. L. Hybrid Graphene–quantum Dot Phototransistors with Ultrahigh Gain. *Nat. Nanotechnol.* **2012**, *7*, 363–368.

(207) Zhang, W.; Huang, J. K.; Chen, C. H.; Chang, Y. H.; Cheng, Y. J.; Li, L. J. High-Gain Phototransistors Based on a CVD MoS2 Monolayer. *Adv. Mater.* **2013**, *25*, 3456–3461.

(208) Perea-López, N.; Elías, A. L.; Berkdemir, A.; Castro-Beltran, A.; Gutiérrez, H. R.; Feng, S.; Lv, R.; Hayashi, T.; López-Urías, F.; Ghosh, S.; Muchharla, B.; Talapatra, S.; Terrones, H.; Terrones, M. Photosensor Device Based on Few-Layered WS2 Films. *Adv. Funct. Mater.* **2013**, *23*, 5511–5517.

(209) Fan, Y.; Zhou, Y.; Wang, X.; Tan, H.; Rong, Y.; Warner, J. H. Photoinduced Schottky Barrier Lowering in 2D Monolayer WS 2 Photodetectors. *Adv. Opt. Mater.* **2016**.

(210) Kufer, D.; Konstantatos, G. Highly Sensitive, Encapsulated MoS2 Photodetector with Gate Controllable Gain and Speed. *Nano Lett.* **2015**, *15*, 7307–7313.

(211) Lan, C.; Li, C.; Yin, Y.; Liu, Y. Large-Area Synthesis of Monolayer WS2 and Its Ambient-Sensitive Photo-Detecting Performance. *Nanoscale* **2015**, *7*, 5974–5980.

(212) Huo, N.; Yang, S.; Wei, Z.; Li, S.-S.; Xia, J.-B.; Li, J. Photoresponsive and Gas Sensing Field-Effect Transistors Based on Multilayer WS2 Nanoflakes. *Sci. Rep.* **2014**, *4*, 5209.

(213) Yu, W. J.; Liu, Y.; Zhou, H.; Yin, A.; Li, Z.; Huang, Y.; Duan, X. Highly Efficient Gate-Tunable Photocurrent Generation in Vertical Heterostructures of Layered Materials. *Nat. Nanotechnol.* **2013**, *8*, 952–958.

(214) Lei, S.; Wen, F.; Ge, L.; Najmaei, S.; George, A.; Gong, Y.; Gao, W.; Jin, Z.; Li, B.; Lou, J.; Kono, J.; Vajtai, R.; Ajayan, P.; Halas, N. J. An Atomically Layered InSe Avalanche Photodetector. *Nano Lett.* **2015**, *15*, 3048–3055.

(215) Gabor, N. M.; Song, J. C. W.; Ma, Q.; Nair, N. L.; Taychatanapat, T.; Watanabe, K.; Taniguchi, T.; Levitov, L. S.; Jarillo-Herrero, P. Hot Carrier-Assisted Intrinsic Photoresponse in Graphene. *Science.* **2011**, *334*, 648–652.

(216) Ratha, S.; Simbeck, A. J.; Late, D. J.; Nayak, S. K.; Rout, C. S. Negative Infrared Photocurrent Response in Layered WS2/reduced Graphene Oxide Hybrids. *Appl. Phys. Lett.* **2014**, *105*, 2012–2017.

(217) Nakanishi, H.; Bishop, K. J. M.; Kowalczyk, B.; Nitzan, A.; Weiss, E. A.; Tretiakov, K. V; Apodaca, M. M.; Klajn, R.; Stoddart, J. F.; Grzybowski, B. A. Photoconductance and Inverse Photoconductance in Films of Functionalized Metal Nanoparticles. *Nature* **2009**, *460*, 371–375.

(218) Echtermeyer, T. J.; Britnell, L.; Jasnos, P. K.; Lombardo, a; Gorbachev, R. V; Grigorenko, a N.; Geim, a K.; Ferrari, a C.; Novoselov, K. S. Strong Plasmonic Enhancement of Photovoltage in Graphene. *Nat. Commun.* **2011**, *2*, 458.

(219) Liu, Y.; Cheng, R.; Liao, L.; Zhou, H.; Bai, J.; Liu, G.; Liu, L.; Huang, Y.; Duan, X. Plasmon Resonance Enhanced Multicolour Photodetection by Graphene. *Nat. Commun.* **2011**, *2*, 579.

(220) Furchi, M.; Urich, A.; Pospischil, A.; Lilley, G.; Unterrainer, K.; Detz, H.; Klang, P.; Andrews, A. M.; Schrenk, W.; Strasser, G.; Mueller, T. Microcavity-Integrated Graphene Photodetector. *Nano Lett.* **2012**, *12*, 2773–2777.

(221) Gan, X.; Shiue, R.-J.; Gao, Y.; Meric, I.; Heinz, T. F.; Shepard, K.; Hone, J.; Assefa, S.; Englund, D. Chip-Integrated Ultrafast Graphene Photodetector with High Responsivity. *Nat. Photonics* **2013**, *7*, 883–887.

3
Methodology

Contents

3.1 Introduction 94
3.2 Materials Production 96
3.2.1 CVD growth and Transfer of graphene 96
3.2.2 CVD growth and transfer of WS_2 100
3.3 Device Fabrication 102
3.3.1 Optical Lithography 102
3.3.2 Electron-Beam Lithography 104
3.3.3 Metallization and Lift-off 106
3.3.4 Plasma Etching 108
3.4 Characterization 109
3.4.1 Optical Microscopy 109
3.4.2 Scanning Electron Microscopy 110
3.4.3 Transmission Electron Microscopy 112
3.4.4 Raman and Photoluminescence Spectroscopy 115
3.4.5 Electronic measurement 119
Reference 120

3.1 Introduction

Many special expertise and techniques are used throughout the thesis from the materials production to the characterization and to the device fabrication and measurement. This chapter aims to give a description on the major techniques and facilities used in this thesis. A brief review on the mechanism and history of each

technique will be presented on the beginning of each section. However, The emphasis will be on the application of these techniques or facilities in this thesis.

The second section of this chapter (i.e. section 3.2) covers the materials acquisition methods in this thesis. The detailed CVD growth and transfer process of graphene will be described. Only the optimized growth procedure is provided, but the influence of different parameter on graphene quality is discussed chapter 4. Following this, the growth and transfer of WS_2 domains will also be briefly discussed. It is noted that the growth of WS_2 is not within the major scope of this thesis. However, several references on that will be presented.

Section 3.3 is devoted to the methods and facilities used in device fabrication. Two lithography methods, namely photo lithography and electron beam lithography (EBL), are described and discussed in the first part of this section. Following these lithography methods, the metallization and lift-off processes are described. These processes are used to fabricate metal electrodes on 2D electronic and optoelectronic devices. Section 3.3 will be finished by the description on plasma etching that is used to pattern 2D materials used in this thesis.

The last section of this chapter (i.e. section 3.4) is a description of the characterization method used in this thesis. Section 3.4 of this chapter starts with a discussion the application of optical microscopy and scanning electron microscopy (SEM) as the

microscopic characterization method in 2D materials. Transitional electron microscopy (TEM) will be discussed right after optical microscope and SEM. The TEM techniques are used to characterize the 2D materials in atomic resolution and of vital importance for studies in chapter 6 of this thesis. Following the microscopic methods, spectroscopic method like Raman and photoluminescence will be described. Finally, details on DC measurements methods of 2D materials will be described.

3.2 Materials Production

3.2.1 CVD growth and Transfer of graphene

CVD growth of graphene is carried out in tube furnace. Digital gas flow controller is used to control the CVD system. 99.999% copper from Alpha Aesar is used in the growth of graphene. To wet and flatten the melted copper, tungsten foil (99.95% Alpha Aesar) is used as a substrate. Both the W and Cu foils are cut into 1cm by 1cm pieces prior to the reaction. They are sonicated in acetone followed by IPA for 5 minutes each to clean the surface. After the cleaning step, the metal pieces are blown dry by compressed air. The copper pieces are then placed onto the W piece, which is loaded onto an Al_2O_3 ceramic reaction boat. The boat is then loaded into the furnace.

After samples loaded into the furnace, the furnace is flushed with 200sccm Ar (99.998%), 100sccm H_2 (mixture of 25%H_2, 75%Ar) and 100sccm CH_4 (mixture of 1%CH4, 99%Ar), while increasing the temperature form room temperature to 600℃. Hereafter, 'CH_4' is used to refer the mixture gas if not specially noted so as the H_2 gas.

The sample is left outside of the heating zone of furnace in this stage to prevent unexpected reaction. The flushing aims to empty leaked-in air refill the gas pipe with fresh precursor gas. After that, CH_4 is turned off, but the flow rate of Ar and H_2 keeps at 200sccm and 100sccm respectively. The temperature of furnace is further increased to $1000°C$ after turning off the CH_4 gas. The temperature increasing speed is set to $30°C/min$, but it generally takes about 20 to 30 minutes to reach the set temperature and stabilized. Once the furnace reaches $1000°C$, the sample is loaded into the heating zone by sliding the furnace to the marked position that is calibrated to achieve an optimum temperature stability. The temperature of furnace is further increased to $1060°C$ and kept at such temperature for 30min to anneal the sample. The gas is tuned to 200sccm Ar and 80 sccm of H_2. Following the annealing, the temperature is increased to $1090°C$ to melt the copper. The copper is further annealed at this temperature for 30 minutes to enable some particles with high melting point agglomerate into dross and flow to the interface between copper and tungsten. After that, 10sccm of CH_4 is introduced together with the 200sccm Ar and 80sccm of H_2 gas to start the reaction. The reaction stands for 1.5h to grow a relative continuous film on the copper surface. After that, the temperature is lowered down to $1060°C$ again to allow another 30 minutes of growth. Some cracks forms during the cooling down process especially when copper solidified and thus this another 30 minutes growth is aimed to heal the tears in graphene film. After that, furnace is turned off and moved so as to allow a fast cooling down of the sample. This growth method is proved to give uniform monolayer graphene by ambient pressure CVD as demonstrated in chapter 4.

After the sample cooling down to room temperature, the gas is turned off to take samples out of the furnace. Immediately after sample taken out of the furnace, a PMMA protection layer is spin-coated onto the sample to prevent any degradation of graphene in the humid British air. 8% PPMA solution in anisole with molecular weight of 495k from Micro Chem is spun on the surface of graphene for this purpose. The PMMA is dynamically dispersed at 1000rpm for 15s and then spread at 4500rpm for 1 minutes. After that, the sample with PMMA is baked 180C for 1 minute on a hot plate to evaporated the solvent.

Transferring graphene onto desired substrate starts after the building of protection layer on graphene by wet chemical etching of catalyst. Due to the chemical inertia of tungsten, an electrochemical etching method is developed to etching tungsten substrate before the etching of copper so as to warrantee a fast and clean transfer process. The sample is electrically connect to the anode (positive side) of a power source, with a piece of copper connect to the cathode (negative side) as the counter electrode. NaOH (80ml, 1.5M) solution is used as electrolyte solution. The NaOH is 97% in purity and purchased from Sigma Aldrich. The sample is then dipped into the electrolyte solution while keeping the tungsten side facing the copper electrode. Current is then forced by the power station with a double threshold of 2.5V and 0.6A, In this way, the power station outputs the largest power given that the current is smaller than 0.6A and the voltage is smaller than 2.5V. This parameter is set to

minimize the O_2 bubbles generated at the anode which occasionally peals PMMA film off from the surface of copper and oxidize graphene. The electrochemical etching is carried out in a water bath at 45℃. The reaction at this experimental set-up is found to totally etch the $1cm \times 1cm$ tungsten substrate within 20 minutes. After the etching of tungsten substrate, the copper catalyst is etched by conventional chemical etching method. In this method, the sample is floated on the surface of ammonium persulfate solution with copper facing the copper etchant, which is ammonium persulfate solution. The $(NH_4)_2S_2O_8$ (98%, Sigma Aldrich) solution is 0.2M. Samples is generally left over-night on the etchant so as to thoroughly dissolve the copper. The etching time can be cut down to about 4 hours by placing the etchant in 45℃ water bath. Comparisons of this transfer process versus other methods are elaborated in chapter 4.

When metal catalyst is totally etched, the PMMA-graphene film is scoped by a glass slide and rinsed in DI water for more than twice and at least 30 minutes for each time. After the rinsing, the film is stamped onto the desired substrate, which is generally a 300nm SiO_2/Si chip. An overnight drying in ambient environment before PMMA removal is necessary to provide good attachment between graphene and chip. After the drying process, the chip covered by graphene-PMMA film is baked at 150℃ for 15min. The baking process softens the PMMA and thus leads to a better contact between graphene and silicon chip. A longer baking and higher temperature is found to be helpful to keep the integrity of graphene, but will also increase the amount of

PMMA residual after its removal. After the baking process, the chip is merged in acetone to dissolve the PMMA on graphene. The PMMA removal is done in a water bath at $45°C$ for 2.5 hours. After the removal of PMMA, the chip is rinsed in fresh acetone then IPA before blown dry by compressed air. The graphene should by then attach on the surface and ready to use. Comparing with acetone, NMP or acetic acid is the stronger remover for PMMA. However, they are found to exfoliate the transferred graphene off from the silicon chip and thus not used in most studies.

3.2.2 CVD growth and transfer of WS_2

Most of the CVD WS_2 used in this thesis is grown in collaboration with other members in our group. In this way, a detailed account of the growth procedure should not be within the scope of this thesis, and only a brief description on the growth will be presented here. However, a detailed record of WS_2 transfer will still be given, which is partly developed from my own experiments. More details on the growth could refer to previous works of our group.[1]

WS_2 is synthesized with a two furnace system to control the temperature of S and WO_3 separately. A $2cm \times 2cm$ silicon chip with 300nm SiO_2 on top was used as the growth substrate. The substrate is cleaned then loaded into the reaction furnace together with precursors. 300 mg sulfur powder (≥99.5%, Sigma-Aldrich) and 200mg WO_3 is used for synthesis. The position and distance between precursors and substrate are carefully controlled so as to grow monolayer WS_2. Before CVD growth, the

system is flushed with 500 sccm Argon for at least 30min to remove the air inside. WO_3 is heated up to 1170 ℃ and S to 180 ℃ for the reaction. The reaction lasts for 3 min with a carrier gas (Ar) flowing at 250 sccm. When finishing the reaction, we decrease the temperature of WO_3 quickly, while heating S to 450 ℃ to deplete the unreacted S.

A layer of PMMA is spun on the as grown WS_2 domains as protection layer immediately after the CVD growth. WS_2 domains are found to degrade in ambient condition especially when exposed to humid air or UV light. The PMMA is 8% anisole solution with molecular weight of 495k similar as the one used in graphene transfer. The spin recipe is also same to the one used for graphene transfer, which is 4500rpm for 1 minute. The chip is then baked at 180℃ for 1 minute to evaporate the anisole solvent and solidify the PMMA film. WS_2 is generally grown on a 2cm by 2cm silicon chip, which will be cut into 4 pieces of 1cm by 1cm small chips.

The WS_2 is transferred by a wet chemical assisted transfer method. The edge of the chip with PMMA covered WS_2 is milled by diamond file before the etching. This is aimed to get rid of PMMA edge bead covering the chip edge, which significantly slows down the etching speed. After that, 80mL, 1.5M NaOH solution (97% NaOH, Sigma Aldrich) is used as the etchant of silicon oxide. The solution is then heated in a 45℃ water bath. The chip is then carefully placed and floated on the surface of etchant. The etching process generally takes about 1 hour.

After the etching process, the PMMA-WS_2 film is scoped onto DI water by glass slide. The film is rinsed at least twice for 30 minutes each time before transferring onto the final substrate. After that, the sample is dried overnight to enable a good attachment between the WS_2 domains and the chip. Different from graphene, the baking process is found to be not necessary for the transfer of WS_2, though most transferred WS_2 are still baked. This may due to the stronger interaction between TMDC materials and silicon chip. Acetone is commonly used as the remover of the PMMA at 45℃. However, merging the chip in NMP at 80℃ for 2 hours is also found to effectively remove PMMA. Different from graphene, the NMP remover does not peal transferred WS_2 domains off from the chip easily. After the removal of PMMA, the chip is ready for device fabrication.

3.3 Device Fabrication

3.3.1 Optical Lithography

Optical lithography is one of the most widely used lithography method in industry, which patterns the photo resist by ultra-violet (UV) exposure. Chemical reactions in the UV exposed region of the UV-sensitive would change the solubility of the photo resist in certain solution, which is referred as the “developer”. Two types of photo resist, i.e. “positive” and “negative” resist, are commonly used. In the case of positive resist, photoresist molecules in the exposed region will reconstruct and become soluble in the developer. On the contrary, the negative resist will crosslink when

exposed. The unexposed region of the negative resist will however be dissolved during the developing step. By control the shape and size of the region exposed to UV light, micro-patterns can be made with the photo resist. Since light is used to expose the pattern, a theoretical resolution is set by the wavelength of exposure light.

Both positive and negative resist is used in the device fabrication process of this thesis. MicroPosit S1813 G2 photoresist (hereafter "S1813") is used as the positive resist and the MicroChem MaN 1420 photoresist (hereafter "MaN1420") is used as the negative resist. The lithography starts with spin-coating the photo resist on the sample surface. The spinning coating recipe is 4500rpm for 1 minute. This will result a film thickness of 1.2 μm for S1813 positive resist and 2μm for MaN1420 negative resist. After the spin coating, the sample is baked on a hot plate. The positive resist is baked at 115℃ and the negative resist is baked at 90℃. The baking time for both resist is 1min.

After that, the sample covered by photo resist is aligned with a photo mask using the Karl Suss MJB3 mask aligner. The photo mask is from different companies but all of the use Cr reflection layer. The patterning of the mask determines the structure of device. After aligning the chip with mask, they are pressed together to have a good contact. This mode of lithography is often referred as the "contact mode". In our experiment, all devices fabricated by optical lithography are exposed in the contact mode. UV light is then illuminated onto the mask so as to the expose unmasked part

of the sample for certain amount of time. After that, the sample is taken out of the mask aligner and developed in the developer of the photoresist to finish the lithography process. It should be noted that the MaN series negative resist will crosslink after exposure, which results them to be hard to totally get rid of.

3.3.2 Electron-Beam Lithography

Electron beam lithography (EBL) is the state-of-art lithography methods in nano-device fabrication, which enables high accurate and flexible device fabrication. Different from optical lithography, wavelength of incident beam is not the major limitation factor of the resolution of this lithography method. Instead of using photon, accelerated electron is used to expose the resist. The wavelength of electrons is down to picometers, which is smaller than the size of an atom. The actually resolution of the EBL method is limited by the abberations induced by electromagnetic lenses as well as electron beam source. Another factor that lowers the EBL resolution is the beam spread. Random Scattering of incident electron beam will result a larger exposed region than the real beam size. In this way, the lowest exposure dose and thinnest resist should be found to have the optimum results. Despite of all these side effects mentioned, the JBX-5500 EBL facility used in this study still promise a resolution better than 4nm. In additional to the good resolution, EBL system enables a very flexible fabrication procedure. Any pattern can be written within EBL system without the use of a pre-patterned mask.

The electron optical circuit of an EBL system is like the one in scanning electron microscope (SEM). Electrons are focused and scanned over the surface of the sample so as to expose the electron resist. Two electron beam acceleration voltages, 25kV and 50kV, can be selected. For all experiments in this thesis, 50kV electron beam is used. The writing field without moving the sample holder (cassette) can be set but there is a maximum writing field determined by the objective lens used in exposure.

Both positive and negative resist is used in studies in this thesis. PMMA is used as positive electron resist. The incident electron beam cut the polymer chain of PMMA in the exposed region. PMMA with shorter chain tend to dissolve quicker in the developer. On the other hand, MaN2403 is used as negative electron resist. The incident electron beam crosslinks the exposed resist. The unexposed part of the resist can be washed away by the developer after the exposure.

A layer of electron resist is spin-coated on the surface e of materials before the lithography. Positive resist (PMMA) or negative resist (MaN2403) is used depending on the purpose. Double layer PMMA is generally used for the fabrication of thick metal figures like bond pad and large electrodes. For the 1^{st} layer of PMMA, 4% anisole solution of 495k PMMA is spun on the surface of chip at 4500rpm for 45s. This will results a 150nm film on the chip surface. After the spin coating, the chip is baked at 180°C for 1.5min to evaporate the anisole solvent. Another spin coating is followed immediately after the baking. The 2^{nd} layer of PMMA is made of 4% anisole

solution of 950k PMMA, which is spun at the same spin-coating recipe. Another baking at $180°C$ for 1.5min is done after the 2nd coating. After the 2nd baking, the sample is ready to load into the EBL facility. As for patterning graphene ribbon, negative resist is used to save the exposure time. The negative resisted is spin-coated on chip at the spin speed of 3000rpm for 30s, which results a film thickness of 300nm. The baking temperature for negative resist is $90°C$ and the baking time is 1min.

The sample is now ready to load into the chamber and exposure. The chip is fixed onto a chip holder (cassette), and then loaded into the exchange chamber. After the chamber pressure reaches the threshold, air-lock of the exposure chamber will be opened and the sample is loaded into the exposure chamber. The exposure is controlled by a remote operation system on PC. The exposure current can be adjusted so as to reach a good resolution as well as short writing time. Typically, figures larger than $5\mu m$ is written with 10nA and figures from 100nm to several micrometre is written by 1nA current to have the best result. Even finer control can be achieved by using an extra lens for fine beam control. The positive resist (PMMA) is exposed at a dose of $600\mu C/cm^2$ and the negative resist is exposed at a dose of $200\mu C/cm^2$. After the exposure process, positive resist is developed in a mixture of 1:3 IPA:MIBK solution for 1 min at $25°C$. As for the negative resist, the sample is developed in MaD525 at $25°C$ for 2.5min.

3.3.3 Metallization and Lift-off

The metallization and lift-off procedure is the conventional way to fabricate metal electrodes and bond pads. Metal thin film is evaporated onto the sample covered with patterned resist. The evaporated metal only contacts the sample in regions without resist. After that, the resist is removed so as to "lift-off" the metal on resist and leave only metal contact with the sample on chip.

Metallization

The metallization is carried out using the Edward 360 thermal evaporator in cleanroom. The sample is attached onto the sample holder by Kapton tape, which keeps good stability under high vacuum and high temperature. The evaporation generally start at when the chamber pressure dropped to $2 \times 10^{-6}\mathrm{mbar}$. Joule heating is used to increase the temperature of metal target and produce metal evaporation. For the fabrication of bond pad, a 10nm Cr adhesion layer under a 90nm Au layer is often used.

Lift-off

The lift off process is carried immediately after the metallization of sample by leaving it in the resist remover. Acetone is the most commonly used remover for both positive and negative resist. Other removers like NMP is also used under certain occasion as will mentioned in the latter chapters when used. A sonication process is helpful for a quick and clean lift-off process whenever is possible.

3.3.4 Plasma Etching

Plasma etching is a prevailing technique to patterning 2D materials. The plasma state is a collection of free charged particles with equal amount of positive charge and negative charge, and thus the system is electrically neutral. In a plasm etcher, electrons are stimulated out of the gas atom by RF power to form the plasma state. The charged gas molecules also moves which is caused by the outside electromagnetic field. In this way, both mechanically milling (due to the booming of charged gas molecule on sample surface) and chemical reaction (due to the high reactivity of the stimulated gas molecules) happen at the same time during the plasm etching process.

Diener plasma etcher in our lab is used for all experiments in this thesis. For the experiment facility used in this thesis, 40kHz RF electromagnetic field is generated to produce plasma. The full power of that plasma etcher is 100W. Oxygen plasma is used to pattern 2D materials including graphene and WS_2. The flow rate of O_2 is kept at around $40L_n/h$. The chamber is pumped down then flushed with the O_2 gas for 5 minutes before the starting of plasm etching. During the plasma etching process, the base pressure keeps from $0.3mbar$ to $0.4mbar$. For the etching of graphene, the RF power is generally set to 60W, and he etching process last for 30 seconds. For the etching of WS_2, a large plasm power (90W) and longer etching period (100s) is used. It I noted that the WS_2 is found to be much harder to totally get away compared with graphene.

3.4 Characterization

3.4.1 Optical Microscopy

Optical Microscopy is one of the major and easiest microscopic methods used in the study of 2D materials. This method enables a fast and non-harmful detection of the layer number and microscopic continuity of 2D materials. Merely single layer of carbon atom in graphene is visible on the 300nm oxide layer of silicon chip.[2] Techniques that correlate the colour of graphene on SiO_2/Si substrate to layer number are soon developed.[3] With the quick discovery of new 2D materials, the optical microscopic method soon finds a large application as a general tool to determine the layer number of 2D materials.

Several types of microscope are used in studies covered by this thesis. A home-made microscope illuminated by a yellow LED is the major one used to identify the as grown WS2 domain. Mitutoyo objective lens with $40\times$ and $20\times$ magnification are used for different images. Thorlabs 1280×1024 CMOS colour sensor is used as the camera to acquire the microscopic images and display on a computer. The yellow LED is found to provide a good contrast of the WS2 domains on 300nm SiO_2/Si substrate. This microscope is mainly used for the image taking of WS_2.

Another microscope used is the eVue Pro digital imaging system that is in accompany with the Cascade MicroTech Probe Station. Different from the home-made

microscopy system, this microscope is illuminated by an in-lens light source of fast blinking red, green and blue light. RGB light periodically shines on sample surface and the contrast is recorded and synthesis together to give the final colourful image. This microscope provides a better resolution compare with the home-made microscope as mentioned. In this way, it is mainly used to distinguish the contrast difference among graphene with different layer number on 300nm SiO_2. This microscopic is also used to take optical microscopic record of the devices during electronic measurement.

3.4.2 Scanning Electron Microscopy

The Scanning electron microscope (SEM) provides rich information about the 2D materials studied in complimentary with the optical microscope. Several types of SEM are used in this thesis. This section will briefly describe the working principles of SEM as well as the common usage of the SEM in this study.

Accelerated energy electron beam (typically $10^0 - 10^2$keV) is focused onto the surface of sample surface then scanned over the surface line by line. Secondary electrons and the scatter electrons are the two major types of electrons that are stimulated by the incident electron beam. The secondary electron is generated by the knocking off of electron form the inner shell of atoms on the surface of sample material. It contains information on the materials composition. The back scatter electrons are result of elastic scattering of the incident electron beam. The intensity of

back scatter electron is sensitive to the crystal orientation of the materials and thus will provide relative crystal information. Both types of electrons are collected by the electron detector which forms the SEM image.

Hitachi S-4300 cold emission SEM is most commonly used in this study. This microscope is routinely used to check the quality of 2D materials used in this thesis including graphene and WS2. The resolution of this microscope reaches down to around 40nm. Very low acceleration voltage down to 0.5kV can be reached while maintaining a reasonable resolution. In the study in chapter 6, the observation of suspended 2D materials is necessary. Such a task is generally challenging due to the high electron transmission of 2D materials, especially when suspended. It is found that a lower acceleration voltage of the electron beam would results a high contrast of suspended 2D material. In practice, 2kV acceleration voltage and 5μA beam current is used to resolute the suspended materials to reach a balance between good space resolution and high contrast. A lower imaging current is also found to protect the 2D materials from e-beam damage during the imaging process.

Another SEM used frequently is the N-vision SEM. The in-lens detector equipped in this microscope enables a better contrast especially for fluctuated surface. This SEM also has a better space resolution compared with the Hitachi SEM. Figures down to 10nm can be clearly resolved. This microscope is used for part of the SEM study on the graphene growth on copper as is represented in chapter 4. The copper is by nature

curved after the melting and solidification, which would introduce spurs effect on SEM imaging with the conventional side-electron detector like the one in Hitachi S4300. The high resolution of this microscope also provides the observations of more details like small teas on graphene surface.

As for the SEM characterization of materials on silicon chip, 3kV acceleration voltage is generally used. This will results a negative charge of the SiO_2 surface of the silicon chip and enhance the contrast between it and graphene. Carbon tape is used to attach the sample onto a conductive holder.

3.4.3 Transmission Electron Microscopy

Transmission electron microscope is a powerful tool to unveil the structure information of 2D materials. TEM is frequent used in the study presented in the chapter 6 of this thesis. Two types of TEM, i.e. JEOL 2010 and Oxford-JEOL 2200, are used in the study. TEM images with atomic resolution are taken by Oxford-JEOL 2200 TEM, which is obtained in collaboration with Dr. Alex Robertson. The author also uses the JEOL 2010 for some routine check of the TEM devices. Most of TEM related works are reported in chapter 6. A detailed operation procedure is out of the scoped of this thesis, but only some important notes on the key parameters will be given. This section will, however, describe how we calculate the beam current density and calibrate the real magnification of TEM image, which are indispensable for studies in chapter 6 of this thesis.

Modern TEM system generally includes three systems: electron source system, electron-optical system and the imaging system. Electron beam emitted from the electron source system (i.e. “electron gun”) is altered by the electron-optical system and convert to light or electronic signal by the imaging system. Among them, the electro-optical system determines the quality and resolution of the final image. Electron beam is illuminated onto the materials and the transmitted electrons are controlled by the lenses so as to magnify the image of material. The TEM is categorized into two types, i.e. the HRTEM and conventional TEM according to the mechanisms of contrast formation. HRTEM relays more on the phase contrast while the convention TEM relays more on the amplitude contrast. The amplitude contrast is induced by the inelastic scattering between incident electron beam and materials lattice. It provide information on the thickness and (to certain extent) chemical component of the materials. On the other hand, HRTEM make use of the interference of electron when passing through the materials lattice. This is the so called “phase contrast”. The observation of phase contrast requires more on the monochromatic and parallel of electron beam when passing through the sample compared with the amplitude contrast. Details on the mechanism behind TEM deserve much more paragraphs and thus are not included in this thesis. An abundancy of reference on this topic can be found though.[4] in the case of 2D materials characterization, HRTEM is commonly used to resolve the atomic-thin materials.

In practice, there are several key issues to address. The incident electron beam is known to induce defect on the materials.[5] In this way, acceleration voltage of the TEM observation is important to balance between high resolution and low defects creation rate. 80kV acceleration is generally used for this purpose. Both image mode and diffraction mode is used to take the structure and crystal information of the materials. It is noted that long time exposure of WS_2 will results the formation of defects, which is due to the electron sputter of sulphur atom. Another issue is directly related to the acceleration voltage is the aberrations in the electromagnetic lenses in TEM. In most modern TEM, the spherical aberration is the largest limitation of actual resolution. According to the Scherzer's theorem, the spherical aberration always exist in a system of electromagnetic lenses with cylindrical symmetry.[6] Thanks to the development of the spherical aberration corrector,[7] as what is used in the Oxford-JEOL 2200 TEM, the spherical aberration is to a large extent limit to a small value.

Calibration of TEM data

The lattice parameter of WS_2 and graphene film are used to calibrate the high-mag TEM data (reported magnification >500000). The lattice constant (e.g, edge length of a unit cell) of WS_2 is taken as 3.158A,[8] [9] and the lattice constant of graphene is taken as 2.462A.[10] To avoid any local effect due to lens aberrations or other unexpected effect, the calibration is carried out in reciprocal space by taking the FFT of the image with clearly resolved lattice structure. Both reference crystals, e.g. graphene and WS_2,

show similar hexagon symmetry in the FFT of their lattice resolved TEM images. We chose the longest feasible pairs of spots to lower the measurement error. The average distance between the spots within one pair is taken as the reference. The calibration is finished by compare the theoretical value of such distance with the measured distance in pixel.

Measurement of beam current

The beam current density is calculated by dividing the count number in dm3 file with a pre-calibrated converting number (15.23 counts per electron in our case). We calculate the total e-beam current on the device by summing up the e-beam current per pixel. The link between count number in dm3 file and real current is measured by a Faraday cup that equipped under the sample holder. A pico-Ampere meter is used to measure the beam current from the Faraday cup.

3.4.4 Raman and Photoluminescence Spectroscopy

Raman

Raman spectrum of material reveals the lattice information of the material by peaks in Raman shift. Inelastic scattering between incident photon and lattice would occasionally result a blue (or red) shift of the photon if one or several phonons are absorbed (or emitted). Peaks in Raman shift are thus attributed to different phonon modes, which are fundamentally determined by the lattice symmetry and bond strength. In practice, the position and relative intensity between each Raman peak also

depends on the energy of incident photon.[11] Moreover, multi-phonon absorption (emission) is commonly found, which add certain uncertainty to the understanding of Raman spectrum. Thorough discussions on these phenomena are out of the scope of this thesis, but should be referred to relevant references.[11] [12] In this thesis, the Raman spectrum of graphene and WS2 domains are used to identify the layer number and quality of them. The characterization of graphene by Raman spectrum has been reported by Ferrari et al in 2007.[13] Raman spectrum of 2D TMDC are also been identified soon after the their discovery.[14] [15]

The JY Horiba LabRAM ARAMIS imaging confocal Raman Microscope is used to acquire the Raman spectrum of 2D materials in this thesis. 532nm green laser generated from a frequency doubled Nd:YAG laser source is used to excite the Raman scattering. $50\times$ lens is used for Raman measurement without special specification hereafter in this thesis. The laser is linearly polarized, and the spot diameter is about 6 micrometres. The full power of the laser is 12.5mW in total, but different filter could be used to avoid damage to the sample or signal saturation. Two types of grating, $1800mm^{-1}$ and $600mm^{-1}$, are equipped in this Raman spectrometer, which enables different resolution in the acquired spectrum. The system is calibrated with the Raman shift of silicon at 520.1cm^{-1}.

Raman spectrum of graphene and WS_2 domains in this thesis is taken with the same Raman Spectrometer aforementioned, but with different set-ups. Full laser power is

used to measure Raman spectrum of graphene. The spectrum is averaged between 2 cycles of measurement with 2s acquisition time and 1s dwell time. This set-up is found to have a good contrast in spectrum but not damage the sample or induce thermal effect. Under the experimental set-up aforementioned, D ($\sim 1344 cm^{-1}$), G ($\sim 1580 cm^{-1}$), and 2D ($\sim 2680 cm^{-1}$) peaks are observed for monolayer graphene. The D peak of graphene is generally referred as the "defect peak", which reflects the spoil of periodical hexagonal lattice of graphene. The integral peak intensity of 2D peak should be larger than twice of the G peak in the case of monolayer graphene. It should be noted, however, the Raman spectral of turbostratic multilayer graphene is very similar to monolayer graphene due to poor interlayer scattering of phonons. In this way, additional methods like AFM or SEM should also be involved to determine the actual layer number.

The Raman spectrum of WS_2 is taken at 10% laser power for 1 second and averaged 3 times. The dwell time is also 1 second. It is noted that a stronger laser or longer time exposure time would induce damages to the WS_2 domains hereby should be avoided. Many secondary peaks are stimulated by the 532nm laser used in our experiments. Nevertheless, the two major peaks, i.e.: $E_{2g}(\sim 356 cm^{-1})$, and $A_{1g}(\sim 415 cm^{-1})$, are still significant. The peak shift and integral intensity ratio between E_{2g} peak and A_{1g} peak are $58 cm^{-1}$ and larger than 3 for monolayer WS_2. Further studies on the Raman spectrum of WS_2 can be found in chapter 5 and 6 of this thesis, but detailed account of the physics under Raman spectrum should be referred to literatures.

Photoluminescence

Photoluminescence (PL) is a powerful tool for the characterization of materials. PL spectroscopy measures the light emission of the material after the absorption of photons with certain energy. Photoluminescence of direct-band-gap material is generally much stronger than indirect-band-gap materials due to the higher light absorption and recombination rate. When in their 2D form, all materials belonging to the TMDC family are direct-band-gap, which is in favour of PL characterization. It should be noted, however, the PL peaks of 2D material are sensitive to many factors like temperature[16], light intensity[17], dielectric environment[18],and gate[19].

The same spectrometer (i.e. JY Horiba LabRAM ARAMIS imaging confocal Raman Microscope) is used to take PL signal as when taking Raman signal. However, the PL is taken at different parameter settings. The range of PL for WS_2 is general set to from 1.8eV to 2.1eV, which covers the major PL peak in WS_2. 10% filter is applied when taking the PL spectrum of WS_2 to avoid sample damage. The acquisition time is generally set to 1 second to avoid signal saturation, but ready to adjust to optimum of the best spectrum contrast. With the setting aforementioned, the PL spectrum of monolayer WS_2 generally consists of 2 peaks: exciton (2.02eV) and trion (1.97eV). It would be possible to extract the electron concentration of WS_2 by the ratio between integral intensity of trion and exciton as mentioned in chapter 5 of this thesis. Experimental measurement of PL of CVD WS_2 can be found in chapter 5 ad 6 of this

thesis.

3.4.5 Electronic measurement

Electronic measurements in chapter 4 and chapter 5 are carried out on probe station in ambient environment while the measurements in chapter 6 are done in vacuum (inside TEM). Some of the measurements are carried out on Cascade Probe station so as to realize automatic movement of the sample. Other measurements are finished with our home-made probe station.

Two kinds of semiconductor measurement units (SMUs), Keithley 2400 and HP4142A, are used in this thesis. During the measurement, both the source-drain current and gate current leakage are recorded by the SMU. Remote control software is used to control the output and measurement of the SMU automatically. The software was coded by former group member, but is maintained an updated by the author of this thesis during his DPhil study. All “sweep” measurements are actually realized by the continuous “spot” measurement. When use the Keithley 2400 as the SMU, the number of power line cycle (NPLC) is generally set to 0.1 to enable a quick sweep, but will set to 1 when a precise measurement is required. It should be noted that the Keithley 2400 SMU general guarantee an accuracy of current measurement down to 0.1nA, but that is accuracy of measurement is directly linked to the NPLC. The larger NPLC will results a better precis but slower measurement.

Field effect mobility is the major figure of merit extracted by the electronic

measurement. In practice, current saturation is rarely reached in the output measurement of our materials. In this way, all field effect measurements are done in the linear region of material. The following equation is used to extract the field effect mobility:

$$\mu = \frac{dI}{dV_g}\frac{L}{W}\frac{1}{V_{sd}C_i}$$

Where I is the current, V_{sd} is the source-drain bias, V_g is the gate voltage, L and W and the channel length and width respectively, and C_i is the relative capacitance. 300nm SiO_2 are the gate dielectric layer used in our experiments without special claim, the relative capacitance of which is $11.5nF/cm^2$. More detailed account on this measurement, especially regarding on the extraction of field effect mobility, is reported in chapter 4 of this thesis.

Reference

(1) Rong, Y.; Fan, Y.; Leen Koh, A.; Robertson, A. W.; He, K.; Wang, S.; Tan, H.; Sinclair, R.; Warner, J. H. Controlling Sulphur Precursor Addition for Large Single Crystal Domains of WS2. *Nanoscale* **2014**, *6*, 12096–12103.

(2) Novoselov, K. S. S.; Geim, A. K. K.; Morozov, S. V. V; Jiang, D.; Zhang, Y.; Dubonos, S. V. V; Grigorieva, I. V. V; Firsov, A. A. a. Electric Field Effect in Atomically Thin Carbon Films. *Science.* **2004**, *306*, 666.

(3) Blake, P.; Hill, E. W.; Castro Neto, A. H.; Novoselov, K. S.; Jiang, D.; Yang, R.; Booth, T. J.; Geim, A. K. Making Graphene Visible. *Appl. Phys. Lett.* **2007**, *91*.

(4) Williams, D. B.; Carter, C. B. *Transmission Electron Microscopy: A Textbook for Materials Science*; 2nd ed.; Springer US: Boston, MA, 2009.

(5) Sun, L.; Banhart, F.; Warner, J. Two-Dimensional Materials under Electron Irradiation. *MRS Bull.* **2015**, *40*, 29–37.

(6) Crewe, A. V. Ideal Lenses and the Scherzer Theorem. *Ultramicroscopy* **1976**, *2*, 281–284.

(7) Rose, H.; Wan, W. Aberration Correction in Electron Microscopy. In *Proceedings of the 2005 Particle Accelerator Conference*; IEEE, 2005; pp. 44–48.

(8) Yu, Y.; Hu, S.; Su, L.; Huang, L.; Liu, Y.; Jin, Z.; Purezky, A. a; Geohegan, D. B.; Kim, K. W.; Zhang, Y.; Cao, L. Efficient Interlayer Relaxation and Transition of Excitons in Epitaxial and Non-Epitaxial MoS2/WS2 Heterostructures. *arXiv Prepr. arXiv …* **2014**, *15*, 486–491.

(9) Wildervanck, J. C.; Jellinek, F. Preparation and Crystallinity of Molybdenum and Tungsten Sulfides. *Zeitschrift für Anorg. und Allg. Chemie* **1964**, *328*, 309–318.

(10) Pozzo, M.; Alfè, D.; Lacovig, P.; Hofmann, P.; Lizzit, S.; Baraldi, A. Thermal Expansion of Supported and Freestanding Graphene: Lattice Constant versus Interatomic Distance. *Phys. Rev. Lett.* **2011**, *106*, 1–4.

(11) Malard, L. M.; Pimenta, M. A.; Dresselhaus, G.; Dresselhaus, M. S. Raman Spectroscopy in Graphene. *Phys. Rep.* **2009**, *473*, 51–87.

(12) Smith, E.; Dent, G. *Modern Raman Spectroscopy - A Practical Approach*; John

Wiley & Sons, Ltd: Chichester, UK, 2004.

(13) Ferrari, A. C.; Meyer, J. C.; Scardaci, V.; Casiraghi, C.; Lazzeri, M.; Mauri, F.; Piscanec, S.; Jiang, D.; Novoselov, K. S.; Roth, S.; Geim, A. K. Raman Spectrum of Graphene and Graphene Layers. *Phys. Rev. Lett.* **2006**, *97*, 1–4.

(14) Li, H.; Zhang, Q.; Yap, C. C. R.; Tay, B. K.; Edwin, T. H. T.; Olivier, A.; Baillargeat, D. From Bulk to Monolayer MoS 2: Evolution of Raman Scattering. *Adv. Funct. Mater.* **2012**, *22*, 1385–1390.

(15) Berkdemir, A.; Gutiérrez, H. R.; Botello-Méndez, A. R.; Perea-López, N.; Elías, A. L.; Chia, C.-I.; Wang, B.; Crespi, V. H.; López-Urías, F.; Charlier, J.-C.; Terrones, H.; Terrones, M. Identification of Individual and Few Layers of WS2 Using Raman Spectroscopy. *Sci. Rep.* **2013**, *3*, 1755.

(16) Plechinger, G.; Nagler, P.; Kraus, J.; Paradiso, N.; Strunk, C.; Schüller, C.; Korn, T. Identification of Excitons , Trions and Biexcitons in Single-Layer WS2. **2015**, *461*, 457–461.

(17) Currie, M.; Hanbicki, A. T.; Kioseoglou, G.; Jonker, B. T.; Currie, M.; Hanbicki, A. T.; Kioseoglou, G.; Jonker, B. T. Optical Control of Charged Exciton States in Tungsten Disulfide. *Appl. Phys. Lett.* **2015**, *106*.

(18) Lin, Y.; Ling, X.; Yu, L.; Huang, S.; Hsu, A. L.; Lee, Y.; Kong, J.; Dresselhaus, M. S. Dielectric Screening of Excitons and Trions in Single-Layer MoS 2. *Nano Lett.* **2014**, *14*, 5569–5576.

(19) Zhu, B.; Chen, X.; Cui, X. Exciton Binding Energy of Monolayer WS2. *Sci. Rep.* **2015**, *5*, 9218.

4

Growth and Electronic Application of CVD Graphene

Contents

4.1 Introduction 123

4.2 CVD Growth and Transfer of Graphene 124

4.2.1 Introduction 124

4.2.2 Growth of Graphene on melted copper 126

4.2.3 Transfer of Graphene by anodic etching of catalyst 132

4.2.4 Characterization of the CVD graphene 137

4.3 Influence of Substrate to Graphene FET 139

4.3.1 Introduction 139

4.3.2 Experiment and Materials characterization 140

4.3.3 Results and discussion 142

4.3.4 Conclusion 146

Reference 146

*The major content in section 4.2 of this chapter is modified from reference [1].

**EDX images in Figure 4-1 (a)-(f) are taken by Dr. Susie Speller, SEM images in Figure 4-3 (b) and (c) is taken by Dr. Kuang He.

4.1 Introduction

This chapter aims to discuss the author's work on the chemical vapour deposition growth and transfer of graphene. This work paves the way toward on-chip graphene electronics. The second section (section 4.2) of this chapter will compare different growth and transfer methods. This study provides the optimum parameters for the

growth and transfer of graphene on liquid copper. Following that, section 4.3 will provide experimental evidence on the influence of substrate to electronic properties of graphene. Hydrophobic substrate is found to be favourable for graphene electronics due to lower level of unintentional doping and trapped states from trapped water.

4.2 CVD Growth and Transfer of Graphene

4.2.1 Introduction

Graphene is expected to play versatile roles in various electronic and spintronic applications including, but not limited to, radio-frequency field effect transistors[2 3], spin valves[4 5], solar cells[6 7] and organic light emitting diodes (OLED)[8 9]. Despite of the bright vista aforementioned, the lack of saleable production method of high-quality continuous graphene film keeps graphene-based device distant away from the industrialization. “Top down” methods that obtain graphene form graphite, like mechanical exfoliation and liquid exfoliation, is not suitable for that task as have reviewed in the 2nd chapter of this thesis. As a brief reiteration, the mechanical exfoliation methods produce high quality graphene, but with very limited and uncontrollable production. In addition, the quantity of graphene produced by liquid exfoliation is large, but generally suffers from poor electronic properties. Different from the “top down” method, which generally involves the physics cleavage of graphite, “bottom up” methods of graphene production synthesis graphene through chemical raction. The “bottom up” methods mainly includes thermal annealing of silicon carbide[10] and chemical vapour deposition (CVD). Epitaxial graphene on

thermal annealed silicon carbide exhibits excellent electronic properties[11 12], but its applications are limited by the challenges in controlling the number of layers of graphene and transferring it onto conventional substrates (i.e. silicon chip). On the other hand, CVD graphene matches epitaxial graphene on silicon carbide in its electronic properties[13 14 15], whilst being able to transfer onto arbitrary substrate.

Although the record size of individual isolated graphene domains continues to increase (now in the mm scale),[16, 17] challenges still remain in producing high-quality continuous graphene sheet. Large area continuous graphene sheets generally have small domain sizes around 20 μm.[18] Moreover, multi-layer regions of graphene is found even in graphene synthesized under low pressure[19]. Impurities, surface roughness and grain boundaries of copper are suspected to be responsible for the multi-layered regions. In contrast, large area single layer graphene domains are easily synthesized when the copper catalyst is in a molten state rather than solid form.[20 21 22 23] With longer growth time, graphene domains floating on melted copper are expected to expand and coalesce to form continuous film.

In this section we study synthesis and transfer processes for continuous graphene film grown on melted copper by CVD. We find that macro-defects, e.g. cracks and holes, can be derived from tensions introduced in either the synthesis or transfer process. To address that problem, we develop a novel two-stage “regrowth” method. A tension-free electrochemical transfer method is also investigated for the efficient

transfer of centimetre-scale continuous graphene without introducing any major cracks.

4.2.2 Growth of Graphene on melted copper

Graphene is grown by ambient pressure chemical vapour deposition (AP-CVD) as reported in the methodology chapter of this thesis. Catalyst substrate, cooling rate and transfer method are found to be the key factors determining the quality of final product. Refractory metals like W or Mo are used as substrates because they are wet by the molten copper, producing flat surfaces for graphene growth. Although W and Mo share similar chemical and mechanical properties, they have different effects on the morphology of the CVD grown graphene. Hexagonal particles are found all over the substrate of the as-synthesized graphene on Mo-supported copper, as shown in Figure 4-1. Despite their similar shape with graphene domains, Raman spectroscopy showed no graphene peaks in this area, whilst energy dispersive X-ray spectroscopy (EDX) shows the particles are composed of a mixture of Mo-C-O, Figure 4-1 (c)-(f).

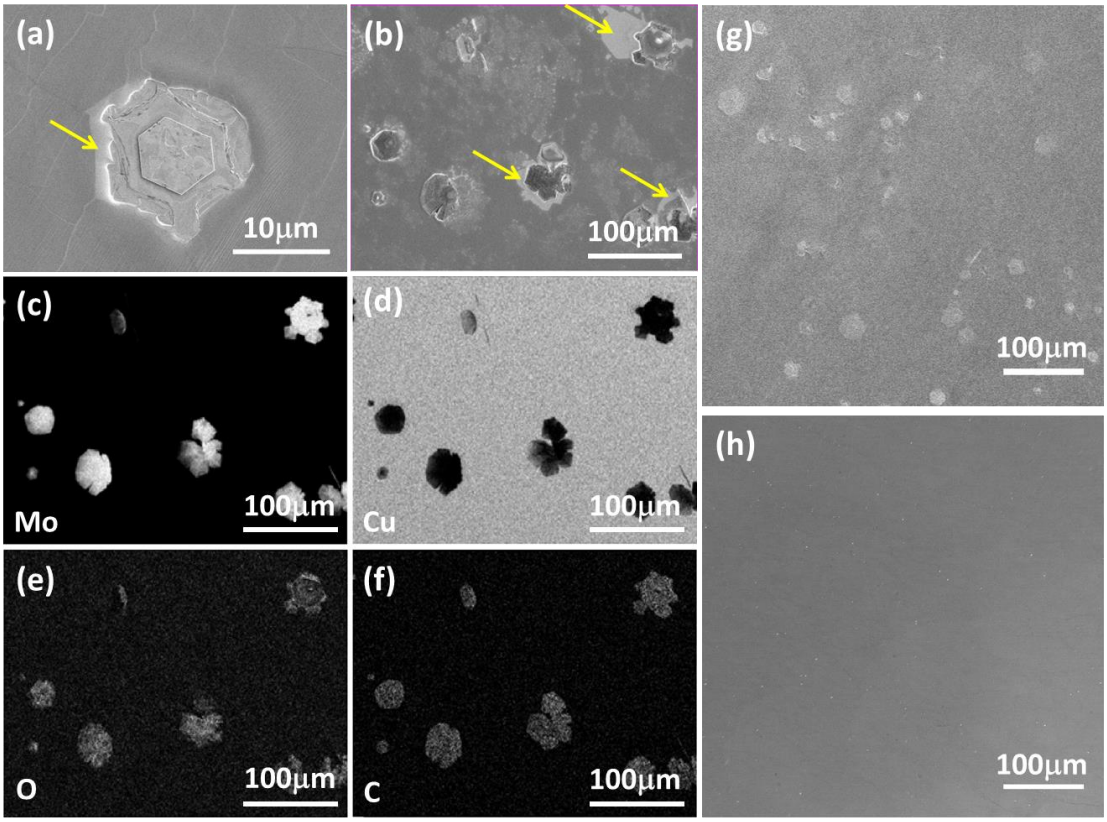


Figure 4-1 SEM and EDX images of graphene grown by CVD on copper with a Mo or W wetting substrate. (a) SEM image of graphene grown on molten Cu with a Mo wetting substrate by CVD, where a hexagonal Mo-C-O alloy is observed to disrupt the graphene in the local neighbourhood as pointed out by the arrow. (b) SEM image of a region of graphene grown by CVD on Cu:Mo used for energy dispersive X-ray spectroscopy (EDX) maps in (c)-(f). (c) Molybdenum La1 EDX map. (d) Copper Ka1 EDX map. (e) Oxygen Ka1 EDX map. (f) Carbon Ka1_2 EDX map. (g) SEM image showing large number of holes in graphene caused by Mo-C-O alloy. (h) Continuous graphene film obtained by CVD on molten Cu with a W substrate.

The density of the Mo-C-O particles increases with the amount of time the sample is exposed to CH_4, but does not increase with the amount of pre-annealing time in hydrogen (i.e before CH_4 is introduced). Therefore the Mo-C-O particles are likely to be formed by metal-catalysed carbonization. In contrast with graphene grown on Mo supported Cu, graphene grown on W supported Cu remains continuous. No secondary phase particles are found and the graphene is hole-free over the centimetre scale, as

shown in Figure 4-1 (h).

The cooling process is another key factor determining the continuity of graphene. We study two cooling processes: “fast cooling” and “regrowth cooling”. “Fast cooling” refers to a cooling process where the sample is quickly removed from the heating zone immediately after synthesis to rapidly cool to room temperature. “Regrowth cooling” refers to a cooling process where the temperature is gradually lowered down from 1090 ^{o}C to 1060 ^{o}C for the last 30 minutes of graphene growth before removing the sample out of the heating zone and cooling to room temperature.

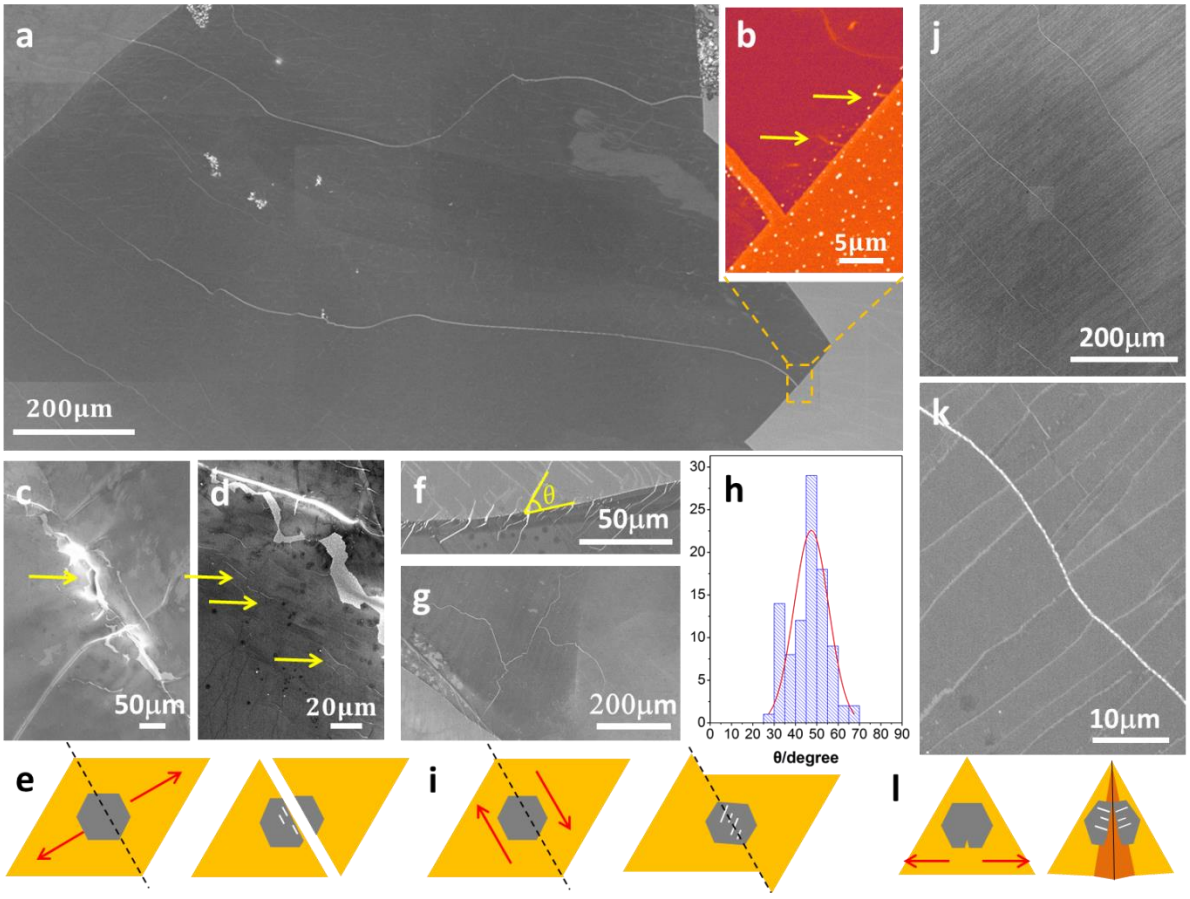


Figure 4-2 Cracks in “fast cooled” graphene samples. (a) SEM image of long cracks across. The cracks originate from graphene edge; propagate through graphene until reach copper grain boundary. (b) Fake-coloured SEM image of nanoparticles etching tracks in graphene edges. (c) SEM image of the cracks in graphene resulting from thermal grooving of the Cu. (d) High-mag SEM image of the tail of the crack in graphene induced by thermal grooving. Secondary cracks running parallel to the main

rift are indicated. (e) Schematic illustration of the formation of cracks in graphene from thermal grooving and its secondary cracks. (f) SEM image of "boundary tears" in graphene from a Cu grain boundary. (g) SEM image of a mm-scale lightning-shaped crack. (h) Histogram of the intersection angles between "boundary tears" and the copper grain boundary. (i) Schematic illustration of the formation of "boundary tears". (j) SEM image of the large cracks which reach the edge of graphene (as in (a)), along with the offshoot side cracks. (k) Higher magnification SEM of the offshoot side cracks stemming from a main crack. (l) Schematic illustration of the formation of long cracks that reach the edge of graphene and its offshoot side cracks.

Numerous types of cracks are found in the fast cooled graphene. Long cracks from the edge taper off and finally diminish after propagating up to millimetres inward the graphene as shown in Figure 4-2 (a). These long cracks are likely to be developed from notches on graphene edge, as shown in Figure 4-2 (b). Small nanoparticles around graphene edge can help to etch graphene[24 25] and forms the notches, some of which further develop in to the large cracks under the strain induce by the cooling process as demonstrated in Figure 4-2 (l). Smaller cracks were found propagating out sideways from the long main cracks, as shown in Figure 4-2 (j) and (k). These shorter offshoot side cracks are of higher density but are narrower than the main long cracks. Thermal grooving in the Cu also causes cracks to form, where a crack often begins at a dimple/groove in the Cu and spreads few hundreds of micrometres along the thermal grooves, as shown in Figure 4-2 (d). The drastic deformation of Cu during solidification tears the graphene film. Secondary cracks running parallel with thermal grooving are also found, shown in Figure 4-2 (d). The third type of main crack, "boundary tears", run parallel with each other and intersect the Cu grain boundary at 45^{o}, as shown in Figure 4-2 (f) and (h). In contrast to the normal-stress-induced cracks

from thermal grooving, shear stress is responsible for the "boundary tears". Cu grains rotate to accommodate stress during solidification, which shears and tears graphene near the Cu grain boundaries.[26] "Boundary tears" release the tensile stress and thus result in strain-free zones in graphene around Cu grain boundaries. Such zones may halt the propagation of the long edge cracks, shown in Figure 4-2 (a). Boundary cracks occasionally develop into larger lightning-shaped cracks (Figure 4-2 (g)).

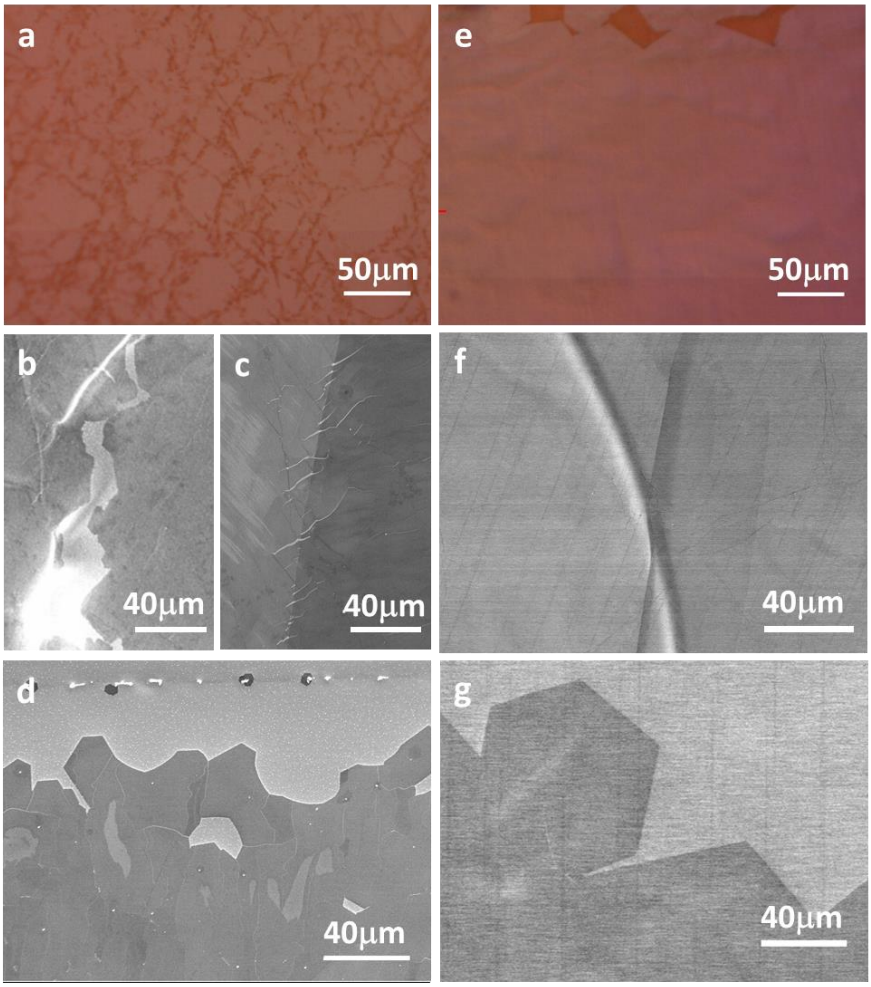


Figure 4-3 Morphology of graphene treated by different cooling processes. (a) Optical microscopic image of fast cooled graphene on Cu. Sample is baked in air at 150 ^{o}C for 15 minutes to oxidize uncovered Cu in order as to increase the optical contrast. Oxidized Cu appears dark red, whilst graphene protected Cu appears light orange. (b)SEM image of a large crack in fast cooled graphene from thermal grooving. (c) SEM image of "Boundary tears" on the fast cooled graphene. (d) SEM image of long cracks from the graphene edge. (e) Optical microscopy image of "regrowth" graphene

on Cu. Sample is partially oxidized in order to increase the image contrast. (f) SEM image of crack-free "regrowth" graphene covering the Cu grain boundary. (g) SEM image of crack-free "re-grown" graphene edge. No long cracks develop from the edge of graphene.

In order to eliminate these cracks graphene was synthesized by a novel "regrowth" process, hereafter referred to as "regrown" graphene. This resulted in substantially better continuity than "fast cooled" graphene. By slowly reducing the temperature from 1090^{o}C – 1060 ^{o}C, the Cu solidifies from its molten state slower than when rapidly cooled, resulting in fewer cracks. Furthermore, by continuing to supply CH_4 during this period, it allows graphene to continue to grow and fill the vacant space left by cracks in the film, actively repairing the cracks. The "regrown" graphene is more continuous and when the sample is baked in air there is no sign of oxidation of the Cu in the main central region, as seen by comparing Figure 4-3 (a) and (e).

4.2.3 Transfer of Graphene by anodic etching of catalyst

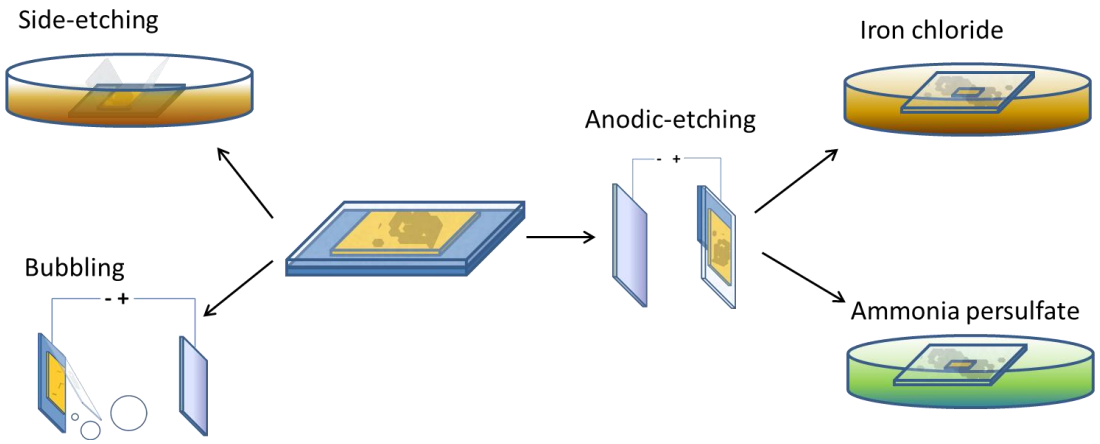


Figure 4-4 Schematic illustrations of different transfer processes. In the "side etching" method, Cu is gradually etched by iron chloride solution leaked in from sample side. In the "bubbling" method, graphene is isolated from the catalyst by delamination. In the "anodic etching" method, W is etched by an electrochemical method. Subsequently, the remaining Cu is dissolved by either iron chloride or ammonium persulfate.

Although the synthesis of graphene by CVD can lead to high quality material, it is the transfer stage that is a major rate-limiting step in the progress of graphene for electronics. The transfer a single graphene layer from one substrate to another without inducing cracks is not trivial. Although several transfer methods have been reported, there is still a lack of studies on the effectiveness of transferring graphene grown on melted Cu to silicon wafers. Here we compare the effect of different transfer methods on the quality of graphene in terms of continuity and surface residues. PMMA is spun onto graphene as a protective supporting layer for all methods discussed. Figure 4-4 schematically illustrates the three transfer methods, and two Cu etchants, studied in this report. In the "side etching" method, the sample floats on the iron chloride solution. Because of the chemical inertness of W, the etchant can only gradually

dissolve Cu from the space between graphene and W substrate. When Cu is totally consumed, the W substrate sinks, leaving the graphene-PMMA film floating on the etchant. In the “bubbling” method, hydrogen bubbles lift the graphene-PMMA film off the Cu substrate. These hydrogen bubbles come from the electrolysis of a 1M sodium hydroxide solution with the sample used as the cathode. Besides the two methods above, we have developed a novel “2-step” transfer method specifically for graphene grown on molten Cu with a W substrate. Firstly, the W substrate is etched by the electrochemical method. This etching step is referred as “anodic etching” hereafter. Following the anodic etching of W, Cu is dissolved with either iron chloride or ammonium persulfate, followed by successive rinsing in water to finish the transfer.

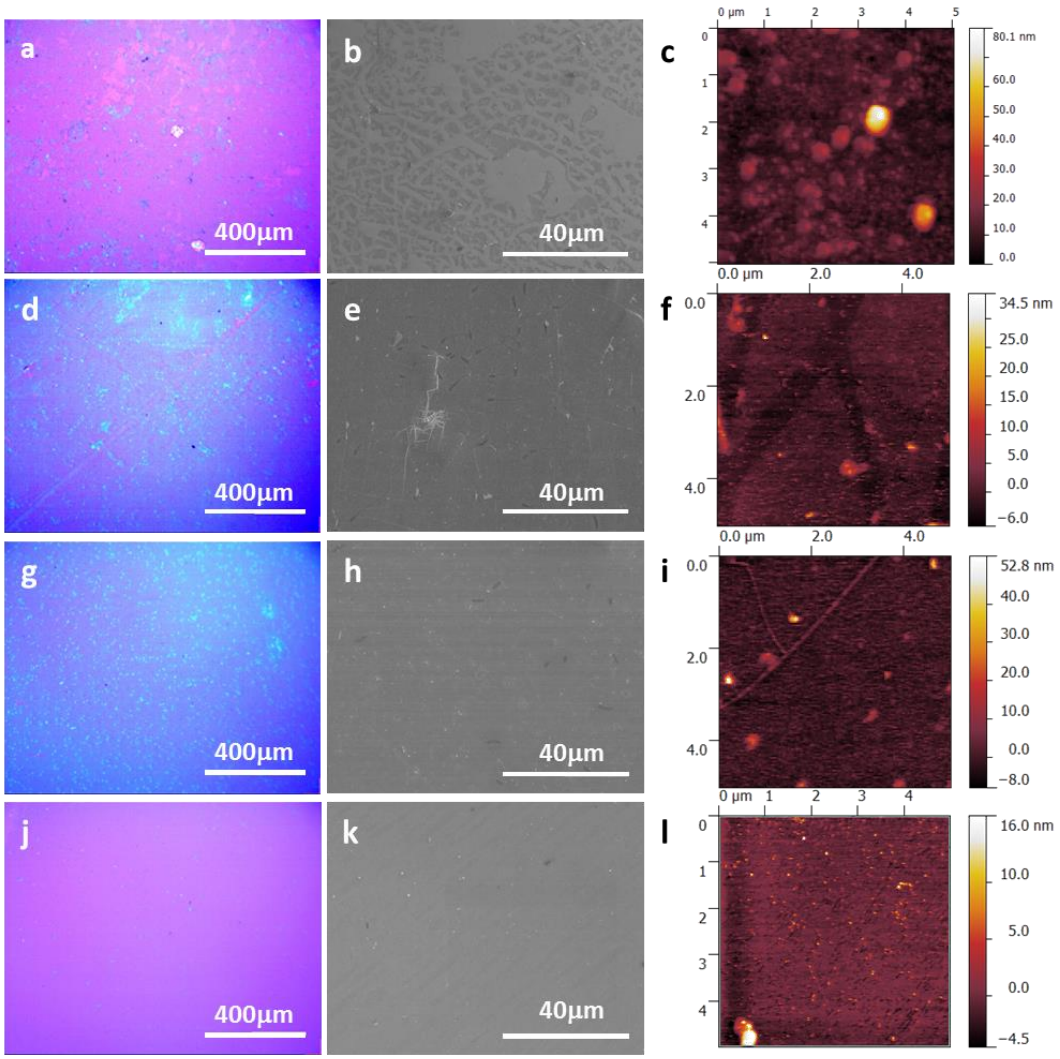


Figure 4-5 Continuity and surface roughness of transferred graphene. (a), (b), (c) Optical microscope, SEM and AFM images of graphene transferred by "bubbling" method. Graphene is shredded and large amounts of surface contamination is found. (d) (e) (f) Optical microscope, SEM and AFM images of graphene transferred by the "side etching" method. Some cracks and holes are found. (g) (h) (i) Optical microscope, SEM and AFM images of graphene transferred by the "2-step" method with Cu etched by iron chloride. Graphene maintains continuity over a large region but some surface residues are found. (j) (k) (l) Optical microscope, SEM and AFM map of graphene transferred by the "2-step" method with Cu etched by ammonia persulfate. Graphene is clean and continuous over a large region. The brightness/contrast of the optical microscope images are adjusted to reveal any surface contamination that might be present.

The transfer process influences the quality of graphene on the silicon wafer in terms

of the continuity and surface contamination. In our experiment, transferring CVD graphene grown on molten Cu by the bubbling method destroys its integrity, as shown in Figure 4-5 (a)-(c). Turbulence caused by hydrogen bubbles twists and cracks the graphene-PMMA film during transfer process. We have noticed, however, some isolated hexagonal domains of monolayer graphene with widths up to 100μm retain better continuity than the continuous film after transfer by the bubbling method. A substantial amount of surface contamination remains on the graphene. The root mean square surface roughness of graphene transferred by bubbling method reaches as high as 7.2nm, which is the highest amongst all methods. Compared to the bubbling method, the side etching method retains better integrity of the graphene. Only few cracks are found across the graphene as shown in Figure 4-5 (e) and (f). However, because of the chemical inertness of W, common etchants like iron chloride or ammonium persulfate cannot dissolve it efficiently. In this way, the etchant can only approach Cu from the space between graphene and W substrate, which results in a slow etching speed. The etchant process generally takes 3 to 5 days to complete. Moreover, W anchors to the bottom of the liquid and distorts the graphene-PMMA film during etching causing further cracks. Bright blue contrast in Figure 4-5 (d) indicates the $FeCl_3$-PMMA residue on graphene. The AFM measurement (Figure 4-5 (f)) confirms the discontinuity of graphene by finding cracks with width around 600nm. The surface roughness is 2.4nm, which is similar with previous reported values of transferred CVD graphene.

Both “side etching” and “bubbling” transfer methods stretch or distort the graphene-PMMA film at a certain stage. The “2-step” etching method, on the other hand, is stress-free therefore preserves the continuity of graphene. The first step of transfer involves oxidizing and dissolving tungsten by anodic etching in sodium hydroxide solution. The reaction requires a high pH solution environment, which is provided by the 2mol/L sodium hydroxide solution in our experiment. W sized $1cm^2$, with 100μm thickness is found to dissolve within 30 minutes by anodic etching. As for the etching of copper, we compare the effect of two Cu etchants, iron chloride and ammonium persulfate on the graphene. When Cu is dissolved by iron chloride, similar amount of $FeCl_3$-PMMA residue is found on graphene as shown in Figure 4-5 (g). On the other hand, not much surface residue appears on the graphene when transferred by ammonium persulfate (Figure 4-5 (j)). Whichever etchant is used, graphene remains crack-free over a centimetre-scale region. We further use AFM to study the surface roughness of 2-step transferred graphene. When Cu is etched by iron chloride, the surface roughness is 3.4nm. This result is compatible with previously reported values of CVD graphene. When Cu is etched by ammonium persulfate, a flatter surface is observed, with a root mean square roughness as low as 1.6nm. It is clear that the ammonium persulfate helps to provide a cleaner graphene sheet than iron chloride copper etchant.

4.2.4 Characterization of the CVD graphene

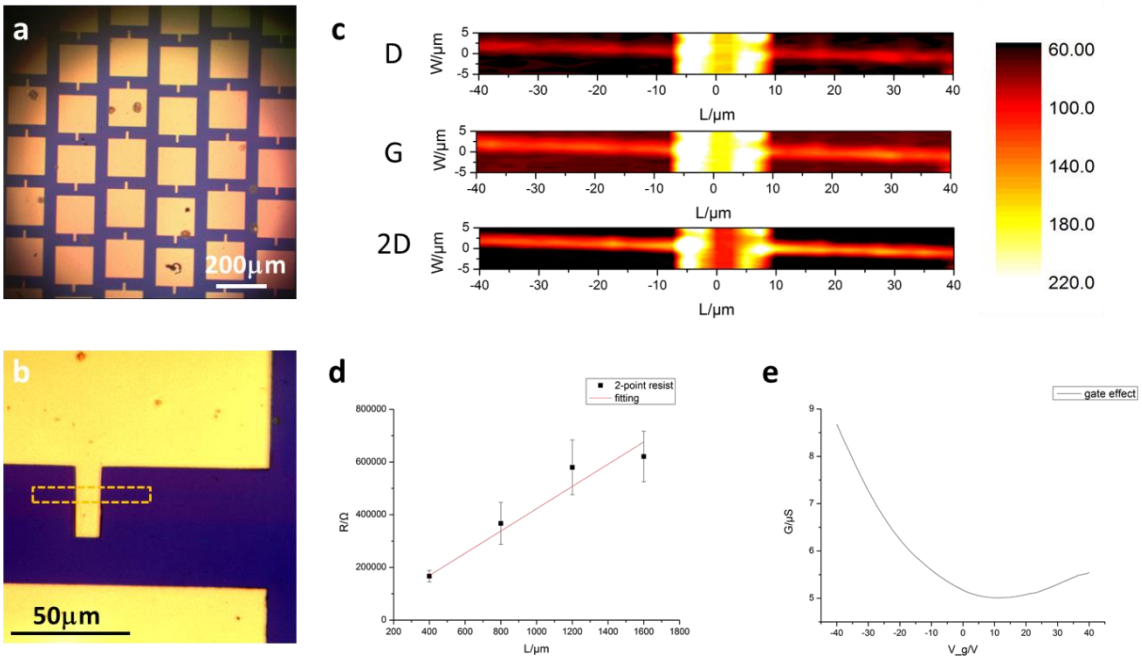


Figure 4-6 Electrical characterization of graphene. (a) Optical microscope image of an array of graphene FETs on a silicon wafer with 300nm oxide. 2 μm-wide graphene ribbons pass under contacts spaced 200 μm apart. (b) Optical microscope image of metal contacts on graphene ribbon. The yellow square marks the region for Raman mapping in (c). (c) D, G and 2D Raman mapping of graphene ribbon crossing a contact. The ratio between 2D and D peak is roughly 2. (d) Resistance of graphene ribbons as a function of different channel lengths. Graphene ribbons remain conductive even when the length-width ratio exceeds 800 and for lengths of 1.6mm. The error bar is calculated as the standard deviation of 5 different graphene ribbons measured in this experiment under 1V bias. (e) Gate dependent conductance of graphene in ambient condition. The channel width and length are 2 μm and 400 μm respectively, source-drain bias is 1V.

To further quantify that the graphene synthesized and transferred following our procedure is continuous across large distances we examined the electrical properties for different length scales. We fabricated arrays of metal electrodes across graphene transferred onto a doped silicon wafer with 300nm oxide layer to measure the conductivity and electronic field effect behaviour using the doped Si as a global back gate. Graphene is trimmed into 2 μm ribbons by electron beam lithography. Arrays of

Cr/Au contacts are then deposited onto the ribbon so that the channel length is $200\ \mu m \times N$, where N is an integer as shown in Figure 4-6 (a). The large aspect ratio of the graphene ribbon ensures the sensitivity of conductivity to the continuity of the graphene. Raman mapping indicates a 2D/G ratio around 2, confirming the single layer nature of graphene as shown in Figure 4-6 (c). A weak D peak is also observed, which may due to defects induced from device fabrication. The conductivity of graphene is measured over different channel lengths. The plot of resistance versus length intercepts the y axis at 240Ω, as shown in Figure 4-6 (d), which results from the contact resistance according to previous reports[27 28]. The resistance of graphene ribbons in our geometry is 422.5Ω/μm and thus can we derive the sheet resistance as 825Ω/□. We also measured the sheet resistance directly on other transferred samples using Van-der-Pauw geometry and obtained similar sheet resistance values. The field effect mobility of the graphene measured in air with this geometry was 1600 $cm^2/(Vs)$, as shown in Figure 4-6 (e). With a smaller length-width ratio, higher mobility is reachable. We notice a hysteresis effect observed in the field effect of graphene, which is likely to be due to the absorption and desorption of water molecules. The transfer curve in Figure 4-6 (e) is averaged over the transfer curves of two gate sweeping directions. Further cleaning processes like ultra-high vacuum annealing, using BN as a substrate, and performing measurements under vacuum should help to further increase the mobility values in our devices.

Conclusion

The results in this paper provide a solution for growth and transfer of large area single layer graphene. Our findings clarify the key factors in each step of growth influencing the quality of graphene film. As a summary, three critical factors, e.g. metal substrate, cooling rate and transfer method, are found to determine the graphene's quality. The metal substrate should be carefully chosen so as to well wet and spread but not form alloy with melted copper. In practice, Mo substrate result the segregation of Mo-Cu alloy when contact with melted copper and break holes in graphene, whilst W substrate enables a continuous graphene sheet. Different cooling rate change the thermal stresses in graphene. A conventional fast cooling process tears graphene because of drastic deformation of Cu during solidification. This problem is addressed by applying the "regrowth" process during cooling. This enables graphene continues to epitaxial grow from the cracks' edge and stitches them. In addition to the synthesis, the choice of transfer process also influences the continuity of graphene. Distortion of graphene-PMMA film during transfer would tear cracks in graphene. A stress-free wet transfer method is developed to minimize the transfer-induced cracks in graphene. Our study will help the further development of large area continuous sheets of high quality monolayer graphene for electronic applications.

4.3 Influence of Substrate to Graphene FET

4.3.1 Introduction

This section aims to provide further studies on the electronic properties of graphene. Most of electronic applications of graphene are realized on certain substrate. Different

from conventional 3D materials, the large surface ratio of 2D materials leads it sensitive to measurement environment. During the measurement of graphene field effect, the effect of substrate is somewhat ignored. In this study, however, we aim to compare the influence of different substrate to the doping level and mobility of graphene. A hydrophobic substrate is found to help reduce the unintentional doping of graphene when measured in ambient condition. The charge carrier mobility of graphene FET also increases when the FET is fabricated on hydrophobic substrate.

4.3.2 Experiment and Materials characterization

Three types of substrates are studied in this experiment, i.e. 300nm SiO2, BN and HMDS modified 300nm SiO2. Graphene grown and transferred according to the method reported in the chapter of methodology (chapter 3) of this thesis. Devices are fabricated by electron beam lithography. All experiments are carried out in ambient condition using Keithley 2400 semiconductor measurement unit.

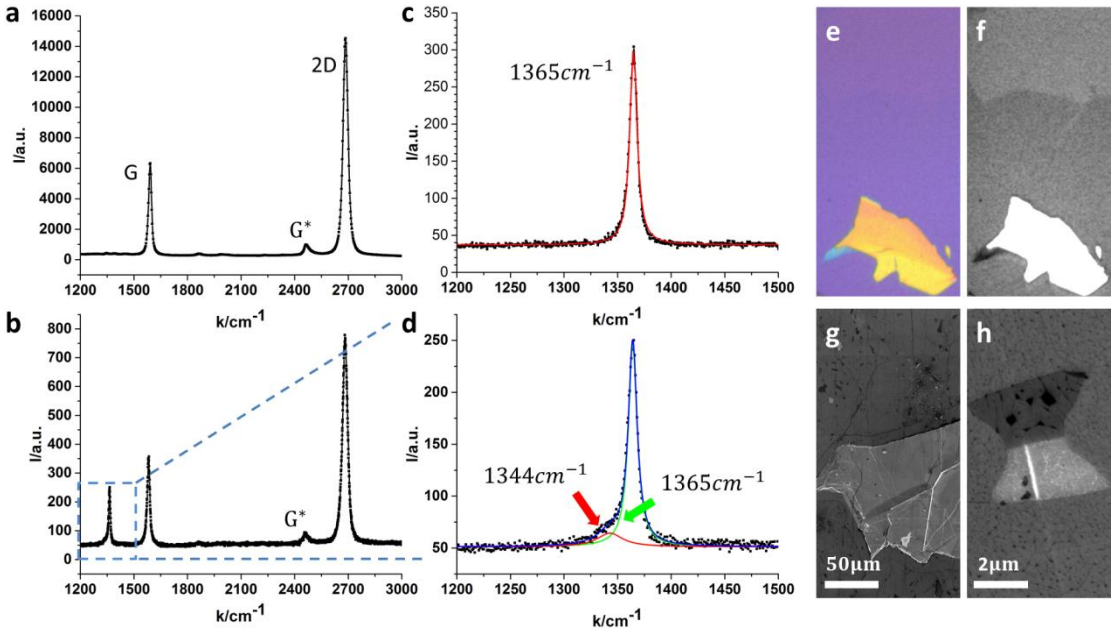


Figure 4-7 Characterization of graphene on BN. (a) Typical Raman spectrum of graphene on silicon. (b) Raman spectrum of graphene on BN. (c) Raman Spectrum of BN. (d) High resolution Raman spectrum of graphene on BN. The D peak of graphene is at $\mathbf{1344cm^{-1}}$ is pointed by the red arrow, while the E2g peak of BN is at $\mathbf{1365cm^{-1}}$ as pointed by the green arrow. (e) Colour optical microscopic image of graphene on BN flake. (f) Red intensity extracted from the RGB value of (f). The contrast between graphene and silicon chip is clear. (g) (h) SEM image of graphene on BN. Image (h) is taken at region where graphene flip over leaving BN exposed.

BN flakes are stamped onto the SiO2 substrate by mechanical exfoliation. Since BN is only used as a substrate in this experiment, we do not pay effort to search for monolayer region of BN. After the stamping of BN flakes, CVD grown graphene is transferred onto the substrate to cover the BN flakes. Raman spectrum of graphene on bare silicon is taken as a reference of graphene used in this experiment as shown in Figure 4-7 (a). We also take the Raman spectrum of BN before the graphene transfer. The Raman peak of multilayer BN flake is found at 1365cm^{-1} as shown in Figure 4-7 (c). This is in consistence with previous reported value for E_{2g} peak of bulk BN.[29] [30] After the transfer of graphene, we confirm the coverage of graphene on BN by both

spectroscopic and microscopic methods. An optical image of BN with transferred graphene is shown in Figure 4-7 (e) and (f). The Raman peak of BN partly overlaps with the D peak of graphene, and appears as an apparently single Raman peak at around 1350cm^{-1}. However, in high resolution Raman spectrum, this peak is separated into two peaks at 1344cm^{-1} and 1365cm^{-1}, which corresponds to the D peak of graphene and E_{2g} peak of BN, as shown in Figure 4-7 (b) and (d). It is interesting to notice that many "bubbles" between BN and graphene is found in the SEM image of graphene covered BN as shown in Figure 4-7 (g) and (h). Some of the bubbles would pop off and flip over under electron beam irradiation leaving a hole in graphene as shown in Figure 4-7(h).

4.3.3 Results and discussion

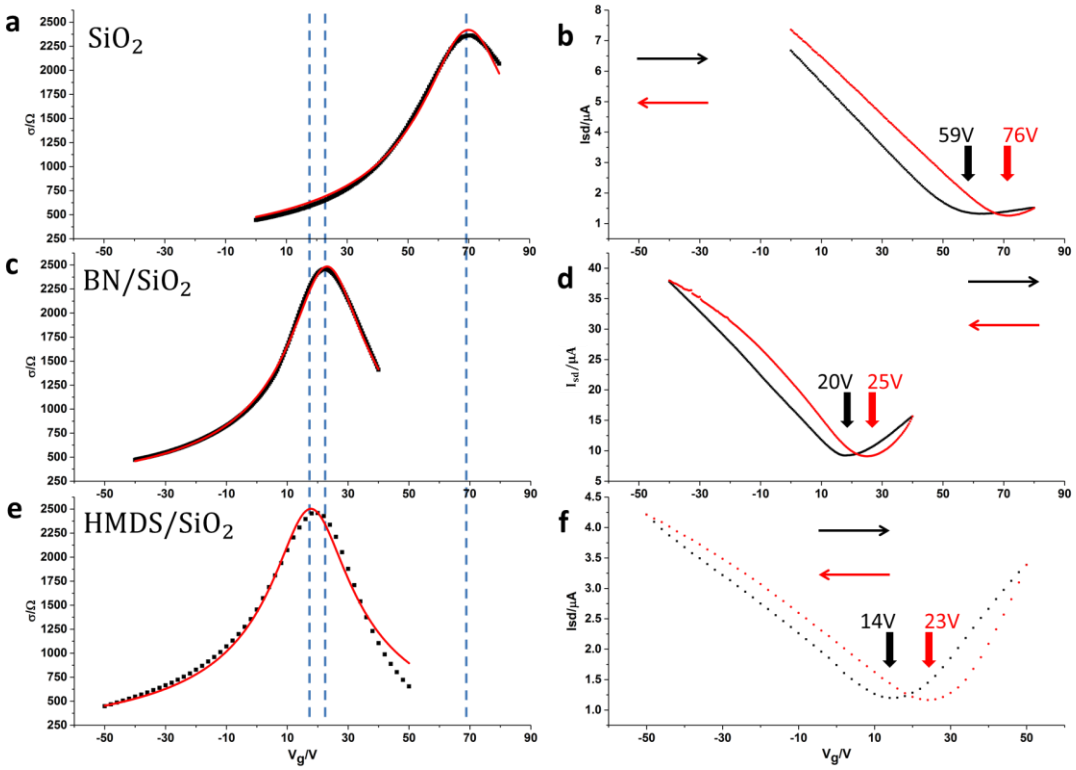


Figure 4-8 Field effect characters of graphene on different substrates. Field effect 2D conductivity of graphene on (a) 300nm SiO2, (c) BN, and (e) HMDS modified SiO2 is measured. A drift of Dirac point is found for different sweeping direction shown in (b) (d) and (f) for graphene on 300nm SiO2, BN and HMDS modified SiO2 respectively.

The ambipolar transfer character shown in Figure 4-8 is unique for graphene field effect transistor. The charge neutrality point, commonly known as the “Dirac point”, is marked by the point where highest channel resistance is reached in the transfer curve. The position of the position of Dirac point is determined by the Fermi level of graphene, which reflects the type and level of doping in graphene. Although it has been recognized that graphene is sensitive to dopant, the influence of substrate is often ignored. Here we present experimental evidence on the influence of different substrate to graphene Fermi level as shown in Figure 4-8

To further understanding the role of substrate, we calculate the 2D resistivity and fit it with a model taking into account of the electron-hole puddle in graphene.

$$\sigma \coloneqq R \times \frac{w}{l} \qquad \text{eq. 4-1}$$

In eq. 4-1, σ is the 2D resistivity of the material (graphene), R is the measured 2-terminal resistance, w is the channel width and l is the channel length. We fit the gate dependent resistivity with a model in account of the electron-hole puddle in the system.[31]

$$\sigma = \sigma_C + \frac{A}{\sqrt{a + \frac{(V - V_D)^2}{B^2}}} \qquad \text{eq. 4-2}$$

Where:

$$A = \frac{1}{en_0\mu} \qquad \text{eq. 4-3}$$

$$B = \frac{en_0}{c_i} \qquad \text{eq. 4-4}$$

In eq. 4-2,eq. 4-3, and eq. 4-4, σ is the 2D resistivity of graphene, σ_C is the resistivity contributed by the contact, V_D is the Dirac point, V is the applied gate voltage, n_0 is the residual charge carrier concentration at Dirac point, e is the absolute value of single electron charge, μ is the carrier mobility, and c_i is the capacity of dielectric layer. In our case, the capacitance of 300nm SiO_2 is known as $c_i = 10.5\text{nF/cm}^2$.

Our experimental results fit well with the model mentioned above. The fitting curve of theoretical value versus experimental results is shown in Figure 4-8 (a), (c) and (e). By fitting with the model above, the Dirac point for as transferred graphene FET on 300nm SiO_2, BN and HMDS modified SiO_2 is found as 69.9V, 23.1V, 17.8V

respectively. Both BN and HMDS modified SiO_2 substrate effectively decrease the p-doping of graphene by pushing the Dirac point back to low gate voltage (around 20V). This value is consistence with exfoliated graphene when measured in air. The residual charge carrier concentration n_0 reflects the doping level of graphene. It is not surprise to found that the residual carrier density for graphene on bare SiO_2 is of the highest, with the value $n_0 = 9.2 \times 10^{11}\text{cm}^{-2}$. This density decrease to $7.67 \times 10^{11}\text{cm}^{-2}$ and $8.05 \times 10^{11}\text{cm}^{-2}$ for graphene on BN and HMDS modified SiO_2 respectively. We also notice a change in mobility of CVD graphene on different substrate. The measured mobility is $2.8 \times 10^3\text{cm}^2/(\text{Vs})$ for graphene on bared 300nm SiO2, and increase to $3.3 \times 10^3\text{cm}^2/(\text{Vs})$ for graphene on BN and $3.2 \times 10^3\text{cm}^2/(\text{Vs})$ for graphene on HMDS modified SiO_2 substrate. The improving charge carrier mobility observed in our experiment is significant but not as high as previous reported value for BN substrate[32] [15] or HMDS modified substrate[33]. Our result is however comparable with some recent reports.[34]

Hysteresis in field effect measurement of graphene is commonly found in experiment. We found the different substrate does not only influence the doping level of graphene and its mobility, but also influence the hysteresis in measurement. We characterize the hysteresis in field effect measurement by the shift of Dirac point between different sweeping directions. The black curves in Figure 4-8 (b) (d) and (f) is transfer curve of device measured from p-type region to n-type region of graphene, and the red curve is measured from the reverse direction. The difference in Dirac point is 17V, 5V and 9V

for graphene on SiO_2, BN and HMDS modified SiO_2 respectively.

4.3.4 Conclusion

Our measurement results indicate a decreasing of doping level of graphene on BN and HMDS processed SiO_2. It is interesting to notice that graphene on this two substrates also exhibits a smaller hysteresis compared with on bare SiO_2. Previous researches indicate that the hysteresis is linked with the trapped water between graphene and substrate.[35] However, since the HMDS only modify the surface of SiO_2, any trapping states in the dielectric layer should not explain our observation. We notice, however, both BN and HMDS modified SiO_2 are hydrophobic and thus less amount of absorb water would appear on the surface them. On the contrary, the –OH function group on bare SiO_2 surface tend to absorb water molecules. In this way, the hysteresis is likely to be due to the trapped water molecule between graphene and substrate.

Graphene field effect transistor is fabricated with the CVD graphene. We provide experimental evidence on the effect of different substrate to the electronic properties of graphene. In particular, it is found that the hydrophobic substrate helps to decrease the substrate induced p-dope of graphene, inhibits the hysteresis and increase the charge carrier mobility.

Reference

(1) Fan, Y.; He, K.; Tan, H.; Speller, S.; Warner, J. H. Crack-Free Growth and

Transfer of Continuous Monolayer Graphene Grown on Melted Copper. *Chem. Mater.* **2014**, *26*, 4984–4991.

(2) Han, S.-J.; Garcia, A. V.; Oida, S.; Jenkins, K. a.; Haensch, W. Graphene Radio Frequency Receiver Integrated Circuit. *Nat. Commun.* **2014**, *5*, 3086.

(3) Wu, Y.; Lin, Y.; Bol, A. a; Jenkins, K. a; Xia, F.; Farmer, D. B.; Zhu, Y.; Avouris, P. High-Frequency, Scaled Graphene Transistors on Diamond-like Carbon. *Nature* **2011**, *472*, 74–78.

(4) Hueso, L. E.; Pruneda, J. M.; Ferrari, V.; Burnell, G.; Valdés-Herrera, J. P.; Simons, B. D.; Littlewood, P. B.; Artacho, E.; Fert, A.; Mathur, N. D. Transformation of Spin Information into Large Electrical Signals Using Carbon Nanotubes. *Nature* **2007**, *445*, 410–413.

(5) Tombros, N.; Jozsa, C.; Popinciuc, M.; Jonkman, H. T.; vanWees, B. J. Electronic Spin Transport and Spin Precession in Single Graphene Layers at Room Temperature. *Nature* **2007**, *448*, 571–574.

(6) Bonaccorso, F.; Sun, Z.; Hasan, T.; Ferrari, a. C. Graphene Photonics and Optoelectronics. *Nat. Photonics* **2010**, *4*, 611–622.

(7) Wang, X.; Zhi, L.; Müllen, K. Transparent, Conductive Graphene Electrodes for Dye-Sensitized Solar Cells. *Nano Lett.* **2008**, *8*, 323–327.

(8) Graphene, S.; Wu, J.; Agrawal, M.; Becerril, A.; Bao, Z.; Liu, Z.; Chen, Ḱ. Y.; Peumans, P.; Chen, Y.; Peumans, P. Organic Light-Emitting Diodes on Solution-Processed Graphene Transparent Electrode. *ACS Nano* **2010**, *4*, 43–48.

(9) Han, T.-H.; Lee, Y.; Choi, M.-R.; Woo, S.-H.; Bae, S.-H.; Hong, B. H.; Ahn, J.-H.; Tae-Woo, L.; Lee, T.-W. Extremely Efficient Flexible Organic Light-Emitting Diodes with Modified Graphene Anode. *Nat. Photonics* **2012**, *6*, 105–110.

(10) de Heer, W. a.; Berger, C.; Wu, X.; First, P. N.; Conrad, E. H.; Li, X.; Li, T.; Sprinkle, M.; Hass, J.; Sadowski, M. L.; Potemski, M.; Martinez, G. Epitaxial Graphene. *Solid State Commun.* **2007**, *143*, 92–100.

(11) Lin, Y.; Dimitrakopoulos, C.; Jenkins, K. a; Farmer, D. B.; Chiu, H.-Y.; Grill, A.; Avouris, P. 100-GHz Transistors from Wafer-Scale Epitaxial Graphene. *Science.* **2010**, *327*, 662–662.

(12) Berger, C.; Song, Z.; Li, X.; Wu, X.; Brown, N.; Naud, C.; Mayou, D.; Li, T.; Hass, J.; Marchenkov, A. N.; Conrad, E. H.; First, P. N.; de Heer, W. a. Electronic Confinement and Coherence in Patterned Epitaxial Graphene. *Science* **2006**, *312*, 1191–1996.

(13) Cao, H.; Yu, Q.; Jauregui, L. a.; Tian, J.; Wu, W.; Liu, Z.; Jalilian, R.; Benjamin, D. K.; Jiang, Z.; Bao, J.; Pei, S. S.; Chen, Y. P. Electronic Transport in Chemical Vapor Deposited Graphene Synthesized on Cu: Quantum Hall Effect and Weak Localization. *Appl. Phys. Lett.* **2010**, *96*, 122106.

(14) Li, X.; Magnuson, C. W.; Venugopal, A.; An, J.; Suk, J. W.; Han, B.; Borysiak, M.; Cai, W.; Velamakanni, A.; Zhu, Y.; Fu, L.; Vogel, E. M.; Voelkl, E.; Colombo, L.; Ruoff, R. S. Graphene Films with Large Domain Size by a Two-Step Chemical Vapor Deposition Process. *Nano Lett.* **2010**, *10*, 4328–

4334.

(15) Gannett, W.; Regan, W.; Watanabe, K.; Taniguchi, T.; Crommie, M. F.; Zettl, a. Boron Nitride Substrates for High Mobility Chemical Vapor Deposited Graphene. *Appl. Phys. Lett.* **2011**, *98*, 242105.

(16) Li, X.; Magnuson, C. W.; Venugopal, A.; Tromp, R. M.; Hannon, J. B.; Vogel, E. M.; Colombo, L.; Ruoff, R. S. Large-Area Graphene Single Crystals Grown by Low-Pressure Chemical Vapor Deposition of Methane on Copper. *J. Am. Chem. Soc.* **2011**, *133*, 2816–2819.

(17) Zhou, H.; Yu, W. J.; Liu, L.; Cheng, R.; Chen, Y.; Huang, X.; Liu, Y.; Wang, Y.; Huang, Y.; Duan, X. Chemical Vapour Deposition Growth of Large Single Crystals of Monolayer and Bilayer Graphene. *Nat. Commun.* **2013**, *4*, 2096.

(18) Ogawa, Y.; Hu, B.; Orofeo, C. M.; Tsuji, M.; Ikeda, K.; Mizuno, S.; Hibino, H.; Ago, H. Domain Structure and Boundary in Single-Layer Graphene Grown on Cu(111) and Cu(100) Films. *J. Phys. Chem. Lett.* **2012**, *3*, 219–226.

(19) Suk, J. W.; Kitt, A.; Magnuson, C. W.; Hao, Y.; Ahmed, S.; An, J.; Swan, A. K.; Goldberg, B. B.; Ruoff, R. S. Transfer of CVD-Grown Monolayer Graphene onto Arbitrary Substrates. *ACS Nano* **2011**, *5*, 6916–6924.

(20) Wu, Y.; Fan, Y.; Speller, S.; Creeth, G. Large Single Crystals of Graphene on Melted Copper Using Chemical Vapor Deposition. *ACS …* **2012**, *6*, 5010–5017.

(21) Geng, D.; Wu, B.; Guo, Y.; Huang, L.; Xue, Y.; Chen, J.; Yu, G.; Jiang, L.; Hu, W.; Liu, Y. Uniform Hexagonal Graphene Flakes and Films Grown on Liquid Copper Surface. *Proc. Natl. Acad. Sci.* **2012**, *109*, 7992–7996.

(22) Wu, B.; Geng, D.; Xu, Z.; Guo, Y.; Huang, L.; Xue, Y.; Chen, J.; Yu, G.; Liu, Y. Self-Organized Graphene Crystal Patterns. *NPG Asia Mater.* **2013**, *5*, e36.

(23) Geng, D.; Wu, B.; Guo, Y.; Luo, B.; Xue, Y.; Chen, J.; Yu, G.; Liu, Y. Fractal Etching of Graphene. *J. Am. Chem. Soc.* **2013**, *135*, 6431–6434.

(24) Datta, S. S.; Strachan, D. R. D.; Khamis, S. M. S.; Johnson, A. T. C. Crystallographic Etching of Few-Layer Graphene. *Nano Lett.* **2008**, *8*, 1912–1915.

(25) Wang, X.; Dai, H. Etching and Narrowing of Graphene from the Edges. *Nat. Chem.* **2010**, *2*, 661–665.

(26) Warren, J. a.; Kobayashi, R.; Lobkovsky, A. E.; Craig Carter, W. Extending Phase Field Models of Solidification to Polycrystalline Materials. *Acta Mater.* **2003**, *51*, 6035–6058.

(27) Xia, F.; Perebeinos, V.; Lin, Y.; Wu, Y.; Avouris, P. The Origins and Limits of Metal-Graphene Junction Resistance. *Nat. Nanotechnol.* **2011**, *6*, 179–184.

(28) Nagashio, K.; Nishimura, T.; Kita, K.; Toriumi, a. Contact Resistivity and Current Flow Path at Metal/graphene Contact. *Appl. Phys. Lett.* **2010**, *97*, 143514.

(29) Reich, S.; Ferrari, a.; Arenal, R.; Loiseau, a.; Bello, I.; Robertson, J. Resonant Raman Scattering in Cubic and Hexagonal Boron Nitride. *Phys. Rev. B* **2005**, *71*, 1–12.

(30) Gorbachev, R. V.; Riaz, I.; Nair, R. R.; Jalil, R.; Britnell, L.; Belle, B. D.; Hill, E. W.; Novoselov, K. S.; Watanabe, K.; Taniguchi, T.; Geim, A. K.; Blake, P.

Hunting for Monolayer Boron Nitride: Optical and Raman Signatures. *Small* **2011**, *7*, 465–468.

(31) Chiu, H. Y.; Perebeinos, V.; Lin, Y. M.; Avouris, P. Controllable P-N Junction Formation in Monolayer Graphene Using Electrostatic Substrate Engineering. *Nano Lett.* **2010**, *10*, 4634–4639.

(32) Dean, C. R.; Young, a F.; Meric, I.; Lee, C.; Wang, L.; Sorgenfrei, S.; Watanabe, K.; Taniguchi, T.; Kim, P.; Shepard, K. L.; Hone, J. Boron Nitride Substrates for High-Quality Graphene Electronics. *Nat. Nanotechnol.* **2010**, *5*, 722–726.

(33) Chowdhury, S. F.; Sonde, S.; Rahimi, S.; Tao, L.; Banerjee, S.; Akinwande, D. Improvement of Graphene Field-Effect Transistors by Hexamethyldisilazane Surface Treatment. *Appl. Phys. Lett.* **2014**, *105*, 2012–2017.

(34) Kim, S. M.; Hsu, A.; Park, M. H.; Chae, S. H.; Yun, S. J.; Lee, J. S.; Cho, D.-H.; Fang, W.; Lee, C.; Palacios, T.; Dresselhaus, M.; Kim, K. K.; Lee, Y. H.; Kong, J. Synthesis of Large-Area Multilayer Hexagonal Boron Nitride for High Material Performance. *Nat. Commun.* **2015**, *6*, 8662.

(35) Wang, H.; Wu, Y.; Cong, C.; Shang, J.; Yu, T. Hysteresis of Electronic Transport in Graphene Transistors. *ACS Nano* **2010**, *4*, 7221–7228.

5

Electronics and Optoelectronics with CVD WS_2

Contents

5.1 Introduction 152

5.2 WS_2 Monolayer Photoconductor 153

5.2.1 Introduction 153

5.2.2 Materials characterization 155

5.2.3 Device Fabrication and Experiments 159

5.2.4 Results and Discussion 161

Reference 172

*Section 5.2 is modified from the publication in reference [1]

** WS_2 domains in Section 5.2 of this chapter are grown by Ms Yingqiu Zhou.

5.1 Introduction

Transitional metal chalcogenides (TMDC) are a family of materials that in the form of MA_2, where M = Mo or W and A = S, Se, or Te. Although the electronic properties of these materials vary from super conductor to metal and to semiconductor when in their bulk form, they are all semiconductor when reduced to one-layer thick. This chapter aims to cast light on the electronic and optoelectronic device application of single layer WS_2, who is a represent of the TMDC family.

5.2 WS_2 Monolayer Photoconductor

5.2.1 Introduction

2D materials like graphene and transitional metal dichalcogenides (TMDC) have been proposed and applied to fabricate ultrathin photodetectors.[2 3] The monolayer materials are ideal for in-chip photonics devices because they are "space-economic" in vertical direction and compatible with conventional lithography routine. Among the 2D families, graphene has been thoroughly studied due to its longest history after discovery. Graphene have with many advantages in favour of sensor applications chemical inertia[4], high charge carrier mobility[5 6 7] and good mechanical strength[8 9]., however its disadvantages are also in significance. Graphene based photo sensors generally suffer from a high dark current[2 10], due to the its zero-bandgap. Unlike graphene, 2D semiconductors with a finite bandgap would limit the dark current and thus is promising candidate for the applications in photo detectors.

The 2D TMDC family is a family of materials that a layer of transition metal, like Mo or W, sandwiches between two layer of chalcogenide atoms, like S, Se or Te.[3] Large scale production of TMDC monolayers are realised thanks to the recent development in CVD growth of TMDC 2D materials.[11 12 13 14] Comparing with other 2D semiconductors like black phosphorus[15], 2D materials belong to TMDC family exhibits better stability in ambient, even harsher, environment.[16] In this way, monolayer TMDCs are promising candidates for the fabrication of robust device. In

the case of photo-sensing, monolayer TMDCs are direct band semiconductors[3], which warrantee a high photon-electron conversion rates[17 18]. For example, WS_2 has a direct band-gap in the visible light region (~2eV), accompanied by strong photo absorption of 5%-10% for a monolayer[19].

Many types of photodetectors have been fabricated with 2D materials, with a general trend of reverse dependence on the photoresponse and band width. Graphene photodetectors with light absorbing quantum dots exhibit a photoresponsivity of around 10^8 A/W, and a slow response time of up to several seconds[20]. On the other hand, the bandwidth of graphene photo detectors without a photo-gating layer can be wider than 1GHz, but the photoresponsivity is of the scale of mA/W[21 22]. TMDC-based photodetectors exhibit diverse photoresponse behaviour. Ohmic contacts are generally assumed for Ti contacted TMDCs, which in turn leads to a small ratio of the photocurrent (I_{bright}) to dark current (I_{dark}), (I_{bright}/I_{dark}) [23 24]. The photoresponsivity of TMDC based photodetector varies 9 orders of magnitude from the scale of μA/W to kA/W, while the response time varies 3 orders of magnitude from the scale of ms to s [25 26 27 23 28]. These large variations are due to a number of factors, such as input laser power, but clearly further detailed studies are needed to reveal more insights into the mechanisms behind photoconductors that utilize monolayer TMDCs.

This section will discuss the application of chemical vapour deposited (CVD) WS_2 as a photo detector. Metal-semiconductor-metal (MSM) photo detectors using WS_2 as the semiconductor photo-sensing material is fabricated on silicon chip. The Schottky barrier is measured by fitting the room-temperature IV curve with the modified thermionic emission current. We discover a lowering of Schottky barrier when the device is illuminated. Our finding enables a new type of 2D conductor based on the light-induced Schottky barrier lowering.

5.2.2 Materials characterization

The good coverage of monolayer WS_2 grown by CVD enables the fabrication of WS2 photo detector arrays on single chip. Gold electrodes are used to form Schottky junctions between the metal contacts and semiconductor, which is required for a MSM photodetector.[29] A Schottky barrier is formed using a high working function metal (e.g. Au) as the contact electrode and a semiconductor with higher Fermi level (e.g. n-type WS_2).[30] The appearance of Schottky barrier together with the band gap in 2D-WS_2 effectively inhibits the dark current to below the measurement limit of equipment in this experiment ($<10^{-11}$ A). The channel length varies from 0.2 – 6.4 μm to explore how this affects the photo-responsivity and gain factors of the devices, with the aim of increasing device performance.

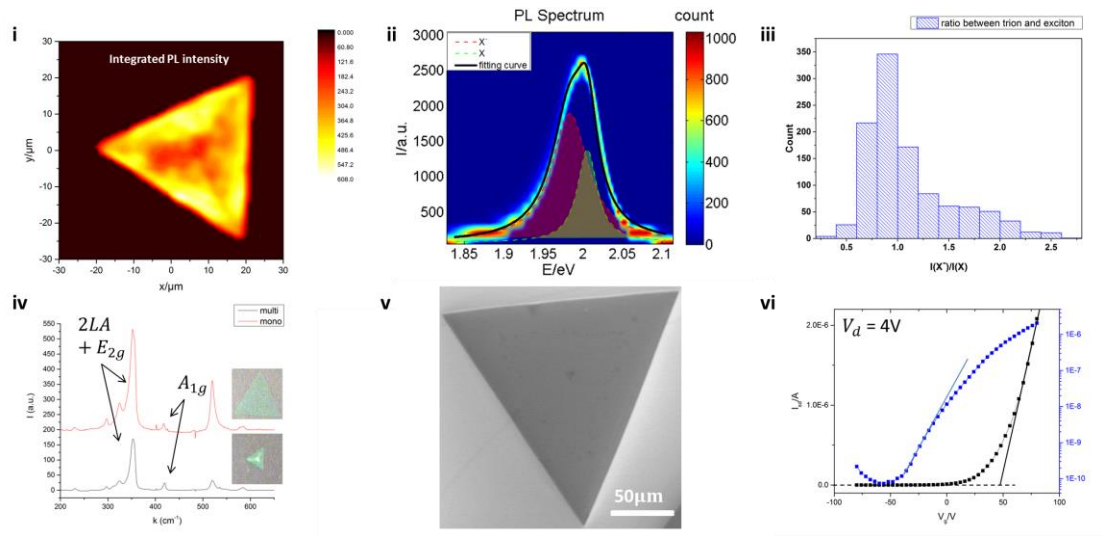


Figure 5-1 (i) Photoluminescence (PL) integrated intensity mapping of one WS_2 domain. PL intensity of monolayer WS_2 is much stronger than it in multilayer WS_2. The ratio between PL peak and Raman peak is used to identify the layer number of WS_2 in this work. (ii) Statistics of PL Spectrum of CVD-monolayer WS_2. The Colour bar in map represents the count of samples. Black solid line is the averaged PL spectrum of all samples, which splits into two peaks corresponding with trion (red peak) and exciton (green peak). Lorentz peak is used for fitting. (iii) Ratio between integrated intensity of trion and exciton. The ratio between these two peaks is proportion to the doping concentration as elaborated in the main text. (iv) Raman spectrum of CVD WS_2. The intensity ratio between ($2LA+E_{2g}$) peak and A_{1g} is used to confirm the layer number of WS_2. Insertions are the optical microscopic image of monolayer (above) and multilayer (below) WS2. (v) SEM image of as-grown WS_2 domain. (vi) Transfer characteristics of a WS_2 field effect transistor (FET). The threshold voltage is 46V and field effect mobility is $\mathbf{4.2 cm^2/(Vs)}$, which is determined by the intercept with I = 0 and slope of the black solid line respectively. The subthreshold swing (slope of blue line) is 17V/dec, which indicates a high density of trap states.

WS2 single crystals domains that used in this experiment are characterized before any electronic measurement. The growth method is described in the method part of this section using a previously reported method with slight modification[31]. The monolayer nature of the WS_2 triangular crystals in this work is confirmed by both photoluminescence (PL) and Raman spectroscopy. Single layer WS_2 domains emit much stronger PL than multi-layer domains due to their direct band gap[32]. A typical

PL intensity mapping from a monolayer WS_2 domain is shown in Figure 5-1 (i). The ratio between the $2LA + E_{2g}$ and A_{1g} peaks in the Raman spectrum is another indicator of the layer number of the WS_2 crystal[33]. The Raman spectrum shown in Figure 5-1 (iv) correlates with the PL analysis in terms of layer number. Some smaller multilayer domains of WS_2 are occasionally found, which is shown as reference in the inset of Figure 5-1 (iv).

The ratio between trion and exciton in PL spectrum of 2D-TMDC indicates the doping level of the material. PL spectra from over 1000 sample points are collected in order to have good statistics in the measurement as shown in Figure 5-1 (ii). The PL spectrum is repeatable over different sample spots, which can be well-fitted by two peaks that correspond to trion (around 1.98eV, red peak in Figure 5-1) and exciton (around 2.02eV, green peak Figure 5-1)[34] emission. The significant trion peak in PL suggest CVD WS_2 be strongly doped.[34] [35] The dopant could be introduced by the transfer process[36] or substrate[37], but is not changeable within this experiment condition. The doping concentration is further estimated by the ratio between spectral intensities of trion and exciton (Figure 5-1 (iii)) according to reference [34] and [35]:

$$\frac{N_X n_e}{N_{X^-}} = \left(\frac{16\pi m_X m_e}{h^2 m_{X^-} \beta}\right) e^{-\beta E_b} \qquad \text{eq. 5-1}$$

$$\frac{I_{X^-}}{I_X} = \frac{\gamma_{X^-} N_{X^-}}{\gamma_X N_X} \qquad \text{eq. 5-2}$$

In eq. 5-1 and eq. 5-2, N_X is the population of exciton, N_{X^-} is the population of trion, n_e is the concentration of electron, m_X (or m_{X^-}) is the effective mass of exciton (or trion), m_e is the effective mass of electron, $\beta = \frac{1}{k_B T}$ is the Boltzmann factor, E_b is the binding energy, I_X (or I_{X^-}) is the integral intensity of exciton (or trion), and γ_X (or γ_{X^-}) is the radiative decay rate of exciton (or trion). By fitting experimental data (Figure 5-1 (ii)) with equations eq. 5-1 and eq. 5-2, the average intrinsic doping concentration is determined as $7 \times 10^{17} m^{-2}$, in similar to typical reported value of WS_2.[34]

Field effect transistors (FET) are fabricated as a prototype of our MSM photo detector as well as to further characterize charge carrier and mobility of the CVD WS_2. Typical transfer curve of FETs with 6.4μm channel length 4μm channel width as Figure 5-2 (iii,f) is present in Figure 5-1 (vi). These FETs display n-type behaviour and the threshold gate voltage is determined by the on-set of the conduction, as shown in Figure 5-1 (vi). Field effect mobility is calculated according to the linear region of the transfer character:

$$\mu = \frac{\mathrm{dI_{sd}}}{\mathrm{dV_g}} \frac{\mathrm{L}}{\mathrm{W}} \frac{1}{\mathrm{V_{sd}} \mathrm{C_i}} \qquad \text{eq. 5-3}$$

In eq. 5-3, μ is the field effect mobility, I_{sd} is the source-drain current, V_g is gate voltage, $\frac{L}{W}$ is the ration between channel length and channel width, V_{sd} is the bias and C_i is the gate capacitance per unit area. The field effect mobility is determined as $4.2 \mathrm{cm}^2/(\mathrm{Vs})$ by the slope of the linear region of transfer curve as shown in black line, Figure 5-1 (vi). This matches well with previous reported values of mobility measured

under ambient environment[38] [24]. However, the significant subthreshold swing (17V/dec) in the transfer character of our CVD WS_2 (blue line in Figure 5-1 (vi)) suggest an abundance of surface trap states[39]. The subthreshold swing is increased by the existence of mid-band gap trap states, which is expressed as in eq. 5-4. [39]

$$S = \frac{ln10}{e\beta}(1 + \frac{e^2}{C_i}N_{trap}) \qquad \text{eq. 5-4}$$

In eq. 5-4, S is subthreshold swing, $\beta = \frac{1}{k_B T}$ is the Boltzmann factor, e is the absolute value of single electron charge, C_i is the capacitance per unit area, N_{trap} is the density of trap states. The subthreshold swing is measured by the slope of subthreshold region in the logarithmic plot of the transfer curve. According to eq. 5-4, we calculate a trap state density of $1.9 \times 10^{17} m^{-2} eV^{-1}$, which is in consist with surface state density reported in 3D bulk materials[30] [40], as well as in MoS_2 transistors[41].

5.2.3 Device Fabrication and Experiments

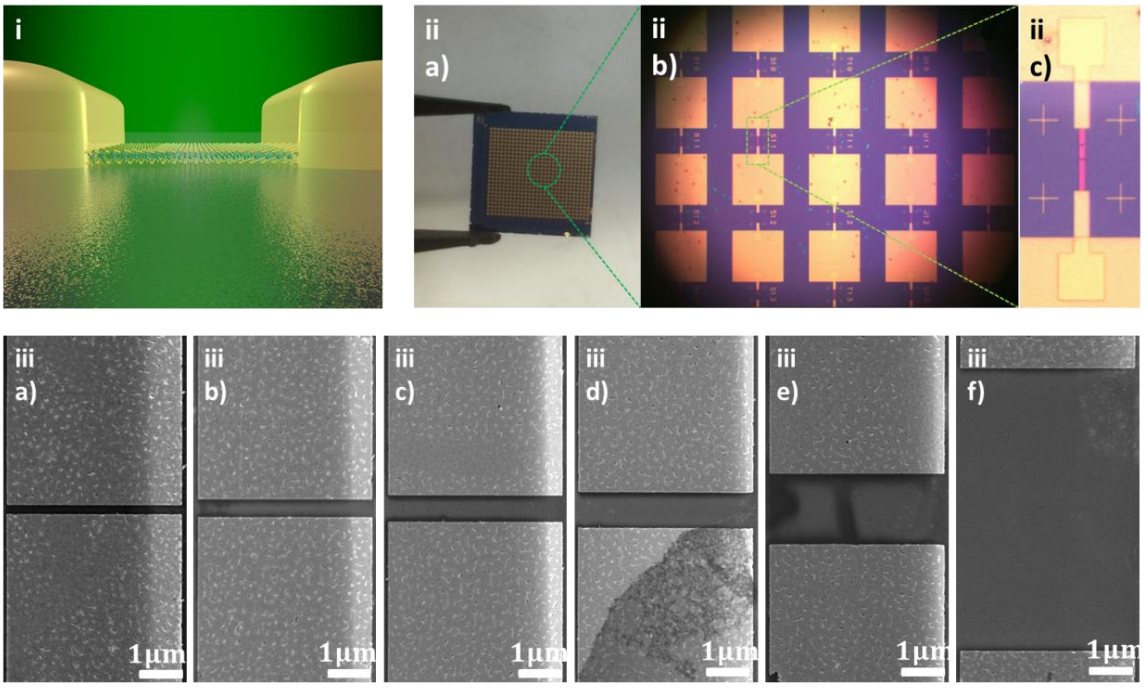


Figure 5-2 Photodetectors on chip (i) Schematic illustration of a metal-semiconductor-metal (MSM) photodetector with monolayer WS_2 between two gold electrodes and 532nm laser illumination. (ii) a)–c) Optical images of devices on silicon chip. (ii) a) Photograph of the array of 24 x 17 devices on 1cm x 1cm silicon chip. (ii) b) Optical microscopic image of device lay-outs. (ii) c) Optical microscopic image of a pair of gold contacts. The pink colour of gold contact is due to the thin thickness (30nm) of them. The number of devices and pitch size is determined to optimize the possibility of contact sparsely distributed WS_2 on silicon chip. (iii) a)-f) Scanning electron microscopy (SEM) image of gold contacts on WS_2 with channel length varying from 200nm to 6400nm.

We fabricated metal-semiconductor-metal photodetectors using the CVD grown WS_2 with variations in the channel length. The WS_2 domains are transferred from the growth substrate onto a new substrate for device fabrication. Details of the growth and transfer method are recorded in the method part. An array (24 x 17) of devices is fabricated on the silicon chip with a pitch size of 300 µm. More than 400 photodetectors are fabricated on one chip in total with about 10% of them works. The number of and pitch between devices are set to maximize the yield rate of working

photodetectors. Optical images of the fabricated devices are shown in Figure 5-2 (ii) a)-c). Photodetectors with 6 different channel length, 200nm, 400nm, 600nm, 800nm, 1600nm and 6400 nm respectively, are fabricated, Figure 5-2 (iii) a)-f). The MSM photodetectors are tested with a 532nm laser with different intensity as schematically illustrated in Figure 5-2 (a). Following previous reported measurement, the photo current is measured by subtracting the dark current off from IV current measured in illumination.[23] Only devices fabricated on one monolayer region of single triangle domain are measured in our experiment so as to rule out any influence of layer number and grain boundary.

5.2.4 Results and Discussion

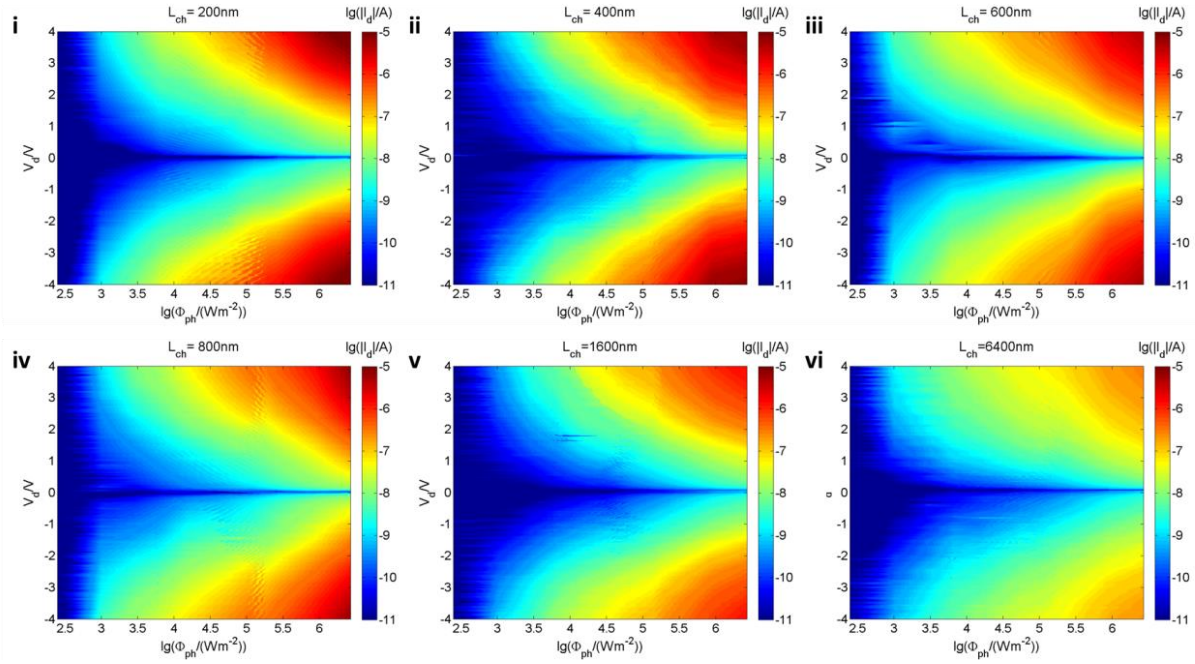


Figure 5-3. Maps of source-drain current in response to source-drain bias and incident laser intensity. Colours in map (i) to (vi) represent absolute value of drain current in 10-based-logarithmic scale (as marked in the colour bar). The range of colour scale in all size maps is same (from 10pA to 10μA) for the convenience of comparison. X axis

and Y axis are 10-based-logarithm of incident illumination intensity and source-drain bias respectively.

Photo-response of devices with different channel lengths (200nm, 400nm, 600nm, 800nm, 1600nm and 6400nm) is measured as a function of source-drain bias and incident light intensity as shown in Figure 5-3. The dark current keeps lower than 10pA (, which is the measurement limit of Keithley 2400 LV SMU used in the experiment,) for devices with all 6 different channel length. The negligible dark current exclude the contribution of tunnelling current in our experimental set-up, which, however, play significant role in short-channel GaSe photo detector under high bias[42]. Although the dark current remains undetectable no matter what channel length and source drain bias, the photocurrent is proved to depend on both. The photocurrent negatively depends on the device channel length as compared in Figure 5-3 (i) to (vi). Photocurrent at a given bias reaches the maximum value at the scale of $10\mu A$ in $\pm 4V$ biased 200nm-channel-length devices as shown in Figure 5-3 (i), while decreases to about 1% of that value in 6400nm-channel-length devices. Higher photo-responsivity for devices with shorter channel lengths and larger bias is found.

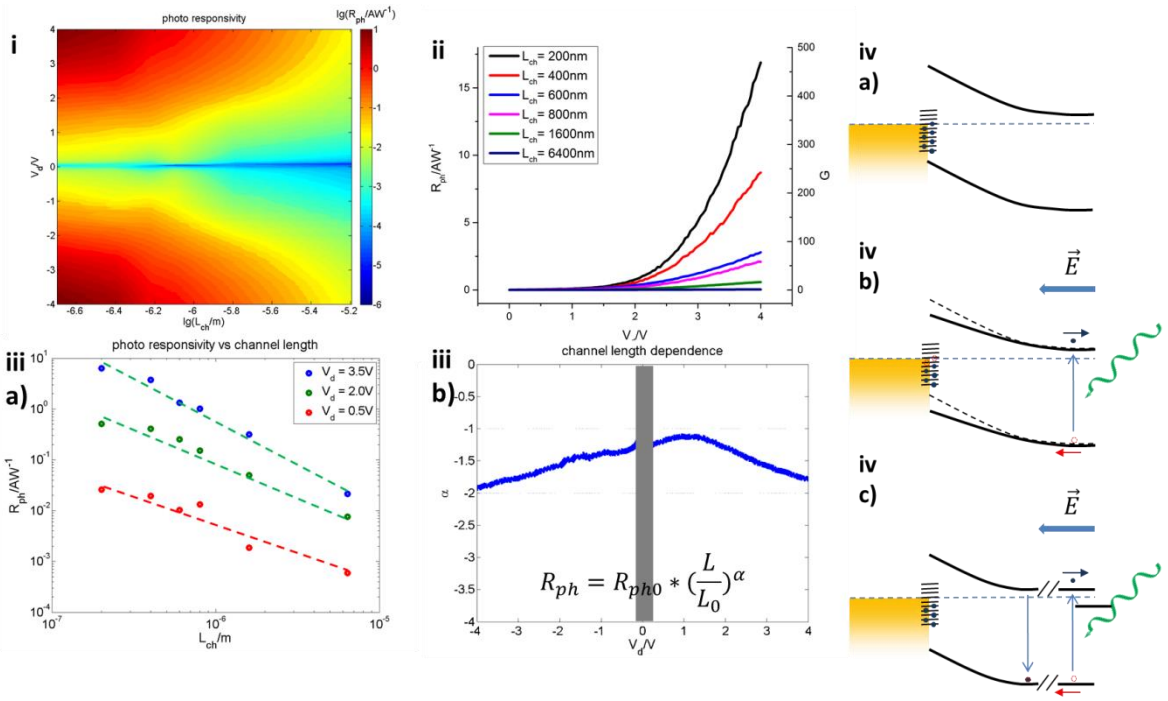


Figure 5-4 Photo responsivity of WS_2 MSM photodetector. (i) map of photo responsivity as a function of channel length and source-drain bias. Colours in the map represent the photo responsivity in 10-based-logristic scale as marked by the colour bar. The photo responsivity are tuned from ~10^{-5} for long channel (L_{ch}=6400nm) photo detectors working under low bias (~0.2V) to ~10^{1} for short channel (L_{ch} = 200nm) photodetector working under mild bias (~4V). (ii) Dependence of photo responsivity (left y axis) and gain (right y axis) on source-drain bias. No current saturation is found for all devices, while gain higher than unity is found commonly. (iii) Dependence of photo responsivity on channel length. (iii,a) Dependence of photo responsivity on channel length with fitting lines. Relation between photo responsivity and channel length follows a power law with the power factor α varies with different source-drain voltage. (iii,b) Dependence of power factor α on source-drain voltage. The α values near zero bias is masked due to noise induces by the small current value. (iv) Band diagram illustrating the photo response mechanism of WS_2 MSM photo detector. (iv,a) Trap states exist at the interface between metal contact and WS_2. The trap states will result a complicated Fermi level pinning effect and influence the effective Schottky barrier height. (iv,b) Photon absorption of the photo detector produces electron-hole pair. Holes are later trapped in the interface between metal contact and semiconductor, which decreases effective Schottky barrier height. The dashed lines indicate the origin position of the conduction and valence band while the solid lines are the actual position conduction and valence band after Fermi level lowering. (iv,c) When the channel length is comparable with the transient length of photo-induced electrons, recombination between electron and hole become significant.

Photo-responsivity and gain are two correlated features of merit for photodetectors. Photo-responsivity measures the sensitivity of photodetector to incident light, which is defined as $R_{ph} = \frac{I_{ph}}{\Phi A}$, where R_{ph} is the photo-responsivity, I_{ph} is the photo current, Φ is the light intensity and A is the detection area. The photoresponsivity of our WS_2 MSM photodetectors was found to be a function of both bias and channel length as shown in Figure 5-4 (i). The photo-responsivity reaches up to 20A/W in for short channel lengths (200nm) and large source-drain bias (4V) (Figure 5-4 (ii)). Further increasing the bias above 4V will lead to higher photo-responsivities, but in current induced degradation of WS_2 start to be significant in our experiments. WS_2 is quickly "burnt" away under bias higher than 5V and no longer conductive. In this way, we set the upper limit of bias to devices as 4V for good consistency and reproducibility. The photo-responsivity is till now the most important value for 2D photo detectors. Slightly smaller photo-responsivity has been reported in Au-MoS_2-Au photodetectors under similar illumination intensity[16]. We note that the illumination intensity (10^2W/m^2-10^6W/m^2) in our experiment is much stronger than the intensity of light (10^{-3}W/m^2-10^2W/m^2) in some other reports. This would lead to an apparent smaller measured photo-responsivity due to the negative dependence of photo-responsivity on illumination intensity.[26]

The gain factor of a photo detector is defined as the number of charge carriers flowing through the circuit per photo-generated electron-hole pair[43] and calculated by

$G = \frac{h\nu}{e\eta} R_{ph}$, where G is the gain, R_{ph} is photo responsivity, h is plank constant, ν is the frequency of photon, e is the absolute value of electron charge, and η is the light absorption rate. By assuming an absorption rate of 8% for monolayer WS_2,[19] gain factor is calculated and plotted in Figure 5-4 (ii). The gain factor reaches about 480, which is comparable to conventional GaAs MSM photo detectors[44] [45] [46] and to organic photo detectors[47].

The gain factor (and thus photo-responsivity) exponentially depends on the source-drain bias (Figure 5-4 (ii)) due to the exponential dependence of emission current overcoming the Schottky barrier. Double logarithm plot of photo-responsivity vs channel length (Figure 5-4 (iii)) reveals a power-law dependence of photo-responsivity on channel length. The power factor varies from $\alpha = -2$, for high bias (4V) to $\alpha = -1$ for low bias as shown in Figure 5-4 (iii,b). Under high bias, the current is limited by the internal resistance of materials. A simple theory involving the trap states is proposed to explain our observation.

We start our analysis form considering the device working under high field (large bias, short channel) and low field (small bias, long channel) condition. Under the high bias condition, the current is limited by the initial resistance of the device. Although the density of photo-generated electron hole pair is almost a fixed value, the gain changes with channel length according to the following formula[43].

$$G = \frac{\mu_e + \mu_h}{\mu_e} \cdot \frac{\tau}{t_t} \qquad \text{eq. 5-5}$$

$$t_t = \frac{L_{ch}^2}{\mu_e V} \qquad \text{eq. 5-6}$$

In eq. 5-5 and eq. 5-6, G is the gain factor of the photo detector, μ_e and μ_h are the electron and hole mobility respectively, τ is the recombination life time, t_t is the transit time, which is the time for an electron to travel from one electrode to another, L_{ch} is the channel length, and V is the source-drain bias. From equation eq. 5-5 and eq. 5-6, it is clear that $G \propto L^{-2}$ (thus $R \propto G \propto L^{-2}$). On the other hand, if the source-drain bias is comparable or smaller than the effective Schottky barrier height, the flat-band condition is not reachable and thus most voltage drops within the dipole layer between the WS_2 and gold contact. In this way, only electron-hole pairs that are generated within the depletion zone contribute to the photocurrent.[48] Photocurrent is independent to channel length in that regime, which leads to the photo-responsivity reciprocally depending on channel length (e.g. red line in Figure 4 (iii, a) and low bias region in Figure 5-4 (iii, b)). By taking our experimental data at high source-drain voltage into equation eq. 5-5 and eq. 5-6 and assuming that holes are trapped (i.e. $\mu_h \ll \mu_e$), we estimate the recombination life time to be around 7ns, which fits well with theoretical prediction of radiative life time in monolayer WS_2 at ambient condition.[49]

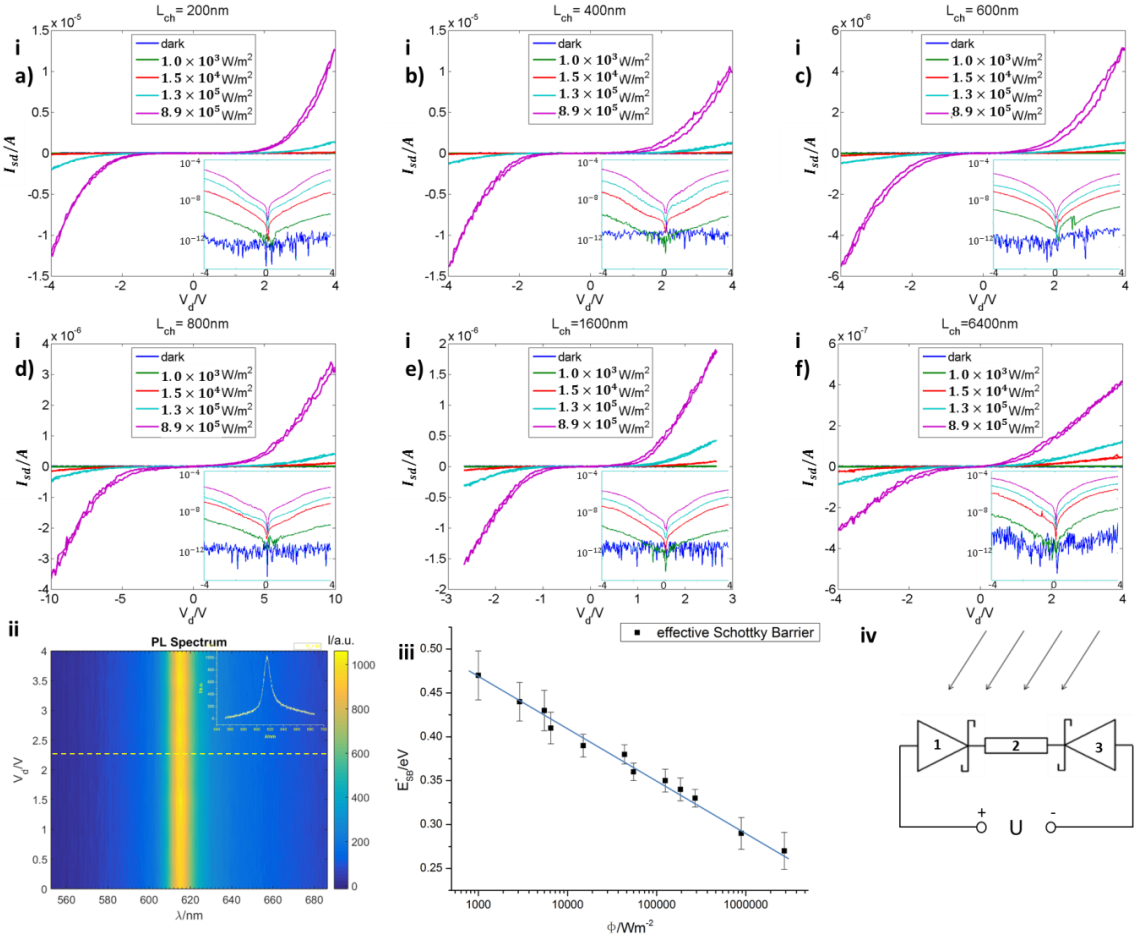


Figure 5-5. (i) a)-f) Photoconductivity of WS_2 photodetectors for different channel lengths (200nm, 400nm, 600nm, 800nm, 1600nm and 6400nm). The insertions are IV plots in logarithmic scale.[50] (ii) PL spectrum of devices under different bias. Typical PL spectrum is shown as the insert that is taken at 2V bias (indicated by the yellow dashed line). (iii) Scatter plot of effective Schottky barrier height (E_{SB}) as a function of light intensity (Φ). The blue line is a fitting curve showing the linear dependence of effective Schottky barrier on logarithm of light intensity. (iv) Equivalent circuit diagram for a MSM photodetector. The MSM photodetector consists of a pair of back-to-back Schottky diodes (device 1, 3) and a series resistor (device 2).

To further clarify the photo-response mechanisms for the Au-WS_2-Au MSM photodetector, the output character is carefully studied. Non-linear IV curves appear as the output character of all devices. Typical IV curves of devices with various channel lengths are shown in Figure 5-5 (i) a)-f). These non-linear IV curves indicate

the formation of a Schottky barrier[51] [52], which is desirable in MSM photo detector. We model the output character as an electrical circuit consisting of two Schottky diodes contacted back-to-back with a series resistance in the middle (insert of Figure 5-5 (1), a)-f)). For small source-drain bias, the reverse-biased diode limits the current flow through the circuit. When increasing the bias, leakage through the reverse-biased diode becomes significant and current flows through the circuit with an exponential increase. Several mechanisms, e.g. increasing of field emission[53], minority carrier injection[54] or avalanche break-down of the channel material[54], may result in similar non-linear IV curves in the set of back-to-back diodes in Figure 5-5 (i). We now discuss the influence of these factors to the photo current as well as gain factor based on our experimental observation.

Avalanche break-down is reported in 2D avalanche photodetectors[55], but is unlikely to occur in our experimental conditions. The electric field should strongly alter the PL spectrum[56] when avalanche break-down happens. However, the PL spectra remains almost unchanged in our experiments as shown in Figure 5-5 (ii). In addition, when avalanche break-down occurs, the kinetic energy of charge carriers is approximately equal to the band gap[57] [58]. We can roughly estimate the kinetic energy by $E_k \sim \frac{1}{2} m^* \left(\frac{\mu V_{sd}}{L_{ch}}\right)^2$, where E_k is the kinetic energy, m* is the effective mass, μ is the mobility, V_{sd} is the source-drain bias, L_{ch} is the channel length.[58] Even though the kinetic energy estimated in this way (~1meV) is generally larger than the real kinetic energy, it is still three orders of magnitude smaller than the band gap of WS_2 (~2eV).

By ruling out avalanche break-down, the output character of the device is described with a modified theory for thermionic emission current through Schottky barrier. The contribution of other transport mechanisms (field emission and minority carrier injection) is considered by adding a phenomenological ideality factor[59]. In this way, we model the current flowing through the back-to-back Schottky diode pair as a series resistance as in Figure 5-5 (iv). We have the following set of equations[60 61]:

$$I = I_0 \exp\left(-\left(1-\frac{1}{n}\right) e\beta V_1\right)(\exp(e\beta V_1) - 1) \qquad \text{eq. 5-7}$$

$$I = \frac{V_2}{R} \qquad \text{eq. 5-8}$$

$$I = -I_0 \exp\left(\left(1-\frac{1}{n}\right) e\beta V_3\right)(\exp(-e\beta V_3) - 1) \qquad \text{eq. 5-9}$$

$$U = V_1 + V_2 + V_3 \qquad \text{eq. 5-10}$$

From eq. 5-7 to eq. 5-10, I is the source-drain current, U is the source-drain bias, I_0 is a constant determined by the Schottky barrier height, n is the ideality factor, e is the absolute value of single electron charge, $\beta = \frac{1}{k_B T}$ is the Boltzmann factor, and V_i (i = 1, 2, 3) are the voltage drop across device 1 (diode on the left), 2 (resistor in the middle) and 3 (diode on the right) in Figure 5-5 (iv) respectively. By solving equations from eq. 5-7 to eq. 5-10, we get the relation between transport current and source-drain bias:

$$I = I_0\left[\frac{\cosh\left(\frac{1}{2}\left(1-\frac{1}{n}\right)e\beta(U-IR)\right)}{\cosh\left(\frac{1}{2n}e\beta(U-IR)\right)}\right]^{-\left(1-\frac{1}{n}\right)} \cdot \frac{\sinh\left(\frac{1}{2}e\beta(U-IR)\right)}{\cosh\left(\frac{1}{2n}e\beta(U-IR)\right)} \quad \text{eq. 5-11}$$

Notations in the equation eq. 5-11 share the same meaning as in equations from eq. 5-7 to eq. 5-10. By fitting the measured IV curve with the equation eq. 5-11, can we extract the pre-factor I_0, internal resistance R and ideality factor n. Especially, I_0 is determined by the Schottky barrier height of the 1D junction between metal contact and 2D WS2[62 63].

$$I_0 = wA_{2D}^{*}T^{3/2}\exp(-\beta e\phi_{\mathrm{SB}}^{*}) \quad \text{eq. 5-12}$$

Where in equation eq. 5-12, w is the contact width, A^* is the effective 2D Richardson constant, T is temperature, $\beta = \frac{1}{k_B T}$ is the Boltzmann factor, and ϕ_{SB}^{*} is the effective Schottky barrier height. By taking the fitting parameter I_0 into equation eq. 5-12, we can calculate the effective Schottky barrier height in the WS_2 MSM photo detector, which is plotted in Figure 5-5 (iii).

Both the ideality factor and the Schottky barrier height are extracted by fitting the experimental data to formulas above. The ideality factor is around 1.03±0.01, which is near unity and thus indicates ideal Schottky junctions are formed between WS_2 and the gold contact. This value is consistence with common diodes and transistors. It is notable that the effective barrier depends negatively on the incident light intensity, but has no correlation with the channel length down to 200nm in our experiment. This

suggests a very narrow depletion zone in our device, which is likely due to an abundancy of trap states in the interface between electrode and WS_2.

The lowering of the effective Schottky barrier height can be understood as a result of accumulating trapped charge at the interface between the metal contact and semiconductor.[49] The hysteresis in Figure 5-5 (i) is due to the charge and discharge process of trap states in the interface between electrode and WS_2. Incident light can generate electron-hole pairs, which are separated by the external electric field. Although electrons can easily drift to and enter the positive electrode (anode), holes are trapped in the interface between the negative electrode (cathode) and semiconductor, especially if there is an abundancy of trap states. The semiconductor is then going to be positively charged around the cathode due to the accumulation of holes. These charges in turn lower the local Fermi level of WS_2, which further decreases the Schottky barrier height. Such a mechanism is schematically plotted in Figure 5-5 (iv,b). Similar photo induced trapped charge accumulation is reported in graphene-MoS_2 interfaces acting as a photo gate[64]. When reaching equilibrium, the Schottky barrier height decreases to such a level that electrons can be injected into the WS_2 by thermionic emission and the holes no longer accumulate near the positive electrode. Similar mechanisms have successfully explained the gain in GaAs MSM photodetectors[44 45 46].

Conclusion

We have revealed that filling trap states at the interface between gold contacts and WS_2 leads to a lowering of effective Schottky barrier height, enabling current injection from the electrodes to dominate. A large gain factor (as high as 480) and small dark current (smaller than 10pA) is realized with mild bias (4V) without any gate for small channel length devices (200nm). Channel length dependence shows that smaller channels give higher photoconductivity and future devices should utilize this advantage to eliminate series resistance effects of the central WS_2 region that has limited role in contributing to the photocurrent activation mechanism. Photo sensing unit with smaller channel length can further lead to a higher packing density in one chip, which will provide better resolution. The large area growth of WS_2 monolayers enabled arrays of photodetectors to be fabricated and opens up the opportunity to produce 2D imaging sensors.

Reference

(1) Fan, Y.; Zhou, Y.; Wang, X.; Tan, H.; Rong, Y.; Warner, J. H. Photoinduced Schottky Barrier Lowering in 2D Monolayer WS 2 Photodetectors. *Adv. Opt. Mater.* **2016**.

(2) Koppens, F. H. L.; Mueller, T.; Avouris, P.; Ferrari, A. C.; Vitiello, M. S.; Polini, M. Photodetectors Based on Graphene, Other Two-Dimensional Materials and Hybrid Systems. *Nat. Nanotechnol.* **2014**, *9*, 780–793.

(3) Wang, Q. H.; Kalantar-Zadeh, K.; Kis, A.; Coleman, J. N.; Strano, M. S. Electronics and Optoelectronics of Two-Dimensional Transition Metal Dichalcogenides. *Nat. Nanotechnol.* **2012**, *7*, 699–712.

(4) Chen, S.; Brown, L.; Levendorf, M.; Cai, W.; Ju, S.-Y.; Edgeworth, J.; Li, X.; Magnuson, C. W.; Velamakanni, A.; Piner, R. D.; Kang, J.; Park, J.; Ruoff, R. S. Oxidation Resistance of Graphene-Coated Cu and Cu/Ni Alloy. *ACS Nano* **2011**, *5*, 1321–1327.

(5) Morozov, S. V.; Novoselov, K. S.; Katsnelson, M. I.; Schedin, F.; Elias, D. C.; Jaszczak, J. A.; Geim, A. K. Giant Intrinsic Carrier Mobilities in Graphene and Its Bilayer. *Phys. Rev. Lett.* **2008**, *100*, 16602.

(6) Dean, C. R.; Young, a F.; Meric, I.; Lee, C.; Wang, L.; Sorgenfrei, S.; Watanabe, K.; Taniguchi, T.; Kim, P.; Shepard, K. L.; Hone, J. Boron Nitride Substrates for High-Quality Graphene Electronics. *Nat. Nanotechnol.* **2010**, *5*, 722–726.

(7) Petrone, N.; Dean, C. R.; Meric, I.; van der Zande, A. M.; Huang, P. Y.; Wang, L.; Muller, D.; Shepard, K. L.; Hone, J. Chemical Vapor Deposition-Derived Graphene with Electrical Performance of Exfoliated Graphene. *Nano Lett.* **2012**, *12*, 2751–2756.

(8) Lee, C.; Wei, X.; Kysar, J. W.; Hone, J.; =. Measurement of the Elastic Properties and Intrinsic Strength of Monolayer Graphene. *Science* **2008**, *321*, 385–388.

(9) Geim, A. K.; Novoselov, K. S. The Rise of Graphene. *Nat. Mater.* **2007**, *6*, 183–191.

(10) Bonaccorso, F.; Sun, Z.; Hasan, T.; Ferrari, a. C. Graphene Photonics and Optoelectronics. *Nat. Photonics* **2010**, *4*, 611–622.

(11) Zhang, Y.; Zhang, Y.; Ji, Q.; Ju, J.; Yuan, H.; Shi, J.; Gao, T.; Ma, D.; Liu, M.; Chen, Y.; Song, X.; Hwang, H. Y.; Cui, Y.; Liu, Z. Controlled Growth of High-Quality Monolayer WS2 Layers on Sapphire. *ACS Nano* **2013**, *7*, 8963–8971.

(12) Lee, Y. H.; Zhang, X. Q.; Zhang, W.; Chang, M. T.; Lin, C. Te; Chang, K. Di; Yu, Y. C.; Wang, J. T. W.; Chang, C. S.; Li, L. J.; Lin, T. W. Synthesis of Large-Area MoS2 Atomic Layers with Chemical Vapor Deposition. *Adv. Mater.* **2012**, *24*, 2320–2325.

(13) Zhou, H.; Wang, C.; Shaw, J. C.; Cheng, R.; Chen, Y.; Huang, X.; Liu, Y.; Weiss, N. O.; Lin, Z.; Huang, Y.; Duan, X. Large Area Growth and Electrical Properties of P-Type WSe 2 Atomic Layers. *Nano Lett.* **2015**, *15*, 709–713.

(14) Shi, Y.; Li, H.; Li, L. Recent Advances in Controlled Synthesis of Two-Dimensional Transition Metal Dichalcogenides via Vapour Deposition Techniques. *Chem. Soc. Rev.* **2015**, *44*, 2744–2756.

(15) Favron, A.; Gaufrès, E.; Fossard, F.; Phaneuf-L'Heureux, A.-L.; Tang, N. Y.-W.; Lévesque, P. L.; Loiseau, A.; Leonelli, R.; Francoeur, S.; Martel, R. Photooxidation and Quantum Confinement Effects in Exfoliated Black

Phosphorus. *Nat. Mater.* **2015**, *14*, 826–832.

(16) Tsai, D. S.; Liu, K. K.; Lien, D. H.; Tsai, M. L.; Kang, C. F.; Lin, C. A.; Li, L. J.; He, J. H. Few-Layer MoS2 with High Broadband Photogain and Fast Optical Switching for Use in Harsh Environments. *ACS Nano* **2013**, *7*, 3905–3911.

(17) Britnell, L.; Ribeiro, R. M.; Eckmann, A.; Jalil, R.; Belle, B. D.; Mishchenko, A.; Kim, Y.-J.; Gorbachev, R. V; Georgiou, T.; Morozov, S. V; Grigorenko, a N.; Geim, a K.; Casiraghi, C.; Neto, A. H. C.; Novoselov, K. S. Strong Light-Matter Interactions in Heterostructures of Atomically Thin Films. *Science.* **2013**, *340*, 1311–1314.

(18) Yu, W. J.; Liu, Y.; Zhou, H.; Yin, A.; Li, Z.; Huang, Y.; Duan, X. Highly Efficient Gate-Tunable Photocurrent Generation in Vertical Heterostructures of Layered Materials. *Nat. Nanotechnol.* **2013**, *8*, 952–958.

(19) Bernardi, M.; Palummo, M.; Grossman, J. C. Extraordinary Sunlight Absorption and One Nanometer Thick Photovoltaics Using Two-Dimensional Monolayer Materials. *Nano Lett.* **2013**, *13*, 3664–3670.

(20) Konstantatos, G.; Badioli, M.; Gaudreau, L.; Osmond, J.; Bernechea, M.; de Arquer, F. P. G.; Gatti, F.; Koppens, F. H. L. Hybrid Graphene–quantum Dot Phototransistors with Ultrahigh Gain. *Nat. Nanotechnol.* **2012**, *7*, 363–368.

(21) Mueller, T.; Xia, F.; Avouris, P. Graphene Photodetectors for High-Speed Optical Communications. *Nat. Photonics* **2010**, *4*, 297–301.

(22) Xia, F.; Mueller, T.; Lin, Y.-M.; Valdes-Garcia, A.; Avouris, P. Ultrafast Graphene Photodetector. *Nat. Nanotechnol.* **2009**, *4*, 839–843.

(23) Lopez-Sanchez, O.; Lembke, D.; Kayci, M.; Radenovic, A.; Kis, A. Ultrasensitive Photodetectors Based on Monolayer MoS2. *Nat. Nanotechnol.* **2013**, *8*, 497–501.

(24) Huo, N.; Yang, S.; Wei, Z.; Li, S.-S.; Xia, J.-B.; Li, J. Photoresponsive and Gas Sensing Field-Effect Transistors Based on Multilayer WS2 Nanoflakes. *Sci. Rep.* **2014**, *4*, 5209.

(25) Lan, C.; Li, C.; Yin, Y.; Liu, Y. Large-Area Synthesis of Monolayer WS2 and Its Ambient-Sensitive Photo-Detecting Performance. *Nanoscale* **2015**, *7*, 5974–5980.

(26) Perea-López, N.; Elías, A. L.; Berkdemir, A.; Castro-Beltran, A.; Gutiérrez, H. R.; Feng, S.; Lv, R.; Hayashi, T.; López-Urías, F.; Ghosh, S.; Muchharla, B.; Talapatra, S.; Terrones, H.; Terrones, M. Photosensor Device Based on Few-Layered WS2 Films. *Adv. Funct. Mater.* **2013**, *23*, 5511–5517.

(27) Choi, W.; Cho, M. Y.; Konar, A.; Lee, J. H.; Cha, G. B.; Hong, S. C.; Kim, S.; Kim, J.; Jena, D.; Joo, J.; Kim, S. High-Detectivity Multilayer MoS2 Phototransistors with Spectral Response from Ultraviolet to Infrared. *Adv. Mater.* **2012**, *24*, 5832–5836.

(28) Zhang, W.; Huang, J. K.; Chen, C. H.; Chang, Y. H.; Cheng, Y. J.; Li, L. J. High-Gain Phototransistors Based on a CVD MoS2 Monolayer. *Adv. Mater.*

2013, *25*, 3456–3461.

(29) Berger, P. R. MSM Photodiodes. *IEEE Potentials* **1996**, *15*, 25–29.

(30) Cowley, a. M.; Sze, S. M. Surface States and Barrier Height of Metal-Semiconductor Systems. *J. Appl. Phys.* **1965**, *36*, 3212–3220.

(31) Rong, Y.; Fan, Y.; Leen Koh, A.; Robertson, A. W.; He, K.; Wang, S.; Tan, H.; Sinclair, R.; Warner, J. H. Controlling Sulphur Precursor Addition for Large Single Crystal Domains of WS2. *Nanoscale* **2014**, *6*, 12096–12103.

(32) Gutierrez, H. R.; Perea-Lopez, N.; Elias, A. L.; Berkdemir, A.; Wang, B.; Lv, R.; Lopez-Urias, F.; Crespi, V. H.; Terrones, H.; Terrones, M. Extraordinary Room-Temperature Photoluminescence in Triangular WS2 Monolayers. *Nano Lett.* **2013**, *13*, 3447–3454.

(33) Berkdemir, A.; Gutiérrez, H. R.; Botello-Méndez, A. R.; Perea-López, N.; Elías, A. L.; Chia, C.-I.; Wang, B.; Crespi, V. H.; López-Urías, F.; Charlier, J.-C.; Terrones, H.; Terrones, M. Identification of Individual and Few Layers of WS2 Using Raman Spectroscopy. *Sci. Rep.* **2013**, *3*, 1755.

(34) Peimyoo, N.; Yang, W.; Shang, J.; Shen, X.; Wang, Y.; Yu, T. Chemically Driven Tunable Light Emission of Charged and Neutral Excitons in Monolayer WS2. *ACS Nano* **2014**, *8*, 11320–11329.

(35) Mouri, S.; Miyauchi, Y.; Matsuda, K. Tunable Photoluminescence of Monolayer MoS2 via Chemical Doping. *Nano Lett.* **2013**, *13*, 5944–5948.

(36) Xu, Z.; Zhang, Y.; Lin, S.; Zheng, C.; Zhong, Y. L.; Xia, X.; Li, Z.; Sophia, P. J.;

Fuhrer, M. S.; Cheng, Y.; Bao, Q. Synthesis and Transfer of Large-Area Monolayer WS2 Crystals : Moving Toward the Recyclable Use of Sapphire Substrates Synthesis and Transfer of Large-Area Monolayer WS 2 Crystals : Moving Toward the Recyclable Use of Sapphire Substrates. **2015**, 6178–6187.

(37) Kobayashi, Y.; Sasaki, S.; Mori, S.; Hibino, H.; Liu, Z.; Watanabe, K.; Taniguchi, T.; Suenaga, K.; Maniwa, Y.; Miyata, Y. Growth and Optical Properties of High-Quality Monolayer WS2 on Graphite. *ACS Nano* **2015**, *9*, 4056–4063.

(38) Ovchinnikov, D.; Allain, A.; Huang, Y.; Dumcenco, D.; Kis, A. Electrical Transport Properties of Single-Layer WS2. *ACS Nano* **2014**, *8*, 8174–8181.

(39) Najam, F.; Tan, M. L. P.; Ismail, R.; Seop Yu, Y. Two-Dimensional (2D) Transition Metal Dichalcogenide Semiconductor Field-Effect Transistors: The Interface Trap Density Extraction and Compact Model. *Semicond. Sci. Technol.* **2015**, *30*, 75010.

(40) Louie, S. G.; Chelikowsky, J. R.; Cohen, M. L. Ionicity and the Theory of Schottky Barriers. *Phys. Rev. B* **1977**, *15*, 2154–2162.

(41) Ghatak, S.; Pal, A. N.; Ghosh, A. Nature of Electronic States in Atomically Thin MoS2 Field-Effect Transistors. *ACS Nano* **2011**, *5*, 7707–7712.

(42) Cao, Y.; Cai, K.; Hu, P.; Zhao, L.; Yan, T.; Luo, W.; Zhang, X.; Wu, X.; Wang, K.; Zheng, H. Strong Enhancement of Photoresponsivity with Shrinking the Electrodes Spacing in Few Layer GaSe Photodetectors. *Sci. Rep.* **2015**, *5*, 8130.

(43) Saleh, B. E. A.; Teich, M. C. Chapter 17: Semiconductor Photon Detectors. In *Fundamentals of Photonics*; Wiley Series in Pure and Applied Optics; John Wiley & Sons, Inc.: New York, USA, 1991.

(44) Sugeta, T.; Urisu, T.; Sakata, S.; Mizushima, Y. Metal-Semiconductor-Metal Photodetector for High-Speed Optoelectronic Circuits. *Jpn. J. Appl. Phys.* **1980**, *19*, 459.

(45) Su, Y. K.; Chang, S. J.; Chen, C. H.; Chen, J. F.; Chi, G. C.; Sheu, J. K.; Lai, W. C.; Tsai, J. M. GaN Metal-Semiconductor-Metal Ultraviolet Sensors with Various Contact Electrodes. *IEEE Sens. J.* **2002**, *2*, 366–371.

(46) Katz, O.; Garber, V.; Meyler, B.; Bahir, G.; Salzman, J. Gain Mechanism in GaN Schottky Ultraviolet Detectors. *Appl. Phys. Lett.* **2001**, *79*, 1417.

(47) Zhang, H.; Jenatsch, S.; De Jonghe, J.; Nüesch, F.; Steim, R.; Véron, A. C.; Hany, R. Transparent Organic Photodetector Using a Near-Infrared Absorbing Cyanine Dye. *Sci. Rep.* **2015**, *5*, 9439.

(48) Wu, C. C.; Jariwala, D.; Sangwan, V. K.; Marks, T. J.; Hersam, M. C.; Lauhon, L. J. Elucidating the Photoresponse of Ultrathin MoS2 Field-Effect Transistors by Scanning Photocurrent Microscopy. *J. Phys. Chem. Lett.* **2013**, *4*, 2508–2513.

(49) Palummo, M.; Bernardi, M.; Grossman, J. C.; Grossman, C. Exciton Radiative Lifetimes in Two-Dimensional Transition Metal Dichalcogenides. *Nano Lett.* **2015**, *15*, 2794–2800.

(50) Sawa, A.; Fujii, T.; Kawasaki, M.; Tokura, Y. Hysteretic Current-Voltage Characteristics and Resistance Switching at a Rectifying Ti/Pr0.7Ca0.3MnO3 Interface. *Appl. Phys. Lett.* **2004**, *85*, 4073–4075.

(51) Chen, J.; Odenthal, P. M.; Swartz, A. G.; Floyd, G. C.; Wen, H.; Luo, K. Y.; Kawakami, R. K. Control of Schottky Barriers in Single Layer MoS2 Transistors with Ferromagnetic Contacts. *Nano Lett.* **2013**, *13*, 3106–3110.

(52) Tans, S.; Verschueren, A.; Dekker, C. Room-Temperature Transistor Based on a Single Carbon Nanotube. *Nature* **1998**, *672*, 669–672.

(53) F.A.Padovani; R.Stratton. Field and Thermionic-Field Emission in Schottky Barriers. *Solid. State. Electron.* **1966**, *9*, 695–707.

(54) Sze, S. M.; Coleman, D. J.; Loya, a. Current Transport in Metal-Semiconductor-Metal (MSM) Structures. *Solid. State. Electron.* **1971**, *14*, 1209–1218.

(55) Lei, S.; Wen, F.; Ge, L.; Najmaei, S.; George, A.; Gong, Y.; Gao, W.; Jin, Z.; Li, B.; Lou, J.; Kono, J.; Vajtai, R.; Ajayan, P.; Halas, N. J. An Atomically Layered InSe Avalanche Photodetector. *Nano Lett.* **2015**, *15*, 3048–3055.

(56) Tasch, S.; Kranzelbinder, G.; Leising, G.; Scherf, U. Electric-Field-Induced Luminescence Quenching in an Electroluminescent Organic Semiconductor. *Phys. Rev. B* **1997**, *55*, 5079–5083.

(57) S.O. Kasap. Chapter 5: Photodetectors and Image Sensors. In *Optoelectronics and photonics :principles and practices*; Gilfillan, A.; Dworkin, A., Eds.;

Pearson Education, Inc., 2012.

(58) Hodgkinson, R. J. Impact Ionization Threshold in Semiconductors. *Proc. Phys. Soc.* **1963**, *82*, 1010–1019.

(59) Rhoderick, E. H. Metal-Semiconductor Contacts. *IEE Proc. I Solid State Electron Devices* **1982**, *129*, 1.

(60) Chiquito, A. J.; Amorim, C. a; Berengue, O. M.; Araujo, L. S.; Bernardo, E. P.; Leite, E. R. Back-to-Back Schottky Diodes: The Generalization of the Diode Theory in Analysis and Extraction of Electrical Parameters of Nanodevices. *J. Phys. Condens. Matter* **2012**, *24*, 225303.

(61) Ohta, Y.; Kubozono, Y.; Fujiwara, A. Transport Properties in C60 Field-Effect Transistor with a Single Schottky Barrier. *Appl. Phys. Lett.* **2008**, *92*, 173306.

(62) Chen, J. *et al.* Effects of Electron Confinement on Thermionic Emission Current in a Modulation Doped Heterostructure. *Solid. State. Electron.* **2013**, *24*, 695–707.

(63) Liu, W.; Sarkar, D.; Kang, J.; Cao, W.; Banerjee, K. Impact of Contact on the Operation and Performance of Back-Gated Monolayer MoS 2 Field-Effect-Transistors. *ACS Nano* **2015**, *9*, 7904–7912.

(64) Zhang, W.; Chuu, C.-P.; Huang, J.-K.; Chen, C.-H.; Tsai, M.-L.; Chang, Y.-H.; Liang, C.-T.; Chen, Y.-Z.; Chueh, Y.-L.; He, J.-H.; Chou, M.-Y.; Li, L.-J. Ultrahigh-Gain Photodetectors Based on Atomically Thin Graphene-MoS2 Heterostructures. *Sci. Rep.* **2014**, *4*, 1–8.

6

2D *In-situ* Electronics in TEM

Contents

6.1 Introduction 182

6.2 Electric Breakdown of WS_2/Amorphous-Carbon Film 183

6.2.1 Introduction 183

6.2.2 Device fabrication and materials characterization 186

6.2.3 Experiments, results and discussions 188

6.3 Negative Electro-Conductance of WS_2 Nano-Device 200

6.3.1 Introduction 200

6.3.2 Device Fabrication and Materials Characterization 202

6.3.3 Experimental results and discussion 206

Reference 213

* Section 6.2 of this chapter is modified from draft ready for publication.

**Section 6.3 of this chapter is modified from reference[1].

*** Works presented in this chapter is in collaboration with Dr. Alex. W. Robertson. Atomic resolved TEM image was taken by Dr. Robertson.

6.1 Introduction

This chapter aims to push the study of 2D electronics into a more precise and determinative level by combining transmission electron microscope with in-situ electronic measurement. A novel in-situ electronic measurement holder is fabricated for that goal. In section 6.2, in-situ electrical breakdown of WS_2 is characterized for the first time. The electric shock provided enables a novel synthesis method of WS_2

nanoparticle decorated graphene film from WS_2/amorphous-carbon film. This result provides a simple yet powerful solution for production of nanoparticle decorated graphene film, which could potentially play an important role in catalytic applications. Session 6.3 of this chapter reports the study on the electron responsivity of suspended WS_2 single crystal. We discover a negative electron-conductivity of WS_2 monolayer. This result paves the road toward 2D direct electron detectors. Studies in this chapter are only a starting point of combining the nano-electronic fabrication of 2D materials with HRTEM, but demonstrate the powerfulness of such measurement system.

6.2 Electric Breakdown of WS_2/Amorphous-Carbon Film

6.2.1 Introduction

Joule annealing under high bias is commonly used pre-treatment of the device before measurement. This method is first applied to 2D materials to get rid of surface contaminations on graphene,[2] but soon finds a larger stage to play as a general routine of cleaning for other 2D materials. Joule annealing improves the device performance for several reasons. Early study show that the contact resistance decreases between carbon-nanotube and metal contact after the Joule annealing treatment.[3] This is caused by the thermal enhanced desorption of adsorbates and formation of bonding between carbon nanotube and metal contact. In addition, the current annealing process helps to evaporate the surface contamination. Small molecules like H_2O or O_2 can be expelled from the surface of 2D materials due to the increasing of surface temperature.

Despite many studies heavily relay on the Joule annealing process, very few study is done to characterize the change of amorphous carbon on the surface of 2D materials. Precious study using SEM and AFM show a smoother surface after the annealing process.[2] Although this result indicates a less amount of amorphous carbon on surface, it is not clear whether the amorphous carbon is evaporated away. Other studies show that amorphous carbon on the surface of graphene can graphitize during the joule annealing process.[4] However, it is not clear whether such a process could also happen in other 2D materials film. Hysteresis induced by amorphous carbon in the transfer curve during field effect measurement as well as IV sweep is found in suspended MoS_2.[5] The persistence of such hysteresis after joule annealing in vacuum indicates that the amorphous carbon is unlikely totally removed by Joule annealing method. As a matter of fact, the graphitization of graphene oxide by vacuum annealing[6] or current induced heating[7] is reported previously. More careful studies, however, reveal that the current induced graphitization is not merely a thermal effect but rather more a electrochemical process that can happen at much lower temperature compared with the graphitization caused by thermal annealing.[8 9] Despite of these studies, there is still a lack of microscopic study to directly link the current and the change of materials structure.

Here in this study, we study the Joule annealing effect to WS2/amorphous-carbon film.WS_2 is one of the promising catalyst for dehydrogenation. Pioneering studies on the desulfurization catalytic behaviour of MoS_2 indicate that the edge area is the

major active region of catalyst.[10] Recent study confirms that the edge is also the major reactive sites for the hydrogen evolution reaction catalysed by TMDC materials.[11] Furthermore, it is soon realized that not only the edge but sulphur defects on the surface of TMDC crystal could also catalyse the reaction.[12] These results inspire people to seek WS_2 nanoparticle catalyst, which by nature have a large aspect ratio of edge and reasonable concentration of defects, to increase the catalytic efficiency. Several challenges have been revealed by the intensive studies on the synthesis of WS2 catalyst. First, the production of WS_2 nanoparticle turns out to be hard. Flower-shaped WS_2 nano-sheets on different substrate like graphene oxide[13], carbon cloth[14], or silicon[15] have been synthesized. Typical size of these nano-sheets is of the scale of 10^2nm. In addition, nano-sheets synthesized are generally in the form of few-layer WS_2 film, which lower catalytic efficiency compared with monolayer materials. Recently defects are intentionally introduced by plasma treatment to monolayer MoS_2, which results an improved catalytic acctivity.[16] However, methods to reduce the sheet sized down to the scale of tens or even several nano-metres are still desired. The poor conductivity of WS_2 catalyst, especially when in the form of few layer thick, is another problem for WS_2 catalyst in electrochemical applications. Many efforts on improving the conductivity of WS_2 have been made. Phase transformation of strained WS_2 Nano sheets have shown improved conductivity as well as catalytic property for hydrogen evolution.[17] Another method to improve the conductivity is to load WS_2 on a conductive substrate. Graphene is among the idea substrate that increase the catalytic effect of WS_2.[18] In this way, it would be ideal to

hybrid WS_2 nano-particle on the surface of graphene substrate for the purpose of high catalytic efficiency.

In this study, we report a one-step synthesis of WS_2 nano-particle embedded graphene film by electric shock. Producing nanoparticles with large current shock is reported previously. Si micro-particles are smashed by the electric shock into nano-particles due to the high temperature cause by the current.[19] In our study, amorphous carbon on the surface of WS_2 is successfully transformed into multilayer graphene film. The formation of graphene is in accompanied with electric break-down of WS_2 monolayer and thus results a WS_2 nanoparticle decorated graphene film. The crystal structure and electronic properties of materials produced by the electric shock is characterized with the help of our home-made in-situ electronic measurement holder. Due to the very low input power during the reaction, the temperature of the device remains low. Our discovery is thus lead to an energy efficiency route of synthesis 2D nanoparticle decorated graphene film.

6.2.2 Device fabrication and materials characterization

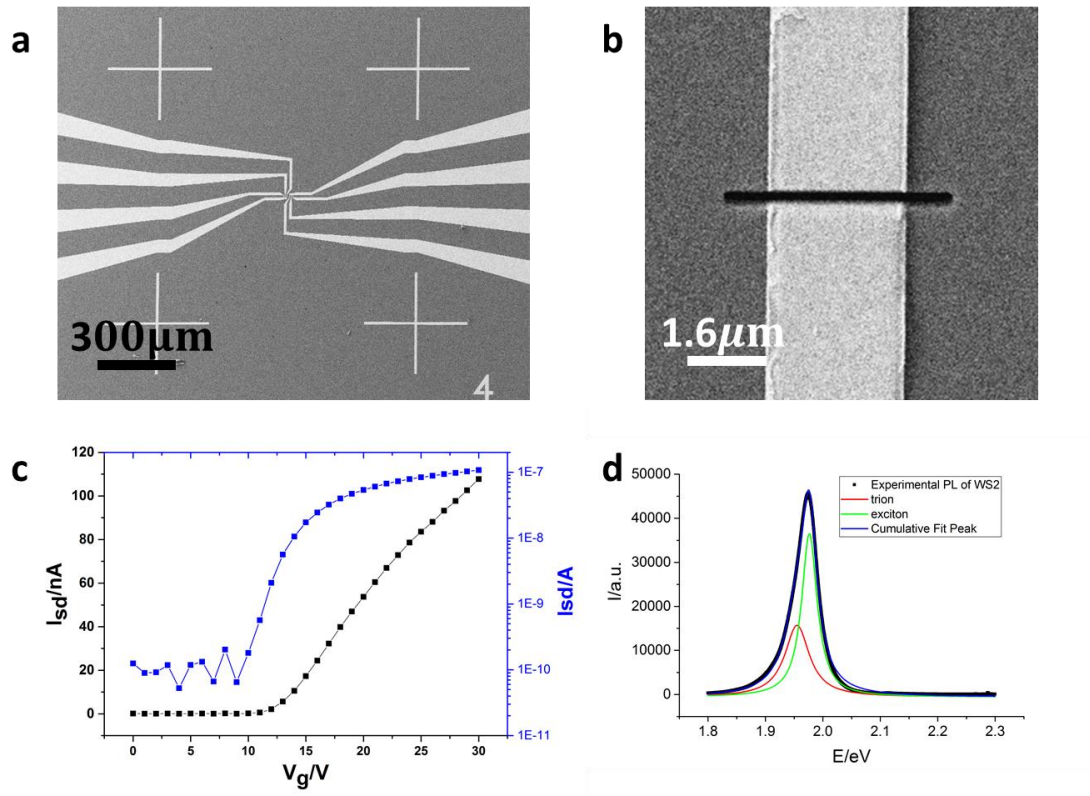


Figure 6-1 Characterization of devices and Materials. (a) SEM image of in-situ electronic TEM grid. (b) High-mag SEM image of electrodes. (c) Transfer curve of the WS2. The black curve is plotted in linear coordinate and the blue curve is plotted in logarithm coordinate. The measurement is done in vacuum (d) Photoluminescence (PL) spectrum of WS_2. The WS_2 is grown in the same recipe as the one transferred onto the in-situ electronic TEM grid, but transferred onto silicon chip for the PL measurement.

Figure 6-1 (a) and (b) is the SEM image of the in-situ electronic grid used in this study. Three devices are measured once in a time. All three devices are co-sourced. A 250nm gap between source and drain electrode is cut by focused ion beam (FIB) milling. The channel length of suspend WS_2 is thus 250nm and the channel width is 2μm. The large ratio between channel width and channel length enables a uniform current flow between the electrodes, the current density of which is simulated in Figure 6-2 (d) under the condition of 1V bias and 1Ω 2D conductivity.

CVD WS_2 is characterized before carrying out the in-situ measurement. Electronic characterization of the materials is carried on field effect transistor (FET) fabricated with the CVD WS_2. The transfer measurement in Figure 6-1 (c) reveals a field effect mobility as $0.8 cm^2 V^{-1} s^{-1}$, and a subthreshold swing as 1.9V/dec. We measure the photo luminescence (PL) of WS_2 used in this experiment. The strong PL spectral intensity is due to the direct band gap, which is characteristic for monolayer TMDC materials. The PL spectrum contains of two major peaks, e.g. the trion and the exciton peak, which are shown in Figure 6-1 (d) as the red and green curves. The significant trion peak indicates the n-doped nature of WS_2, which is typical for CVD grown WS_2.

6.2.3 Experiments, results and discussions

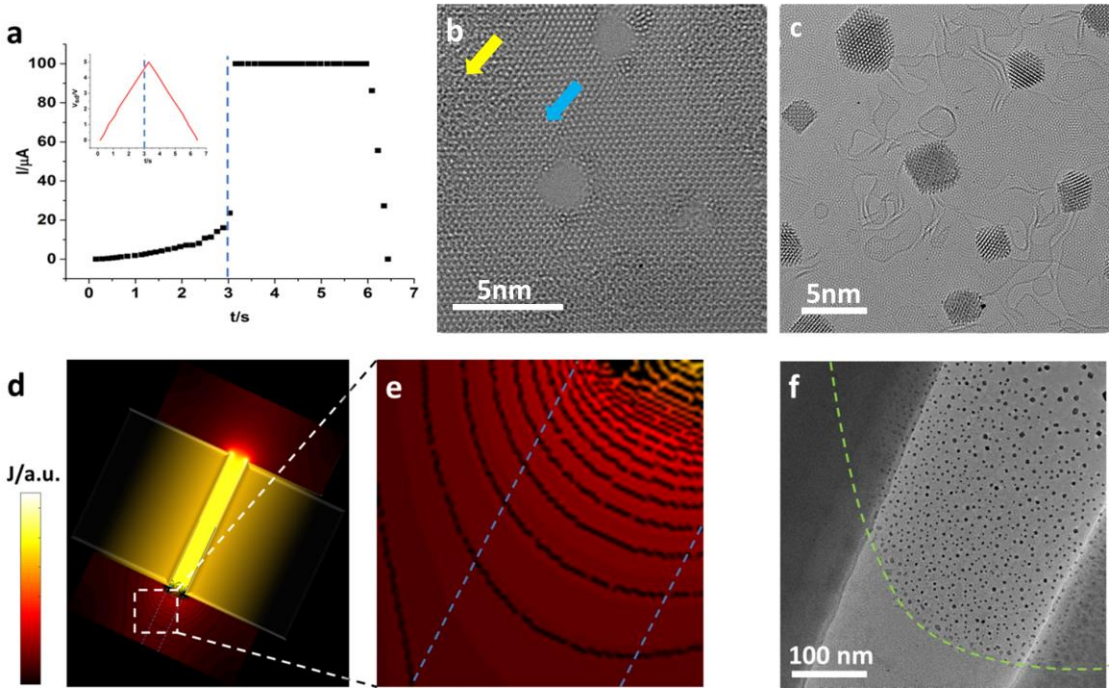


Figure 6-2 Contemporary break-down of WS_2 and formation of graphene. (a) Time resolved current measurement. A sweeping source-drain bias is applied onto the device as the insertion. The WS_2 film breakdown when the source drain bias reaches about 4.5V. (b) HRTEM image of WS_2 film before the electrical break-down. Amorphous carbon adhesion add a noisy background to the atomic image of WS2 as

compared between the region covered by amorphous carbon (pointed by yellow arrow) and region free from amorphous carbon (pointed by blue arrow). (c) HRTEM image of graphene formed after the breakdown of WS_2. Graphene film is decorated with WS_2 nanoparticle. (d) (e) Simulated current density between the source and drain electrodes. (e) is the magnified image from the corner of electrode. Blue dashed line in e marks the edge of silicon nitride. Material between the blue dashed lines is suspended. (f) TEM image of the corner of WS_2 with amorphous carbon after break-down. The green dashed curve marks the edge between graphene and WS_2.

The in-situ electrical measurement is carried out using our home-made in-situ electronic measurement holder. A sweeping source-drain bias is applied to the device. The electron beam is sheltered off from the sample when sample is biased to avoid the influence of incident electron beam.

When high bias applied to the device, WS_2 breaks down in accompany with the formation of multi-layer graphene as shown in Figure 6-2. The break-down of WS_2 with amorphous carbon happens at 4.5V, which corresponds to 18MV/m (channel length 250nm). We notice that the break-down of WS_2 happens very quick once reaches the threshold electric field strength. The transformation happens within 0.15s (Figure 6-2 (a)), which is the minimum measurable time stamp in our experiment set-up. The threshold electric field is comparable with the 10MV/m breakdown electric field for MoS_2.[20] The resistance decreases about two orders of magnitude from 700kΩ to about 6.9kΩ. The better conductivity is due to the formation of graphene as shown in Figure 6-2 (b) and (c). To further understand the role of current in this experiment, we simulate the current density distribution over WS_2 film. Although a uniform current flow right between the two electrodes (Figure 6-2 (d)), the

current density diminishes quickly out of the edge of electrodes (Figure 6-2 (e)). Black curves in Figure 6-2 (e) are the contour lines of the current density. The suspended region is marked by the violet dashed line in Figure 6-2 (e). After the high bias annealing and WS_2 break-down, graphene forms between the electrodes. The contrast of graphene in TEM image is lighter than amorphous carbon covered WS_2 as shown in Figure 6-2 (b), (c) and (f). We notice that the boundary between graphene and amorphous carbon fit well with our simulated contour line of current density as compared in Figure 6-2 (e) and (f). This confirms that the graphitization is caused by current passing through but not factors like electron beam radiation.

Before measuring the crystal information from the TEM data, we calibrated the TEM to link the reported magnification with real magnification. Details of the calibration process are recorded in the methodology session of this thesis. In brief, lattice constant of graphene and WS_2 are used as reference for HRTEM images with different setting magnification. Several images from different crystals are used to avoid systematic bias. The actual magnification for certain setting magnification is determined by the averaged results according to the calibration with different crystals. During the process, we find that the actual magnification varies even with the fixed setting magnification. This determines the uncertainty of our measurement method, which is around 4% of the measured value.

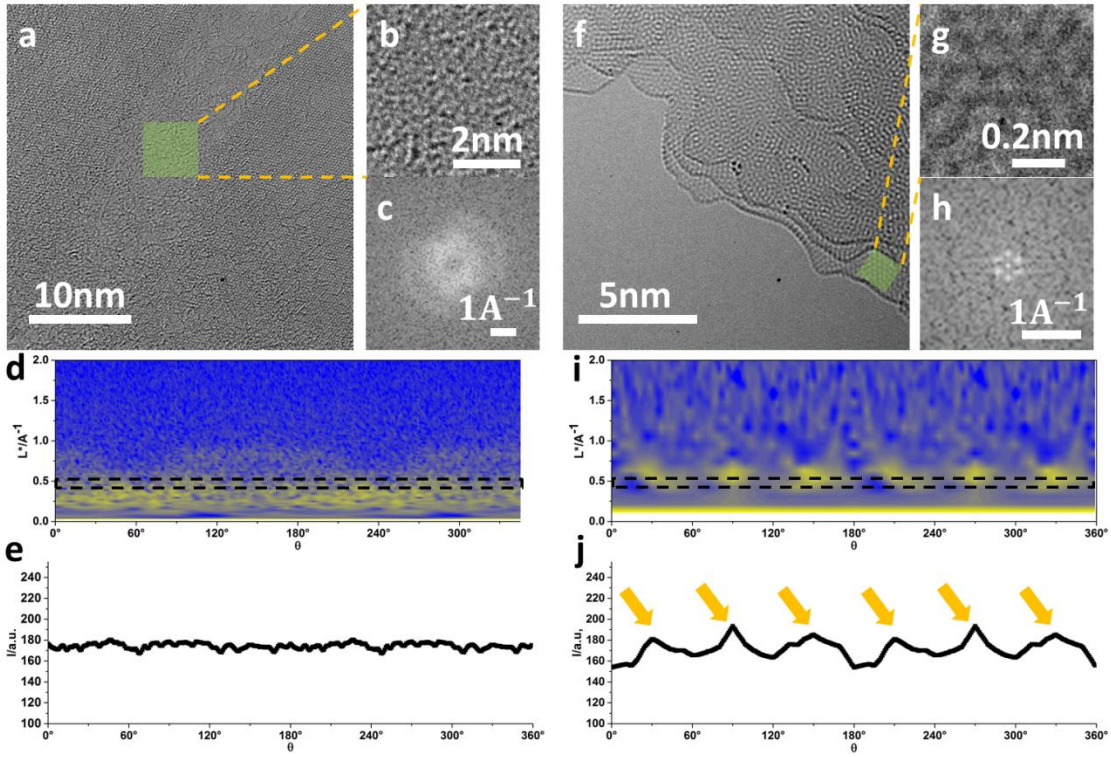


Figure 6-3 Amorphous carbon and graphene film before and after the electric shock. (a)(b) HRTEM image of amorphous carbon covering a crack on WS_2 before the Joule annealing. Image (b) is zoom-in image from the region covered by the green square in (a). (c) FFT of (b). (d) Polar transform of FFT in (c). (e) Intensity profile averaged over the dashed box in (d). No diffraction peak is found. (f)(g) HRTEM image of the edge of graphene formed by the Joule annealing. Image (g) is zoom-in and rotated image from the region covered by the green square in (f). (h) FFT of (g). (i) Polar transform of FFT in (h). (j) Intensity profile averaged over the dashed box in (i). 6 peaks are pointed by the orange arrows, which correlated to the 1st order diffraction spots of graphene.

The structure of 2D film formed by electric break-down of WS_2/amorphous carbon film is further characterized by AC-HRTEM. We compare the TEM image of the amorphous carbon film and the film formed after current shock as shown in Figure 6-3. The thin amorphous carbon film is intentionally introduced by cutting down cleaning time of the TEM sample in active carbon. The details of TEM sample cleaning is recorded in the methodology session of this thesis. The TEM image of amorphous carbon film is taken within a crack of WS_2 (Figure 6-3 (a)). From Figure

6-3 (b) and (c), it is clear that the original amorphous carbon on WS_2 does not show any crystallinity. It is noted that this film remains amorphous after several cycles of Joule annealing under low bias before the break-down. To further confirm the amorphous nature of carbon film on WS_2 before electric break-down, we take the polar transformation of the FFT image (Figure 6-3 (c)) and shown in Figure 6-3 (d). The position in reciprocal space where the 1^{st} order of diffraction of graphene should appear is marked by the dashed rectangle in Figure 6-3 (d). The averaged line profile along the region within the dashed rectangle in Figure 6-3 (d) reveals not apparent diffraction peak as presented in Figure 6-3 (e). In this way, we confirm that the film is totally amorphous before the electric shock and break-down of WS2 crystal.

On the contrary to amorphous carbon film before the Joule annealing process, a clear crystallinity is present after the Joule annealing and break-down of WS_2. Figure 6-3 (f) is the TEM image over the edge of graphene film formed after the electric shock. Multilayer multi-crystal graphene is formed as is indicated by the Moiré pattern in Figure 6-3 (f). By zooming into one of the single layer region, the hexagonal lattice of single layer graphene is observed (Figure 6-3 (g)). Due to the small size of the region of interest, we used FFT of the atomic resolved TEM image (Figure 6-3 (h)) instead of electron diffraction to learn the crystal information from the lattice. The polar transformation of Figure 6-3 (h) clearly shows 6 peaks evenly distributed over $360°$ at the same length (Figure 6-3 (i)). By taking a line profile along the region marked by the dashed rectangle in Figure 6-3 (i), the six peaks are presented in Figure 6-3 (j). As

have mentioned, the position of line profile is determined according to the theoretical position of 1st order diffraction spot of graphene. By fitting the six peaks with a Gaussian peak, we measure the FWHM of them as $16.5°, 17.4°, 32.6°, 16.5°, 17.4°, \text{and } 32.8°$ repectively. The average peak width of the six peaks is $22.2°$, which indicates a relative good crystallinity of the graphene film formed after the Joule annealing.

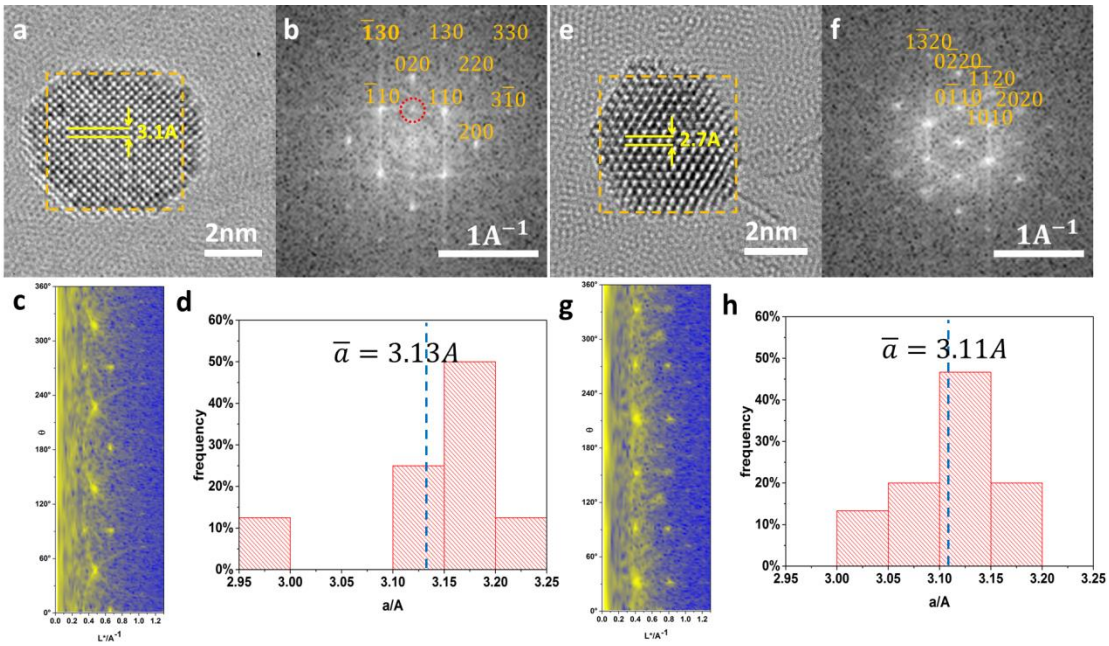


Figure 6-4 Two kinds of typical nanoparticles on graphene film. (a) Tungsten(W) nanoparticle formed by breaking down the WS2 film. (b) FFT of (a). Some of the "diffraction" spots are labelled. The weak spot in red circle is likely to link to (100) planes but with incomplete system extinction. (c) Polar transformation of FFT in (b). The crystal lattice of the nanoparticle clearly shows 4-fold symmetry. (d) Histogram of the lattice constant of tungsten nanoparticle calculated according to its FFT. (e) Remaining WS_2 nanoparticle formed by breaking down the WS_2 film. (f) FFT of (e). The diffraction pattern is labelled. (g) Polar transformation of FFT in (f). The crystal lattice of the nanoparticle clearly shows 4-fold symmetry. (h) Histogram of the lattice of WS_2 nanoparticle constant calculated according to its FFT.

A very interesting result of our experiment is that the graphene film formed by electric

shock is naturally decorated with nanoparticles, as shown in Figure 6-2 (c). The particles are found to vary from WS_2 to W metal particles. HRTEM image of typical W and WS_2 nanoparticles are shown in Figure 6-4 (a) and (e). We attribute the chemical nature of these nanoparticles by considering the crystal symmetry, FFT of the HRTEM and lattice constant of these nanoparticles. The tungsten particles in our experiments all exhibits nearly 4-fold symmetry, with the shape of square or octagon, as shown in Figure 6-4 (a). The {100} family of crystal plane commonly appears as the facet of the nanoparticle, while surface planes belong to {110} family are also found in those octagon shaped nanoparticles. The distance between {100} planes of the W nanoparticle is measured as 3.13A in average as shown in Figure 6-3 (d), which is in consist with the 3.148A for bulk tungsten. The slightly contraction of lattice spacing in metallic nanoparticle comparing with its bulk form is well known for many materials.[21] [22] However, as have mentioned, the uncertainty of our measurement is around 4%, which covers the difference between our measured value and reported lattice constant of W. Since the size of nanoparticles is very small, it is not easy to do electron diffraction on single particle. Instead, we do FFT on our HETEM image with atomic resolution to extract the lattice information. The "diffraction" pattern from FFT apparently shows a 4-fold symmetry. The 1st order diffraction spots (110 spots) are about $0.46A^{-1}$ from the centre in reciprocal space, which correspond to a lattice distance of 2.2A distance between 110 planes. The unit cell edge length is thus 3.1A, which is marked on the HRTEM image of the W nanoparticle (Figure 6-4 (a)). The position of diffraction spots of 1st and higher order can be easily measured from the

polar transformation of FFT, which is shown in Figure 6-4 (c). It is interesting to notice a weak 100 spots are sometimes found in the FFT image, which is highlighted by the red circle in Figure 6-4 (b). The (100) spot should not appear in the diffraction spots in bulk bcc crystals due to systematic extinction. However, the periodical symmetry in nanoparticles are not so strictly obeyed as the bulk form, which could be due to defects or edge effect, and thus a weak but significant spot emerges at the "forbidden position". The systematic extinction of 100 but not 110 spots differentiate the bcc crystal form fcc crystal, which help us to determine the crystal structure of such nanoparticle.

In compare with the W nanoparticles formed after the break down of WS_2, more nanoparticles remain the crystal structure of WS_2, but in the form of nanoparticles. The WS_2 particles exhibit a shape of hexagonal as shown in Figure 6-4 (e). WS_2 nanoparticles produced in our experiments are all terminated with the zigzag edges, which is likely to due to the low "surface" energy of such edges. Similar to the W nanoparticle, we measure the distance between neighbouring crystal lines in zigzag direction and the distance is found to be 2.7A. This corresponds to a length in unit cell of 3.1A, which consists with the reported value of 3.158A. As a reiteration, the uncertainty of our measurement method is around 4%. The FFT of the HRTEM image in Figure 6-4 (f) is ladled in the 4-coordinate way to emphasis the 6-fold symmetry in crystal structure. Figure 6-4 (g) is the polar transformation of the FFT in Figure 6-4 (f) to provide a more instinctive view of the "diffraction" pattern extracted from FFT.

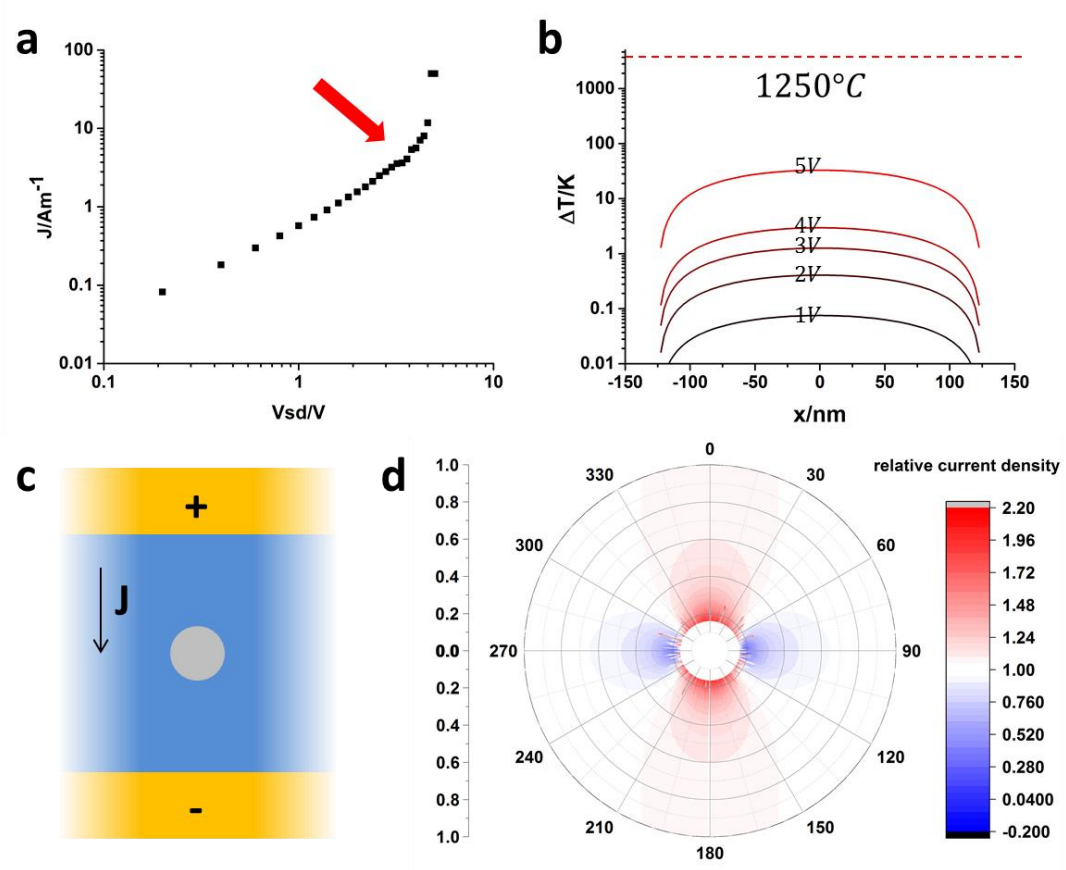


Figure 6-5 Discussion on possible mechanisms. (a) IV plot of the device during breaking down. The red arrow points at the small plateau in current density around the break-down voltage. (b) Temperature increment in the channel. The temperature increment is calculated as in the main text. The melting point of WS_2 is marked by the red dashed line. (c) Schematic of WS_2 with graphene island. (d) Polar contour mapping of relative current density around the graphene islands. The relative current density is the ratio between current density increasing caused by the graphene island divided by the origin current density when no graphene island exists.

Electric shock provides an easy and quick method to produce graphene film decorated with WS_2 nanoparticles. To have a better control of the production, a study on the role of current during the whole reaction is necessary. We will discuss the thermal effect induced by the current first. The thermal effect, together with other effects like electron beam radiation, is found to be unlikely the reason of what we observed. It is

determined that the direct energy transfer from hot charge carrier to the material is the most possible mechanism that is responsible for the quick formation of graphene and break-down of WS_2.

Thermal effect induced by Joule annealing is well known in the study of graphene and other 2D materials. The temperature of sample can be estimated by solving the stable state thermal transformation equation.

$$\kappa\nabla^2 T + \rho = 0 \qquad \text{eq. 6-1}$$

In eq. 6-1, κ is the thermal conductivity of material, T is temperature, and ρ is the input power density or "heat flux". In the case of our study, we can estimate the heat flux by considering the electric power as measured in the IV measurement.

$$\rho = \frac{UI}{WLt} \qquad \text{eq. 6-2}$$

In eq. 6-2, ρ is the heat flux, U is the source-drain voltage, I is the source-drain current, W is the channel width, L is the channel length and t is the thickness of monolayer WS_2 used in this experiment. Considering the geometry of our device, we can further assume that the temperature only changes perpendicular to the edges of two electrodes. Combining eq. 6-1 and eq. 6-2, and consider the symmetry of our system, we have:

$$\kappa\frac{d^2}{dt^2}T + \frac{UI}{WLt} = 0 \qquad \text{eq. 6-3}$$

The meaning of letters in eq. 6-3 is same as in eq. 6-1 and eq. 6-2. The solution of eq. 6-3 describes a parabolic distribution of the temperature perpendicular to the electrodes.

$$\Delta T = \frac{UI}{2WLt\kappa}(x - \frac{L}{2})(x + \frac{L}{2}) \qquad \text{eq. 6-4}$$

In eq. 6-4, ΔT is the temperature increasing, x is the lateral coordinate of the point of concern. The two electrodes are assumes to be the thermal reservoir located at $\pm\frac{L}{2}$, where L is the channel length. By taking $\kappa = 34\mathrm{Wm^{-1}K^{-1}}$,[23] [24] $W = 2\mu\mathrm{m}$, $L = 250\mathrm{nm}$, $t = 0.7\mathrm{nm}$ and the experimentally measured IV relation, can we estimate the change of temperature increasing from current annealing. The results are plotted in Figure 6-5 (b). It is noted that the thermal energy provided by Joule annealing is far insufficient to induce any significant change in the WS_2 domain. Furthermore, thermal induced graphitization of amorphous carbon only happens at high temperature. [6] In this way, we rule out the thermal effect as major reason causing the experimental results.

We also rule out the influence of the incident electron beam by sheltering the electron beam off from the sample when doing the current processing in this report. Control experiments with and without the illumination of electron beam from TEM does not reveal any significant difference in measurement in terms of break-down voltage, or size of WS_2 particles after the breakdown. Other factors like the chemical reaction with the measurement is also unlikely to be significant due to the high vacuum ($< 10^{-5}\mathrm{Pa}$) of the TEM chamber and chemical inertia of the substrate (Si_3N_4).

The direct formation of WS_2 nanoparticle decorated graphene film from WS_2/amorphous carbon film can be understand as a result of direct energy transfer

from hot electrons to conducting material. The electrons are injected from the electrodes into the conduction band of the WS_2. When the electric field induced by the source-drain bias increases, the mean-velocity of electrons in WS_2 increases. In the high field regime, however, the collision between electron and lattice become so strong that the current no longer increase when increasing the voltage, which is known as the velocity saturation. This is measured as a plateau in the IV curve of the device as pointed by the red arrow in Figure 6-5 (a). Higher bias would start to result the impact ionization process caused by hot charge carriers. The energy is quickly transferred from the electrons to the lattice of WS_2 and amorphous carbon, which induce the break of chemical bonds locally.

Once the break-down happens, islands of graphene form on the surface of WS_2. The local conductance is thus increases due to the graphitization. The increased conductance will further "attract" the electric field nearby and results a local increasing current around the graphene islands. This is schematically shown and simulated in Figure 6-5 (c) and (d). Higher current would results a more frequently collision between hot charge carriers and lattice of WS_2/amorphous-carbon film. The current induced transformation from amorphous carbon coated WS_2 film to WS_2 nanoparticle decorated graphene film is thus self-accelerated.

Conclusion

We discovery a simple method to produce WS_2 nanoparticle embedded in graphene

substrate by electric shock. Graphitization of amorphous carbon is induced by current in accompany with a break-down of the WS_2. Our method enables an energy efficient one-step production method for WS_2 nanoparticle on graphene substrate, which is potentially important for the catalytic applications of WS_2. In addition, our synthesis method demonstrates a good potential as a general method in the production of nanoparticles decorated graphene film.

6.3 Negative Electro-Conductance of WS_2 Nano-Device

6.3.1 Introduction

2D semiconductors, such as WS_2 and MoS_2, have recently attracted significant attention due to their direct band gap, which makes them suitable for semiconductor electronic and opto-electronic applications including transistors, photodetectors and light emitting devices.[25] The ultrathin monolayer has enabled a variety of different device structures to be explored, including lateral and vertical geometries. Electronic applications from diode with homo-junction[26] and hetero-junction[27] to transistors[28] and to logic circuit[29] [30] have been reported. Photodetectors making use of the photo-conductivity of single material[31] or photo-induced-current in p-n junction[32] have also been realized. The former device generally exhibits a large photo-responsivity but slow response time due to existence of trap states.[33] [34] [35]

Despite the intensive work on 2D photo-detectors, investigation on electron detection using 2D materials is limited. Part of the reason is the challenge of experimentally

implementing electron irradiation compared to optical excitation of devices. *In-situ* electrical measurements of devices inside transmission electron microscope (TEM) using specialized electrical biasing holders enable simultaneous characterization of electrical performance and atomic structure. Recent works on nanowires have made use of STEM:TEM in-situ TEM holders that utilize piezo controlled sharp metal tips as electrodes to direct contact suspended wires,[36 37] but this approach is not ideal for making uniform contacts with 2D materials that have larger surface area compared to nanowires. Electron beam lithography to pattern and fabrication nanoscale electronic devices containing graphene has proved to be a more effective approach to achieve in-situ electrical measurement of 2D materials. The conductivity change of graphene as a nanoribbon[38 39 40 41] or atomic carbon chain[42] has been studied by different groups. A Schottky junction between graphene nanoribbons and bulk regions has also been reported.[43] When graphene is placed under high electrical bias crack propagation has been shown to occur.[44] More advanced lithographic methods have shown that in-situ gating of graphene nanoribbons can be achieved using side gates within in-situ TEM experiments.[45] More recently, the in-situ electrical biasing TEM studies of 2D materials has been extended from graphene to MoS_2, where conductivity changes induced by electron beam damage was reported.[46]

The atomically thin nature of 2D semiconductors (e.g. WS_2) makes them interesting candidates for applications in electron detection. In electron detectors made with 3D bulk materials, nearly all the incident electrons are stopped by the detector, making

the detector opaque and the mechanisms behind the electro-conductance response relatively complex. 2D materials such as WS_2 are highly transparent to electron beam due to their monolayer thickness and thus offer the opportunity for electron detectors that are effectively electron transparent, enabling the majority of the electron beam to propagate through the device and proceed to other multi-functional detectors.

In this report, we examine the electron detection ability of suspended monolayer WS_2 nano-electronic devices using an *in-situ* electrical biasing holder within an aberration-corrected TEM (AC-TEM). An accelerating voltage of 80kV is used to provide electrons with reduced knock-on damage and therefore holes or damage will not rapidly occur in the ultrathin WS_2 monolayer. Changes in conductivity of WS_2 as a function of electron beam current density are studied, along with switching of the electron beam on and off to demonstrate non-destructive cycling of the electro-conductance.

6.3.2 Device Fabrication and Materials Characterization

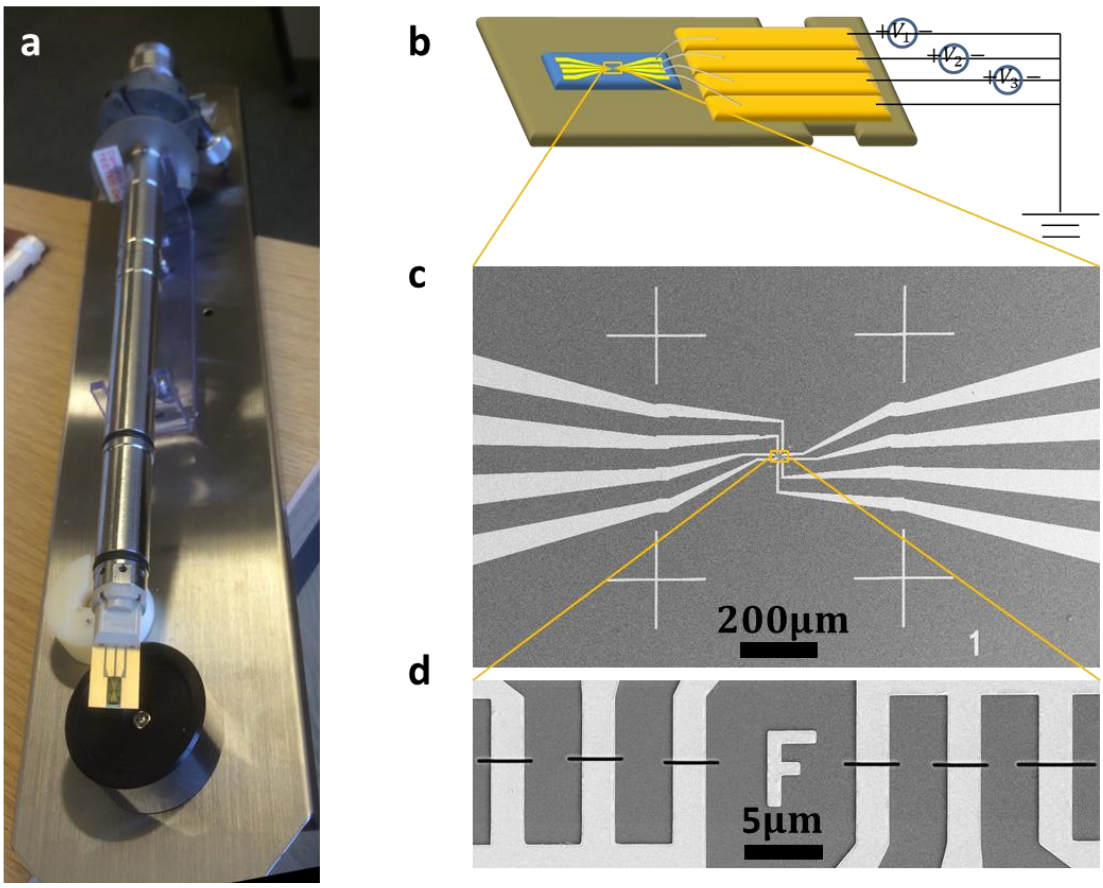


Figure 6-6 Experimental set-up *in-situ* electrical biasing within the AC-TEM. (a) Photograph of the electrical *in-situ* biasing TEM holder. (b) Schematic image of the nanoscale electronic devices with bond pads to connect to the biasing holder with electrical feedthroughs. (c) and (d) SEM images of the electrodes on chip. Electrodes are produced on the silicon nitride (SIN) insulating layer covering the silicon substrate for *in-situ* electrical measurement.

We fabricated nanoelectronic devices using electron beam lithography methods on a thin silicon chip with 100nm silicon nitride thin film. Gold electrodes are aligned to an $10\mu m \times 50\mu m$ suspended silicon nitride (SIN) observation window in the centre of the chip. The slits in the electrodes are produced using focused ion beam (FIB) irradiation, using similar methods as we previously reported.[47] The introduction of the slit in the gold wire separates the source from the drain to produce a two electrode structure. 6 devices in total are fabricated on one chip and are categorized into two

groups. Devices in the same group are co-sourced (Figure 6-6 (d)). The SEM image of as fabricated chip is shown in Figure 6-6 (c) and (d). The channel length of our device is 250nm, with a 2μm channel width. The large aspect ratio between channel width and channel length results the "short-channel" geometry and enables uniform electrical field through the WS_2 when it is biased.

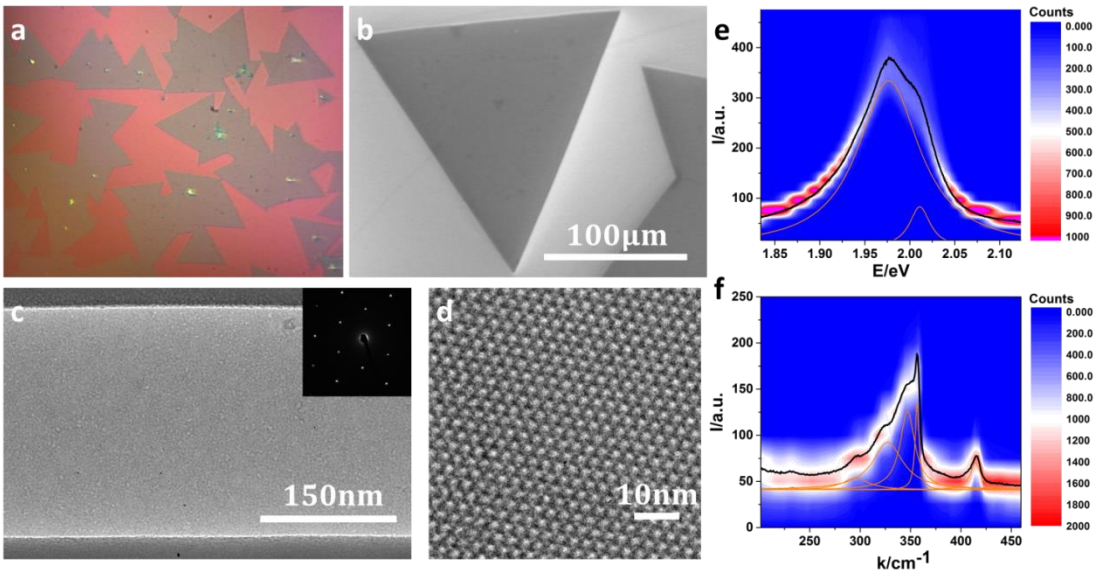


Figure 6-7 Characterization of CVD WS_2. (a) Optical microscope image of as-grown WS_2 on a silicon substrate. (b) SEM image of a WS_2 domain. (c) Low-magnification TEM image of suspended WS_2 within the *in-situ* TEM electrical holder. Insertion is the electron diffraction pattern of WS_2. (d) AC-TEM image of the hexagonal WS_2 lattice with black atom contrast. (e) Histogram of PL spectra from WS_2. Black curve is the average spectrum of WS_2 over all spots. Orange curves are the trion and exciton peaks that comprise the PL spectrum. (f) Histogram of Raman spectra from WS_2. The black line is the average spectrum of WS_2 over all spot in statistic. Orange curves are phonon modes that contribute to the Raman spectrum.

We characterized the Chemical vapour deposition (CVD) grown WS_2 before carrying out *in-situ* electrical measurements to ensure its quality. Single domains of CVD grown WS_2 (Figure 6-7 (a) and (b)) are used for the *in-situ* measurement in this study. The low-magnification TEM image in Figure 6-7 (c) shows the WS_2 after transfer

onto the *in-situ* TEM chip and reveals the suspended region. Selected area electron diffraction was taken from this suspended region of WS_2 and shows only one set of electron diffraction spots, confirming the single crystallinity of WS_2 across the electrode gap (insertion of Figure 6-7 (c)). Despite the small amount of amorphous residue on the surface, the transferred WS_2 is clean enough to resolve the atomic lattice in AC-TEM images (Figure 6-7 (d)). We find if the WS_2 contains excessive amounts of surface contamination then the measurement of the electro-conductance becomes unstable. The quality of WS_2 used in this experiment is further evaluated by photoluminescence and Raman spectroscopy. Since only a small portion of WS_2 is across the device, we take hundreds of different measurement spots to get statistical information of overall quality of WS_2 in this experiment. Figure 6-7 (e) and (f) are the histograms of spectra of CVD grown WS_2. In each image, the colour reflects the counts and the black curve marks the average spectrum. Both Photo-luminescence (PL) and Raman spectra are measured with a 532nm laser. The PL spectrum consists of a trion peak and an exciton peak. The energy of trion and exciton is measured as 1.98eV and 2.01eV respectively, which is in accordance with previously reported values.[48] [49] The large ratio between the trion and exciton peak indicate the n-doped nature of the meaterial. Many secondary resonance peaks appear in the Raman spectrum of our sample similarly to previously reported works.[50] [51] The peak shift and height ratio between E_{2g} (356.5cm^{-1}) peak and A_{1g} (414.4cm^{-1}) peak are 57.9cm^{-1} and 3.16 respectively. This confirms the single layer nature of the CVD WS_2.[52]

6.3.3 Experimental results and discussion

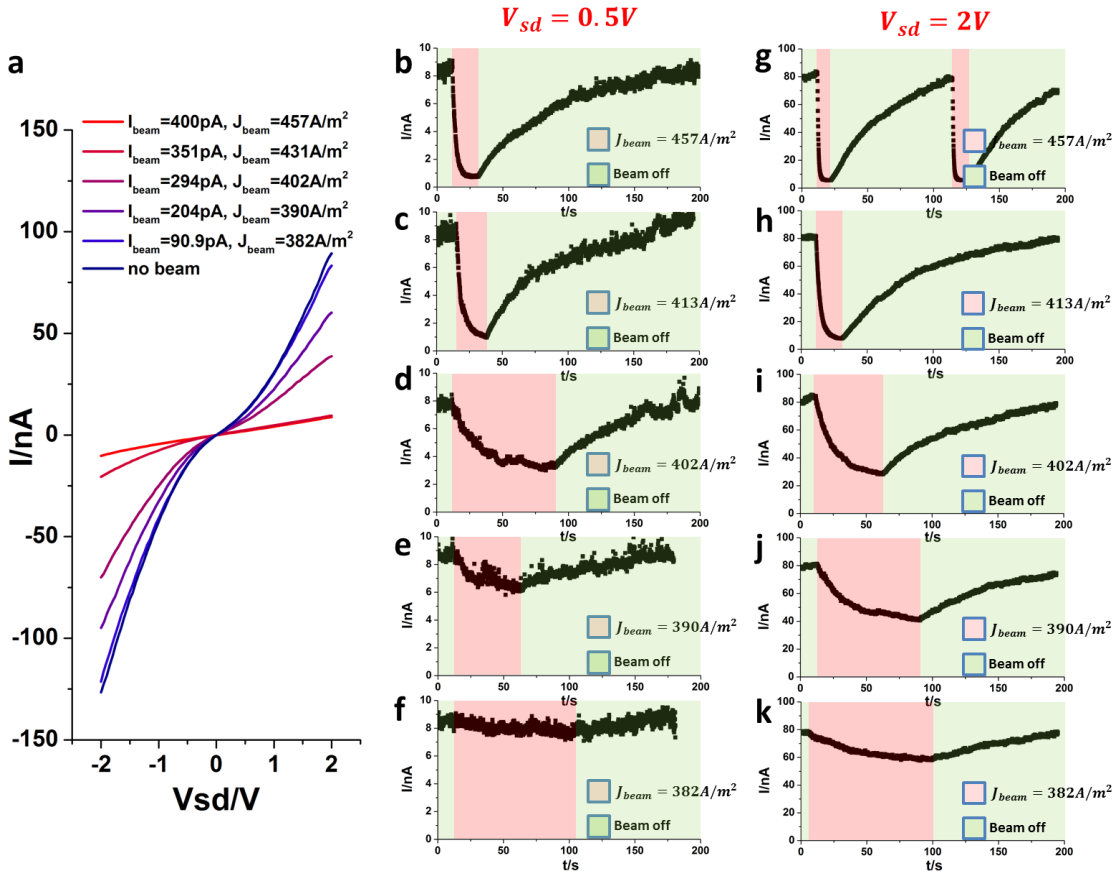


Figure 6-8 Current response of WS_2 to incident electron beam exposure. (a) IV sweep under different electron illumination condition. Nonlinear IV curve is typical for WS_2 devices with a Schottky contact. DC current decreases with increasing electron beam intensity (I_{beam}) and density (J_{beam}). (b)-(f) Time resolved response of device to incident electron beam at low bias ($V_{sd} = 0.5V$). The on/off state of the incident electron beam is indicated by the colour of the background (green background for beam off, red background for beam on). (g)-(k) Time resolved response of device to incident electron beam at high bias ($V_{sd} = 2V$). The on/off state of the incident electron beam is indicated by the colour of background (green background for beam off, red background for beam on).

Figure 6-8 shows the change in current of the biased WS_2 device upon exposure to the electron beam. The monolayer single crystal CVD grown WS_2 in our experiment exhibits a negative electro-conductivity, i.e. the conductance of WS_2 is lowered by the incident electron beam. By varying the incident electron beam density, we measure a

change in the IV curve of WS_2. Before carrying out the electro-conductivity measurements the device is annealed by Joule heating. Similar to previous reports on electronic measurement of WS_2,[53] we find that a long period of Joule annealing is necessary to get stable device performance. Inspection of the device by high resolution TEM imaging confirms that this procedure does not damage the WS_2. The IV sweep of WS_2 under different electron beam current densities is shown in Figure 6-8 (a). When the electron beam is off, "dark" current up to ~ 100nA is measured under 2V bias. This results in a conductivity of 6.1nS (by assuming channel length = 250nm, channel width = 2000nm) which is typical for single layer WS_2 in vacuum.[53] [54] [55] The non-linear IV curve is due to the Schottky contact between WS_2 and the gold electrode contact. When the electron beam is switched on and is incident onto the WS_2 device, the DC current drops down to less than 10% of the dark current. For example, the current passing through WS_2 at a 2V bias decreases from 90nA to 8.7nA when the beam current density increases from 0 to 457A/m^2 (Figure 6-8 (a)).

An intriguing response and recovery process of WS_2 to incident electron beam is revealed in Figure 6-8 (b)-(f) and 3(g)-(k). DC current flow in WS_2 decreases sharply when the device is exposed to the electron beam, but increases slowly after the beam is shut off. Hereafter, we call the decreasing of DC current when turning on the electron beam as "response" process and the increasing of DC current due to turning off the electron beam as "recovery" process. The cyclic response and recovery processes are measured multiple times by manually controlling the beam valve to

switch the electron beam on and off. One cycle of each measurement is shown in Figure 6-8 to illustrate the behaviour. The current recovers to its original value when the beam is turned off again (as seen in Figure 6-8 (b)-(g)).

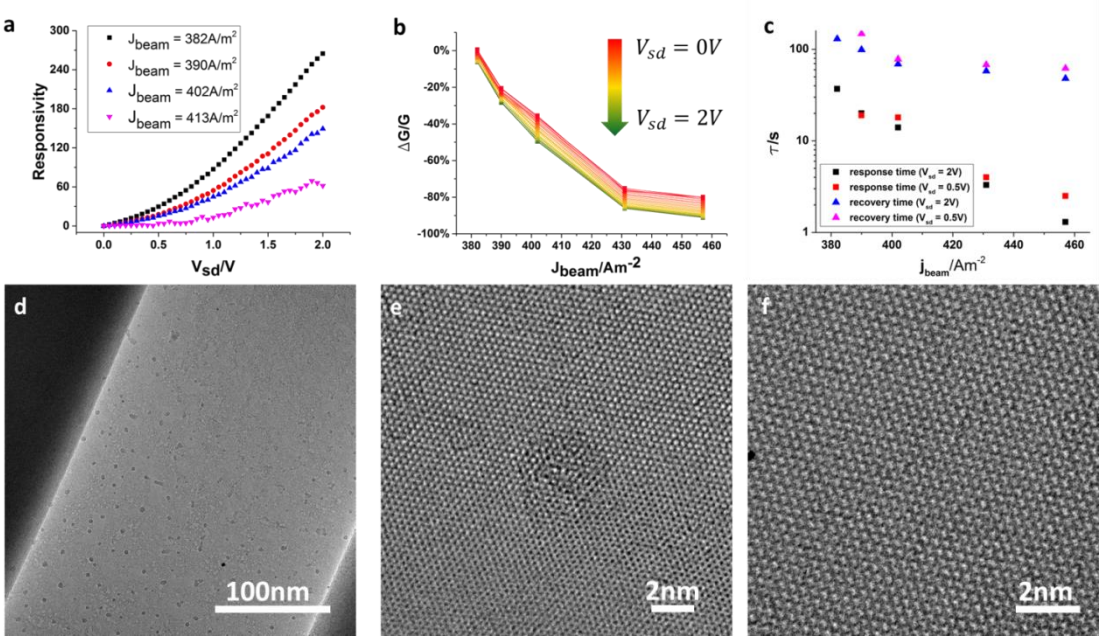


Figure 6-9 Characterization of the device to incident electron beam. (a) Electro-responsivity of the WS_2 device. The electro-responsivity is defined as the ratio between change of IV current and incident electron beam, which increases with increasing source-drain bias as well as incident beam current. (b) Relative change in conductance of the device due to incident electron beam. The conductivity of WS_2 decreases down to 10% of its original value when illuminated by the electron beam. (c) Dependence of response time on incident beam density. Both the response and recovery time does not strongly rely on the source-drain bias. The response time decrease with increasing beam density, while the recovery time keeps almost unanged. (d) – (f) TEM image of WS_2 in this experiment. (d) Low-mag TEM image of WS_2. Small clusters appear on the WS_2 after Joule annealing. (e) AC-TEM image of one cluster on WS_2 lattice. (f) AC-TEM image of clean region of WS_2.

To further understand the DC response of WS_2 to incident electron beam, we define the electro-responsivity as following:

$$Responsivity = |\frac{I - I_{dark}}{I_{beam}}| \qquad \text{eq. 6-5}$$

In eq. 6-5, I is the measured source-drain current when the electron beam illuminates the device, I_{dark} is the dark current (i.e. the current of device when the electron beam is off), and I_{beam} is the incident beam current. The electro-responsivity defined here can be seen as an analogy to the photo-responsivity and represents how sensitive the device is to the incident electron beam. The electro-responsivity at each bias and electron beam density is calculated and shown in Figure 6-9 (a). Within our experimental range, the electro-responsivity increases monotonically with increasing bias and incident beam current.

The dependence of electro-responsivity on source-drain bias indicates that our device acts as an "electro-conductor", analogous to photo-conductor, of which conductance changes when exposed to light. The change of conductance is plotted in Figure 6-9 (b). The conductance of the device varies for different source-drain biases due to its Schottky contact with the gold electrodes. However, the trend of decreasing conductance with increasing beam density is clear (Figure 6-9 (b)). When the beam current density reaches 457A/m^2, the conductance of WS_2 decays to only 9.8% of its conductance in the dark.

Besides the change in conductance, the reaction speed of WS_2 to the external electron beam is also studied. By fitting a time dependence curve in Figure 6-8 (b) and (c), with a formula describing an exponential decay:

$$I = I_0 + I_1 \exp(-t/\tau) \qquad \text{eq. 6-6}$$

In eq. 6-6, I is the measured current, I_0 and I_1 are two fitting parameters and τ is the characteristic response time of the device, we can extract the response (or recovery) time of our device (Figure 6-9 (c)). Both the response time and the recovery time are found to independent on source-drain bias. However, the response time varied from the range of 10^0 to 10^1 seconds in our experiment, while the recovery time is stable at around 10^2 seconds. The response time is about one order of magnitude smaller than the recovery time (Figure 6-9 (c)), which means the device reacts much quicker to the turning on of the electron beam compared to turning off. The time scale of response and recovery is similar to TMD high-gain photo detectors using CVD grown material [31 56], but slower than other photo detectors[28 57]. The recovery time is almost constant regardless of the density of the beam illumination on the device. On the contrary, the response time significantly depends on the beam density.

Although negative electro-conductance is not often reported in 2D materials, there are several mechanisms that could help to understand the experimental results. We start from considering the effect of beam damage. It is known that electron beam damage to WS_2 can introduce sulphur vacancies and other defects.[58 59] Some of the vacancies recombine into line defects at high temperature which can serve as 1D conductive channel when infinitely long.[60] We do find small holes and vacancies after long period of electron beam radiation, which is similar to references as mentioned. However, no line defects were observed during the experiment Figure 6-9 (e) and (f)), though Joule heating effect may increase the temperature of device. Besides, all IV measurements

are repeated by several cycles to rule out the possibility that beam damage dominates the changes in conductance as we observed. In this way, it is unlikely that our observation is due to structure change.

Another possible explanation for negative electro-conductance is the decreasing of charge carrier mobility due to formation of charged electron-hole clusters (like trion) when abundance of free electrons and holes exist in the system. This mechanism explains the transient negative photo-conductivity in monolayer MoS_2 at low temperature.[61] However, our experiment condition disagrees with the one in reference in both measurement time scale (second vs pico-second) and temperature (room temperature vs cryogenic temperature). In this way, formation of electron-hole combinations is unlikely to account for our experiment results.

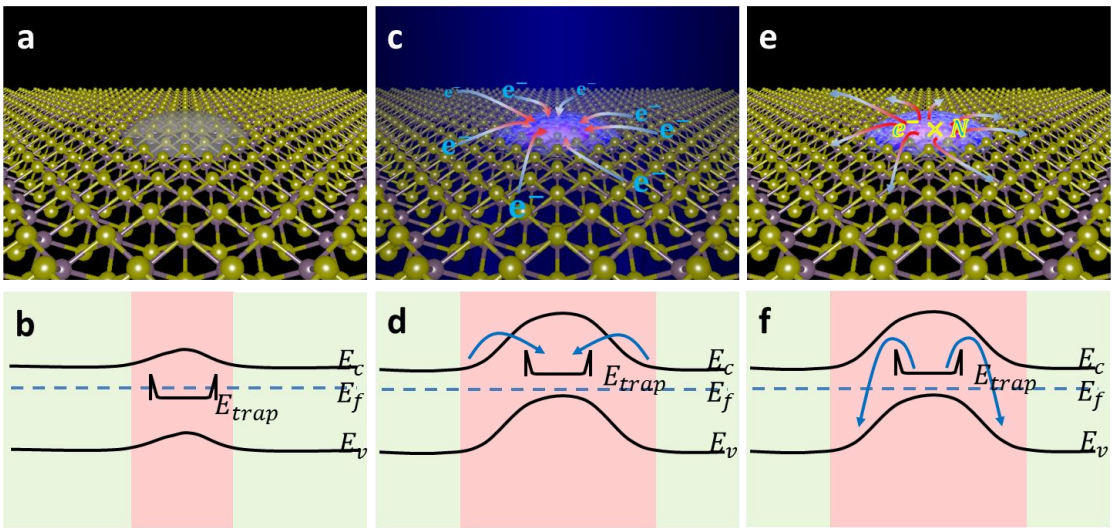


Figure 6-10 Schematic illustrating the mechanism of negative electro-conductance in suspended WS_2. (a) Artistic image and (b) band diagram of WS_2 with trap states before e-beam illumination. (c) Artistic image and (d) band diagram of WS_2 with trap states being illuminated by incident electron beam. Hot charge carriers (electrons) fill the trap states quickly. (e) Artistic image and (f) band diagram of WS_2 with trap states

right after the incident beam is shut off. The trap states slowly discharges.

One mechanism that may explain the negative electro-conductance of WS_2 is the trapping of hot charge carriers. A similar mechanism is widely used to explain the negative photo-conductance phenomenon.[62] [63] [64] The 80keV electron beam energy in our experiment is much higher than the band gap of WS_2 (~2eV). Inelastic scattering leads to the transfer of energy from the electron beam to the WS_2 that can cause a large number of electrons to be promoted to the conduction band as hot charge carriers. Structure defects[65] [66], surface nano-clusters[63] [67] or even absorbed molecules[68] can also act as charge traps for electrons in the conduction band. This will result in a negatively charged trap centre surrounded by a positively charged local region of the WS_2. These negatively charged trap centres may scatter the charge carriers in WS_2. Another way to view the process is to consider the charged trap centres as a local negative gate bias applied to WS_2, which results in a p-doping of the originally n-doped WS_2. A lot of small p-n junction may then be formed inside the WS_2 sheet and thus reduce the conductivity. This mechanism is schematically illustrated in Figure 6-10.

Our experimental results fit well with the process discussed above. According to this mechanism, when increasing the incident beam density, the trap states should be charged more quickly. In our experiment, the response time negatively depends on the incident electron beam density (Figure 6-9 (c)), which is as expected. On the other hand, the time to discharge the trap (recovery time) should not rely on beam current

density that the device is previously exposed to, but only on the energy barrier between the trap centres and WS_2. In addition, hot electrons stimulated by the incident electron beam can easily overcome the energy barrier around the traps and lead to a quick response time (Figure 6-10 (c)-(d)). When the traps are discharged, trapped electrons can only slowly tunnelling through the barrier and thus the recovery time is much slower than the response time (Figure 6-10 (e)-(f)). All these phenomena are supported by our experiments (Figure 6-9 (c)).

Conclusion

In-situ nanoscale electronic devices containing suspended monolayer WS_2 are demonstrated to exhibit negative electro-conductivity. The conductance of the WS_2 is tuned by external electron beam exposure up to an order of magionnitude. The response of the device to external electron beam is found to be of the time scale of seconds. These fundamental results may help the future development of transparent ultrathin direct electron beam detectors based on 2D transition metal dichalcogenides.

Reference

1. Fan, Y. *et al.* Negative Electro-conductance in Suspended 2D WS 2 Nanoscale Devices. *ACS Appl. Mater. Interfaces* **8,** 32963–32970 (2016).
2. Moser, J., Barreiro, A. & Bachtold, A. Current-induced cleaning of graphene. *Appl. Phys. Lett.* **91,** 1–4 (2007).
3. Dong, L. *et al.* Effects of local Joule heating on the reduction of contact

resistance between carbon nanotubes and metal electrodes. *J. Appl. Phys.* **101,** 0–7 (2007).

4. Barreiro, A. *et al.* Understanding the catalyst-free transformation of amorphous carbon into graphene by current-induced annealing. *Sci. Rep.* **3,** 1115 (2013).
5. Shu, J. *et al.* The Intrinsic Origin of the Hysteresis in the MoS2 Field Effect Transistors. *Nanoscale* 3049–3056 (2016). doi:10.1039/C5NR07336G
6. Dave, S. H., Gong, C., Robertson, A. W., Warner, J. H. & Grossman, J. C. Chemistry and Structure of Graphene Oxide via Direct Imaging. *ACS Nano* **10,** 7515–7522 (2016).
7. Bazargan, A. M., Sharif, F., Mazinani, S. & Naderi, N. Highly conductive reduced graphene oxide transparent ultrathin film through joule-heat induced direct reduction. *J. Mater. Sci. Mater. Electron.* (2016). doi:10.1007/s10854-016-5676-x
8. Yao, P. *et al.* Electric current induced reduction of graphene oxide and its application as gap electrodes in organic photoswitching devices. *Adv. Mater.* **22,** 5008–5012 (2010).
9. Ekiz, O. O., Ürel, M., Güner, H., Mizrak, A. K. & Dâna, A. Reversible electrical reduction and oxidation of graphene oxide. *ACS Nano* **5,** 2475–2482 (2011).
10. Tauster, S. J., Pecoraro, T. A. & Chianelli, R. R. Structure and properties of molybdenum sulfide: Correlation of O2 chemisorption with hydrodesulfurization activity. *J. Catal.* **63,** 515–519 (1980).

11. Jaramillo, T. F. *et al.* Identification of active edge sites for electrochemical H2 evolution from MoS2 nanocatalysts. *Science* **317,** 100–102 (2007).

12. Farias, M. H., Gellman, A. J., Somorjai, G. A., Chianelli, R. R. & Liang, K. S. The CO coadsorption and reactions of sulfur, hydrogen and oxygen on clean and sulfided Mo(100) and on MoS2(0001) crystal faces. *Surf. Sci.* **140,** 181–196 (1984).

13. Yang, J. *et al.* Two-dimensional hybrid nanosheets of tungsten disulfide and reduced graphene oxide as catalysts for enhanced hydrogen evolution. *Angew. Chemie - Int. Ed.* **52,** 13751–13754 (2013).

14. Yan, Y. *et al.* Vertically oriented MoS2 and WS2 nanosheets directly grown on carbon cloth as efficient and stable 3-dimensional hydrogen-evolving cathodes. *J. Mater. Chem. A* **3,** 131–135 (2015).

15. Bhimanapati, G. R. *et al.* Growth and Tunable Surface Wettability of Vertical MoS_2 Layers for Improved Hydrogen Evolution Reactions. *ACS Appl. Mater. Interfaces* acsami.6b05848 (2016). doi:10.1021/acsami.6b05848

16. Ye, G. *et al.* Defects Engineered Monolayer MoS2 for Improved Hydrogen Evolution Reaction. *Nano Lett.* **16,** 1097–1103 (2016).

17. Voiry, D. *et al.* Enhanced catalytic activity in strained chemically exfoliated WS2 nanosheets for hydrogen evolution. *Nat. Mater.* **12,** 850–855 (2013).

18. Zhou, H. *et al.* Highly active and durable self-standing WS2/graphene hybrid catalysts for hydrogen evolution reaction. *J. Mater. Chem. A* **4,** 9472–9476 (2016).

19. Chen, Y. *et al.* Rapid, in Situ Synthesis of High Capacity Battery Anodes through High Temperature Radiation-Based Thermal Shock. *Nano Lett.* **16,** 5553–5558 (2016).

20. Lembke, D. & Kis, A. Breakdown of high-performance monolayer MoS2 transistors. *ACS Nano* **6,** 10070–10075 (2012).

21. Qi, W. H. & Wang, M. P. Size and shape dependent lattice parameters of metallic nanoparticles. *J. Nanoparticle Res.* **7,** 51–57 (2005).

22. Wasserman, H. J. & Vermaak, J. S. On the determination of the surface stress of copper and platinum. *Surf. Sci.* **32,** 168–174 (1972).

23. Peng, B. *et al.* Thermal conductivity of monolayer MoS 2 , MoSe 2 , and WS 2 : interplay of mass effect, interatomic bonding and anharmonicity. *RSC Adv.* **6,** 5767–5773 (2016).

24. Peimyoo, N. *et al.* Thermal conductivity determination of suspended mono- and bilayer WS2 by Raman spectroscopy. *Nano Res.* **8,** 1210–1221 (2015).

25. Wang, Q. H., Kalantar-Zadeh, K., Kis, A., Coleman, J. N. & Strano, M. S. Electronics and optoelectronics of two-dimensional transition metal dichalcogenides. *Nat. Nanotechnol.* **7,** 699–712 (2012).

26. Suh, J. *et al.* Doping against the native propensity of MoS2: Degenerate hole doping by cation substitution. *Nano Lett.* **14,** 6976–6982 (2014).

27. Li, M.-Y. M.-Y. *et al.* Epitaxial growth of a monolayer WSe2-MoS2 lateral p-n junction with an atomically sharp interface. *Science.* **349,** 524–528 (2015).

28. Yin, Z. *et al.* Single-layer MoS2 phototransistors. *ACS Nano* **6,** 74–80 (2012).

29. Tosun, M. *et al.* High-Gain Inverters Based on WSe2 Complementary Field-Effect Transistors. *ACS Nano* **8,** 4948–4953 (2014).

30. Wang, H. *et al.* Integrated Circuits Based on Bilayer MoS2 Transistors. *Nano Lett.* **12,** 4674–4680 (2012).

31. Lopez-Sanchez, O., Lembke, D., Kayci, M., Radenovic, A. & Kis, A. Ultrasensitive photodetectors based on monolayer MoS2. *Nat. Nanotechnol.* **8,** 497–501 (2013).

32. Pospischil, A., Furchi, M. M. & Mueller, T. Solar-energy conversion and light emission in an atomic monolayer p-n diode. *Nat. Nanotechnol.* **9,** 257–61 (2014).

33. Koppens, F. H. L. *et al.* Photodetectors based on graphene, other two-dimensional materials and hybrid systems. *Nat. Nanotechnol.* **9,** 780–793 (2014).

34. Kufer, D. & Konstantatos, G. Highly Sensitive, Encapsulated MoS2 Photodetector with Gate Controllable Gain and Speed. *Nano Lett.* **15,** 7307–7313 (2015).

35. Fan, Y. *et al.* Photoinduced Schottky Barrier Lowering in 2D Monolayer WS 2 Photodetectors. *Adv. Opt. Mater.* (2016). doi:10.1002/adom.201600221

36. Wang, Z. L., Poncharal, P. & de Heer, W. a. Nanomeasurements of individual carbon nanotubes by in situ TEM. *Pure Appl. Chem.* **72,** 209–219 (2000).

37. Jin, C., Wang, J., Wang, M., Su, J. & Peng, L.-M. In-situ studies of electron field emission of single carbon nanotubes inside the TEM. *Carbon.* **43,** 1026–

1031 (2005).

38. Qi, Z. J. *et al.* Direct electron beam patterning of sub-5nm monolayer graphene interconnects. in *Proc. SPIE* (eds. Tong, W. M. & Resnick, D. J.) **8680,** 86802F (2013).

39. Qi, Z. J. *et al.* Correlating Atomic Structure and Transport in Suspended Graphene Nanoribbons. *Nano Lett.* **14,** 4238–4244 (2014).

40. Qi, Z. J. *et al.* Electronic transport of recrystallied freesanding graphene nanoribbons. *ACS Nano* **9,** 3510–3520 (2015).

41. Lu, Y., Merchant, C. A., Drndić, M. & Johnson, A. T. C. In situ electronic characterization of graphene nanoconstrictions fabricated in a transmission electron microscope. *Nano Lett.* **11,** 5184–5188 (2011).

42. Cretu, O. *et al.* Electrical transport measured in atomic carbon chains. *Nano Lett.* **13,** 3487–3493 (2013).

43. Wang, Q. *et al.* Fabrication and In Situ Transmission Electron Microscope Characterization of Free-Standing Graphene Nanoribbon Devices. *ACS Nano* **10,** 1475–1480 (2016).

44. Barreiro, A., Börrnert, F., Rümmeli, M. H., Büchner, B. & Vandersypen, L. M. K. Graphene at high bias: Cracking, layer by layer sublimation, and fusing. *Nano Lett.* **12,** 1873–1878 (2012).

45. Rodr ́guez-manzo, J. A. *et al.* In Situ Transmission Electron Microscopy Modulation of Transport in Graphene Nanoribbons. *ACS Nano* **10,** 4004–4010 (2016).

46. Parkin, W. M. *et al.* Raman Shifts in Electron-Irradiated Monolayer MoS 2. *ACS Nano* **10,** 4134–4142 (2016).

47. Wang, H. *et al.* Carbon nanotube nanoelectronic devices compatible with transmission electron microscopy. *Nanotechnology* **22,** 245305 (2011).

48. Peimyoo, N. *et al.* Chemically Driven Tunable Light Emission of Charged and Neutral Excitons in Monolayer WS2. *ACS Nano* **8,** 11320–11329 (2014).

49. Zhu, B., Chen, X. & Cui, X. Exciton Binding Energy of Monolayer WS2. *Sci. Rep.* **5,** 9218 (2015).

50. Zhao, W., Ghorannevis, Z., Amara, K. & Pang, J. Lattice dynamics in mono-and few-layer sheets of WS2 and WSe2. *Nanoscale* **5,** 9677–83 (2013).

51. Loh, T. A. J., Chua, D. H. C. & Wee, A. T. S. One-step Synthesis of Few-layer WS2 by Pulsed Laser Deposition. *Sci. Rep.* **5,** 18116 (2015).

52. Berkdemir, A. *et al.* Identification of individual and few layers of WS2 using Raman spectroscopy. *Sci. Rep.* **3,** 1755 (2013).

53. Ovchinnikov, D., Allain, A., Huang, Y., Dumcenco, D. & Kis, A. Electrical Transport Properties of Single-Layer WS2. *ACS Nano* **8,** 8174–8181 (2014).

54. Khalil, H. M. W., Khan, M. F., Eom, J. & Noh, H. Highly Stable and Tunable Chemical Doping of Multilayer WS2 Field Effect Transistor: Reduction in Contact Resistance. *ACS Appl. Mater. Interfaces* **7,** 23589–23596 (2015).

55. Iqbal, M. W. *et al.* Tailoring the electrical and photo-electrical properties of a WS2 field effect transistor by selective n-type chemical doping. *RSC Adv.* **6,** 24675–24682 (2016).

56. Zhang, W. *et al.* High-gain phototransistors based on a CVD MoS2 monolayer. *Adv. Mater.* **25,** 3456–3461 (2013).

57. Perea-L ̃opez, N. *et al.* Photosensor device based on few-layered WS2 films. *Adv. Funct. Mater.* **23,** 5511–5517 (2013).

58. Garcia, A. *et al.* Analysis of electron beam damage of exfoliated MoS2 sheets and quantitative HAADF-STEM imaging. *Ultramicroscopy* **146,** 33–38 (2014).

59. Zan, R. *et al.* Control of Radiation Damage in MoS2 by Graphene Encapsulation. *ACS Nano* **7,** 10167–10174 (2013).

60. Wang, S., Lee, G.-D., Lee, S., Yoon, E. & Warner, J. H. Detailed Atomic Reconstruction of Extended Line Defects in Monolayer MoS 2. *ACS Nano* **10,** 5419–5430 (2016).

61. Lui, C. H. *et al.* Trion-induced negative photoconductivity in monolayer MoS2. *Phys. Rev. Lett.* **113,** 1–5 (2014).

62. Yang, Y. *et al.* Hot Carrier Trapping Induced Negative Photoconductance in InAs Nanowires toward Novel Nonvolatile Memory. *Nano Lett.* **15,** 5875–5882 (2015).

63. Nakanishi, H. *et al.* Photoconductance and inverse photoconductance in films of functionalized metal nanoparticles. *Nature* **460,** 371–375 (2009).

64. Ratha, S., Simbeck, A. J., Late, D. J., Nayak, S. K. & Rout, C. S. Negative infrared photocurrent response in layered WS2/reduced graphene oxide hybrids. *Appl. Phys. Lett.* **105,** 2012–2017 (2014).

65. Pandey, M. *et al.* Defect-Tolerant Monolayer Transition Metal Dichalcogenides.

Nano Lett. **16,** 2234–2239 (2016).

66. Yuan, S., Roldán, R., Katsnelson, M. I. & Guinea, F. Effect of point defects on the optical and transport properties of MoS2 and WS2. *Phys. Rev. B* **90,** 41402 (2014).

67. Konstantatos, G. *et al.* Hybrid graphene–quantum dot phototransistors with ultrahigh gain. *Nat. Nanotechnol.* **7,** 363–368 (2012).

68. Lan, C., Li, C., Yin, Y. & Liu, Y. Large-area synthesis of monolayer WS2 and its ambient-sensitive photo-detecting performance. *Nanoscale* **7,** 5974–5980 (2015).

7

Conclusion and Future Works

Contents

7.1 Summary and Conclusions 222
7.2 Outlook into Future Works 224

7.1 Summary and Conclusions

The four years' DPhil work is carried out during a period of time that the studies in 2D materials quickly progress. Our understanding on the properties of 2D materials as well as their interaction to the conventional 3D materials are being deepen with the help of new tools and devices fabricated with the novel 2D materials. This thesis covers the experimental studies on 2D materials from synthesis to applications in electronics and optoelectronics and finally to the novel *in-situ* electronics. The unchanged ambition of the author is to understand and make use of the uniqueness of 2D materials.

In chapter 4, the origin of cracks and holes on the transferred graphene are studied, which results an improvement in the quality of transferred graphene. It is found that single layer graphene grown on liquid copper are too tenuous to sustain the change in morphology of copper during solidification. Tears and cracks are generated during

this period. A second growth method is thus provided to grow graphene epitaxial from the edge of its tears then stich the broken graphene film. Transfer process of CVD graphene grown on melted copper is also carefully studied. Conventional wet etching method is very time consuming and prone to induce cracks in graphene during the transfer process. A two-step etching procedure is thus provided as a solution. By anodic etching W and then etching Cu with $(NH_4)_2S_2O_8$ solution, graphene film free from hole and cracks can be transferred. The study in this chapter paves the road toward of CVD graphene based electronic applications.

Further to the device fabrication of graphene, chapter 5 discusses photodetectors fabricated with CVD grown WS_2. The Schottky barrier between CVD WS_2 and gold contacts is found to be tuned by the incident light intensity. Stronger incident light leads to a more linear IV curve, which marks the lowering of effective Schottky barrier. It is revealed that the trapped states between WS_2 and gold contact dominate the effective Schottky barrier. When illuminated by incident light, the trapped states are filled by holes and thus lowering the Schottky barrier. This finding emphases the important role of trapped states between metal contact and 2D materials.

The fabrication of in-situ electronic devices in chapter 6 is motivated by the willing to link the structure of 2D materials with its electronic behaviours. As a starting of this study, I measure the electrical reaction of WS_2 to incident electron beam. It is surprising to find a negative electron-conductance in WS_2. When incident electron

beam form TEM hit the suspended CVD WS_2, the conductance of it decreases. TEM characterization does not reveal any defects in the WS_2 structure within the time span of our experiment and thus the change in conductance is like due to the trapping of hot charge carrier in intrinsic trapped states inside of the WS_2. Further to the study on electron response of WS_2, *in-situ* electric shock is applied to the WS_2 film with thick amorphous residual. It is interesting to find that instead of removing the amorphous carbon, multilayer graphene is formed in contemporary with the breakdown of graphene. Our discovery provide an quick and efficient way to synthesis WS_2 nanoparticle decorated graphene film, which is desirable in the catalytic applications.

7.2 Outlook into Future Works

As the epilogue of this thesis, this section aim to offer an outlook into the future that works in this thesis could lead to. Electronic and optoelectronic devices are fabricated and reported in this thesis. Two major future works are foreseen to branches out from the work in this thesis.

Firstly, the optoelectronics reported in chapter 5 of the thesis should lead to a novel transparent photo detector. The Schottky barrier lowering caused by trapped states between metal electrodes and 2D materials is potentially lead to a new type of photo conductor that display good photo responsivity as well as quick response. This type of high-gain photo conductor with 2D materials should enable a novel transparent camera with satisfactory recording rate. By combining the TMDC materials as the

photo sensing materials and graphene as the electrode, the camera could be transparent by itself. This would enable in-situ detection and measurement of the light intensity without complex designed optical system.

Another promising work in the future relays on further development of our in-situ electronic measurement system. With the help of in-situ electronic measurement, the structure of materials can be linked with electronic properties directly. Experimental studies present in this thesis should be viewed as a start of such a project. I believe that further study on the effect of defects to the electronic properties of 2D materials, especially when in the form of nanoribbon, should be of interest. Furthermore, this measurement tool is transferable to many other studies in nano-electronics, for example the single molecule junction. It is hopefully that this work would enable a new experimental platform for materials study.